NAVAL POSTGRADUATE SCHOOL

MONTEREY, CALIFORNIA

THESIS

DETONATION DIFFRACTION IN A MULTI-STEP CHANNEL

by

Daniel Michel Juillet

December 2010

Thesis Advisor:	Chris Brophy
Second Reader:	Jose Sinibaldi

Approved for public release; distribution is unlimited

THIS PAGE INTENTIONALLY LEFT BLANK

REPORT DOCUMENTATION PAGE		*Form Approved OMB No. 0704–0188*

Public reporting burden for this collection of information is estimated to average 1 hour per response, including the time for reviewing instruction, searching existing data sources, gathering and maintaining the data needed, and completing and reviewing the collection of information. Send comments regarding this burden estimate or any other aspect of this collection of information, including suggestions for reducing this burden, to Washington headquarters Services, Directorate for Information Operations and Reports, 1215 Jefferson Davis Highway, Suite 1204, Arlington, VA 22202–4302, and to the Office of Management and Budget, Paperwork Reduction Project (0704–0188) Washington DC 20503.

1. AGENCY USE ONLY *(Leave blank)*	2. REPORT DATE December 2010	3. REPORT TYPE AND DATES COVERED Master's Thesis	
4. TITLE AND SUBTITLE Detonation Diffraction in a Multi-Step Channel		5. FUNDING NUMBERS N0001410WX20832	
6. AUTHOR(S) Daniel M. Juillet			
7. PERFORMING ORGANIZATION NAME(S) AND ADDRESS(ES) Naval Postgraduate School Monterey, CA 93943–5000		8. PERFORMING ORGANIZATION REPORT NUMBER	
9. SPONSORING /MONITORING AGENCY NAME(S) AND ADDRESS(ES) N/A		10. SPONSORING/MONITORING AGENCY REPORT NUMBER	

11. SUPPLEMENTARY NOTES The views expressed in this thesis are those of the author and do not reflect the official policy or position of the Department of Defense or the U.S. Government. IRB Protocol number _____N/A____.

12a. DISTRIBUTION / AVAILABILITY STATEMENT Approved for public release; distribution is unlimited	12b. DISTRIBUTION CODE

13. ABSTRACT (maximum 200 words)

This research investigated multiple detonation diffraction events in order to better understand the limits and benefits of diffraction strategies with respect to pulse detonation engine design. Hydrogen/air detonations were generated using swept ramp obstacles in a 1.27 m long channel with a cross section of 25.4 mm by 88.9 mm and were diffracted into various multiple-stepped openings. This allowed the detonation wave diffraction transmission limits to be determined for hydrogen/air mixtures and to better understand reinitiating mechanisms throughout the diffraction process. Tests were conducted for area ratios ranging from 2.00–2.60 with varying equivalence ratios from 0.5–1.5.

Computational methods were used to better understand the diffraction phenomenon using a series of sensitivity studies for different chemistry sets, computational cell size and equivalence ratio. Experimental tests used combined optical shadowgraph and particle image velocimetry imaging systems to provide shock wave detail and velocity information. The images were observed through a newly designed explosive proof optical section and split flow detonation channel. It was found that area ratios of 2.0 could survive single and double diffraction events over a range an equivalence ratio range of 0.8 to 1.14 Area ratios of 2.3 survived the primary diffraction event for equivalence ratios near stoichiometric for the given step length. Detonation diffraction for area ratios of 2.6 did not survive the primary diffraction event for any equivalence ratio and were unable to transmit to a larger combustor.

14. SUBJECT TERMS Detonation Diffraction in a multi–step channel			15. NUMBER OF PAGES 152
			16. PRICE CODE
17. SECURITY CLASSIFICATION OF REPORT Unclassified	18. SECURITY CLASSIFICATION OF THIS PAGE Unclassified	19. SECURITY CLASSIFICATION OF ABSTRACT Unclassified	20. LIMITATION OF ABSTRACT UU

THIS PAGE INTENTIONALLY LEFT BLANK

Approved for public release; distribution is unlimited

DETONATION DIFFRACTION IN A MULTI-STEP CHANNEL

Daniel M. Juillet
Major, Canadian Air Force
B.S., Ottawa University, 2001

Submitted in partial fulfillment of the
Requirements for the degree of

MASTER OF SCIENCE IN MECHANICAL ENGINEERING

from the

NAVAL POSTGRADUATE SCHOOL
December 2010

Author: Daniel M. Juillet

Approved by: Dr. Chris Brophy
Thesis Advisor

Dr. Jose Sinibaldi
Second Reader

Dr. Knox Millsaps
Chairman, Department of Mechanical and Aerospace
Engineering

THIS PAGE INTENTIONALLY LEFT BLANK

ABSTRACT

This research investigated multiple detonation diffraction events in order to better understand the limits and benefits of diffraction strategies with respect to pulse detonation engine design. Hydrogen/air detonations were generated using swept ramp obstacles in a 1.27 m long channel with a cross section of 25.4 mm by 88.9 mm and were diffracted into various multiple-stepped openings. This allowed the detonation wave diffraction transmission limits to be determined for hydrogen/air mixtures and to better understand reinitiating mechanisms throughout the diffraction process. Tests were conducted for area ratios ranging from 2.00–2.60 with varying equivalence ratios from 0.5–1.5.

Computational methods were used to better understand the diffraction phenomenon using a series of sensitivity studies for different chemistry sets, computational cell size and equivalence ratio. Experimental tests used combined optical shadowgraph and particle image velocimetry imaging systems to provide shock wave detail and velocity information. The images were observed through a newly designed explosive proof optical section and split flow detonation channel. It was found that area ratios of 2.0 could survive single and double diffraction events over a range an equivalence ratio range of 0.8 to 1.14 Area ratios of 2.3 survived the primary diffraction event for equivalence ratios near stoichiometric for the given step length. Detonation diffraction for area ratios of 2.6 did not survive the primary diffraction event for any equivalence ratio and were unable to transmit to a larger combustor.

THIS PAGE INTENTIONALLY LEFT BLANK

TABLE OF CONTENTS

LIST OF FIGURES

THIS PAGE INTENTIONALLY LEFT BLANK

LIST OF TABLES

THIS PAGE INTENTIONALLY LEFT BLANK

LIST OF ACRONYMS, ABBREVIATIONS AND NOMENCLATURE

α	angle between disturbance trajectory and un diffracted shock normal
Δ	reaction length
γ	ratio of specific heats
Δh_0	reaction energy release
λ	detonation cell width
λ_{cr}	critical number of detonation cell widths
p	pressure
ρ	density
τ	reaction time
θ	non-dimensional effective activation energy
A	pre-exponential parameter
c	frozen acoustic speed
c_{rz}	reaction zone acoustic speed
CJ	Chapman–Jouguet state
C_p	constant pressure specific heat
C_v	constant volume specific heat
d	tube diameter
d_c	critical tube diameter
H	channel height
H_c	critical channel height
e	specific internal energy
E_a	activation energy
h	specific enthalpy
k	reaction rate constant
M	Mach number
p	pressure
R_g	gas constant
0	pre shock state

1	post-shock state
t	time
t_c	critical time for disturbance to reach tube axis
T	temperature
u	fluid velocity (lab frame)
u_{rz}	fluid velocity reaction zone
U_s	shock velocity
v	transverse disturbance velocity
V_{CJ}	Chapman-Jouguet detonation velocity
vn	von-Neumann post-shock state
W	molecular mass
x	distance
x_c	critical distance for disturbance to reach tube axis
Φ	equivalence ratio

ACKNOWLEDGMENTS

First off I would like to thank my wife, Christina, and my two daughters, Reece and Baylee, for supporting my work and their understanding for all that time away from home.

Secondly, working with Dr. Chris Brophy and his rocket lab staff Dave, George and Bobby was a tremendous privilege and without his guidance and all the help of the staff this thesis would not have been possible.

Lastly, I thank the Canadian Air Force for making this truly life-changing experience a reality.

THIS PAGE INTENTIONALLY LEFT BLANK

I.   INTRODUCTION

It is estimated that nearly 80% of the world's energy is derived from the combustion of hydrocarbon fuels in various forms. In today's energy conscience and profit-driven society, even modest improvements in current systems can yield staggering economic gains. The quest to continuously improve energy efficiencies of such combustion driven systems has spawned research in numerous areas. Pressure gain combustion schemes such as detonation and constant volume combustion hold considerable promise in achieving said efficiencies [1]. They have inherently higher theoretical thermal efficiencies primarily due to their near constant volume detonation based combustion cycle which generate much less entropy when compared to constant pressure events, creating a pressure rise during heat release. Pulse detonation combustors (PDC) exploit such efficiencies. When applied in a pulse detonation engine they are estimated to achieve greater specific impulses over many conventional systems for a greater range of flight regimes, as seen in Figure 1.
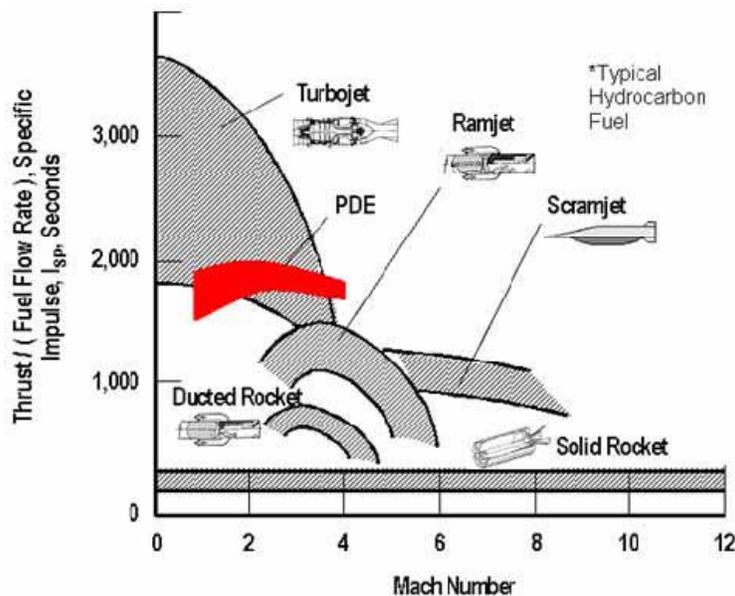
Figure 1.   Comparison of high-speed propulsion technologies (From [2])

Unfortunately, the ability to detonate high mass flow rates in a reliable and repeatable manner has been shown to be a tremendous challenge [3]. This is especially true for accepted kerosene-based aviation fuels, which are much more difficult to detonate than hydrogen. Additionally, the energy required to directly initiate a detonation in a combustor large enough to be of practical use in a pulsed detonation engine can be very difficult. Naturally, much research has attempted to negate complex, high-energy ignition mechanisms by using smaller channels or predetonators followed by a transition into a larger section. Predetonators or initiators typically involve transitioning a deflagration into a detonation through turbulence devices to accelerate the flame. Such devices can have losses, so once the detonation is formed, it is normally preferable to transition a wave to a larger cross sectional area. This allows for additional fuel processing by a surviving detonation wave. Numerous geometries and combinations have been used to date, but it remains to be seen whether a specific geometry can offer any advantages over others. Hence, the requirement to better understand the detonation diffraction phenomena all types of geometries.

Many configurations investigated in the open literature include Brophy et al., [4, 5], who studied a number of initiator-combustor combinations, shown in Figure 2a through Figure 2c, with oxygen-based initiators with some success.
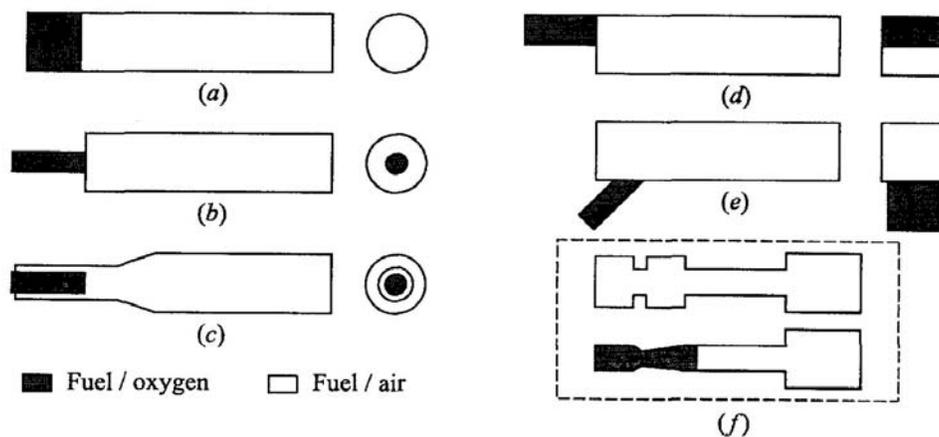
Figure 2. Various initiator main combustor conjurations (From [3])

2

Oxygen-based diffracting initiators were eventually abandoned due to U.S. Navy safety concerns and ultimately led the way to a new generation of swept ramp initiators, which have been shown to reduce pressure losses by a factor of 5 over conventional turbulence devices [6].

A great deal of historical detonation research deals with fundamental diffraction cases into unconfined spaces and provides tremendous understanding of the detonation phenomenon. Unfortunately, there is considerably less literature on subcritical reinitiating events, whereby initiator sections are made as small possible to support a multiheaded detonation wave front. Such cases are of prime concern in the aero propulsion world, since weight and space are at a premium. In order to diffract detonations from heavier and more stable fuels with larger cell structures such as JP–10, initiators will no doubt be required to operate at elevated pressures in a limited amount of volume, so the need to understand how aggressive a detonation can diffract is very important.

This research aims to continue investigations in detonation diffraction by exploring multiple diffractions in a 1 to 3.5 aspect ratio channel, in order to better understand the limits and benefits of diffraction strategies with this respect to pulse detonation engine design. Hydrogen/air detonations were generated using swept ramp obstacles in a 1.27 m long channel with a cross section of 25.4 mm by 88.9 mm and were diffracted into various multiple-stepped openings. Tests were conducted for area ratios ranging from 2.00–2.60, with varying equivalence ratios from 0.5–1.5.

Computational methods were also used to better understand the diffraction phenomenon using a series of sensitivity studies for different reduced chemistry sets, computational cell size and equivalence ratio. Experimental tests used combined optical shadowgraph and particle image velocimetry imaging systems to provide shock wave detail and velocity information.

Results from the research provide baseline design criteria for some current pulse detonation engine concepts being investigated in Figure 3.
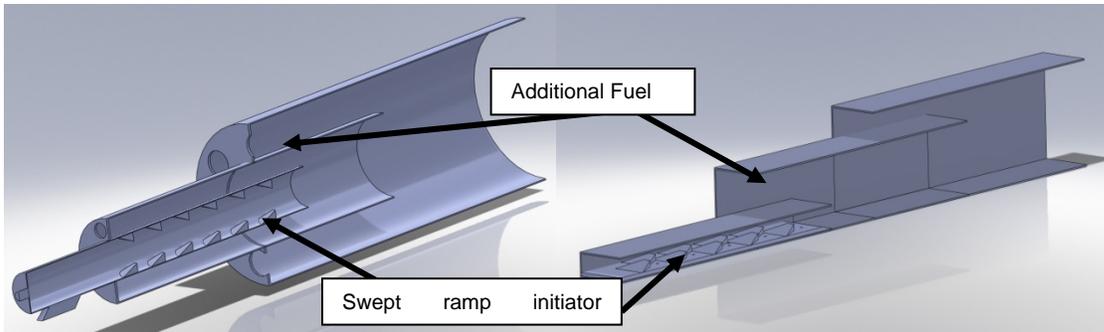
Figure 3.   Cross sectional view of a Concentric Tube and multiple high aspect
ratio channel detonation combustors

The use of concentric tubes or multiple high aspect ratio channels to transition additional fuel to the combustor while isolating the initiator section may allow for greater thrust production.   In each diffraction plane the detonation front is supported by additional air and fuel mixture. Such concepts have the potential to produce higher specific impulse values while also smoothing the inherent intermittent production of thrust.   For the concept to work, the detonation front must survive every diffraction event through an appropriate area change.

II.   BACKGROUND

A.   COMBUSTION WAVE TYPES

Combustion events can be classified into three categories, explosion, deflagration and detonations.   Generally, in explosions the rate of heat generation is extremely fast and does not require a combustion wave through the exploding media.   Deflagrations on the other hand propagate at much lower velocities with regard to reactants they transmit through.   They are essentially subsonic expansions waves with pressure drops across the reaction zone due to products that are accelerated away from the wave in the opposite direction proportional to diffusivity and rate of reaction.   Detonations are characterized by supersonic combustion waves that propagate extremely fast through a reactive mixture increasing the thermodynamic properties sharply, creating a shock-induced chemical reaction, which drives the detonation. Some basic detonation models include Chapman–Jouguet and the ZND models. Main differences are depicted in Table 1.

Table 1.   Detonation and deflagration parameters (From [1])

	Detonation	Deflagration
u_1/c_1 (Mach Number)	5 – 10	0.0001 – 0.03
u_2/u_1	0.4 – 0.7 (deceleration)	4 – 6 (acceleration)
P_2/P_1	13 – 55 (compression)	≈ 0.98 (slight expansion)
T_2/T_1	8 – 21 (heat addition)	4 – 16 (heat addition)
ρ_2/ρ_1	1.7 – 2.6	0.06 – 0.25

B.   RANKINE HUGONIOT GAS DYANAMIC RELATIONS

Rankine (1870) and Hugoniot (1887–1889) were the first to investigate solutions to the non-reacting conservation equations involving shockwave, often termed the Rankine-Hugoniot jump conditions since they applied a control

volume across the shock looking solely at the upstream and downstream components.   In doing so, they were able to derive theses components in terms of wave speed, pressures and particle velocity post shockwave. Lee [7] provides a nice derivation of these relations, starting with the one-dimensional steady state conservation equations across a fixed detonation wave, specified as follows with subscripts 0 and 1 representing reactant and product states with velocities determined with respect to the wave, as depicted in Figure 4. This theory provides a good first approximation to the changes in properties during detonations and should also be noted that these equations assume a steady and adiabatic front.

$$u_0, p_0, \rho_0, h_0 \qquad\qquad u_1, p_1, \rho_1, h_1$$
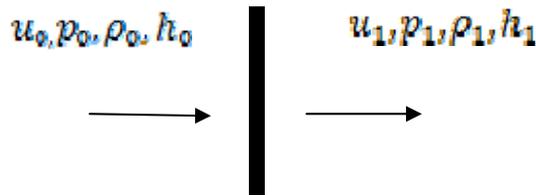
Figure 4.   One-dimension steady state model

$$\text{Mass } \quad \rho_0 u_0 = \rho_1 u_1 \qquad\qquad (1)$$

$$\text{Momentum } \quad p_0 + \rho_0 u_0^2 = p_1 + \rho_1 u_1^2 \qquad\qquad (2)$$

$$\text{Energy } \quad q + h_0 + \frac{u_0^2}{2} = h_1 + \frac{u_1^2}{2} \qquad\qquad (3)$$

If we specify an equation of state for both reactant and products using the perfect gas law ($p = \rho RT$), and if we assume $h = C_p T$ with the relationship $C_p - C_v = R$ and $\gamma = \frac{C_p}{C_v}$, enthalpy can now be written as follows:

$$h = \frac{\gamma}{\gamma - 1}\frac{p}{\rho} \qquad\qquad (4)$$

6

Since we have five unknowns (u_1, p_1, ρ_1, h_1 and u_0), the latter being detonation wave speed and only four equations, one more equation is required to close the set.

In order to close this equation, we need to define the Hugoniot curve equations. If we start by combining Equations 1 and 2, we obtain:

$$\frac{p_1 - p_0}{v_0 v_1} = \rho_0^2 u_0^2 = \rho_1^2 u_1^2 = \dot{m}^2 \tag{5}$$

$$\dot{m} = \sqrt{\frac{p_1 - p_0}{v_0 - v_1}} \tag{6}$$

In this case, $v = 1/\rho$ is known as specific volume and $\dot{m} = \rho u$ mass flux per unit area. If we start by observing the pressure-specific volume plane of all theoretically possible solutions, we can start to better understand relations between Rayleigh lines and Hugoniot curves. Looking at Equation 6, we can see that real solutions only exist in the detonation and deflagration regions in white in Figure 5.
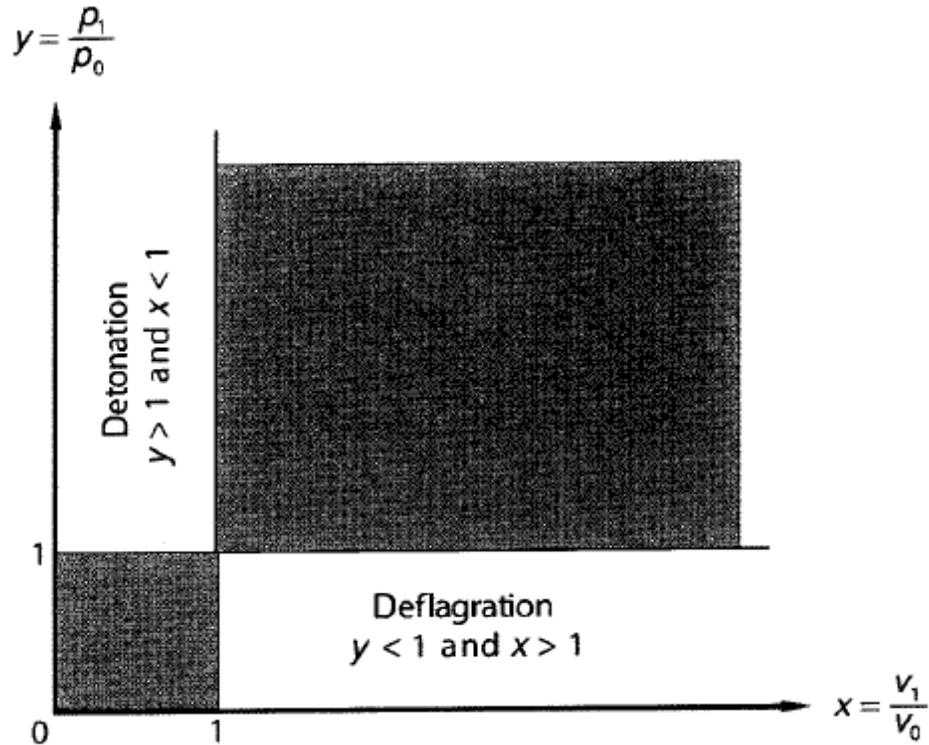
Figure 5.　　Solutions in the p–v plane (From [7])

For solutions to exist, we have either $p_1 > p_0, v_0 > v_1$, the case where we have a compression solution for a detonation or $p_1 < p_0, v_0 < v_1$ an expansion solution and deflagration, as in Figure 5 Lee defines $x = v_1/v_0 = \rho_0/\rho_1$ and $y = p_1/p_0$, in doing so one can now rewrite Equation 6 as:

$$y = (1 + \gamma_0 M_0^2) - (\gamma_0 M_0^2)x \tag{7}$$

this is the Rayleigh line equation with a slope of $-(\gamma_0 M_0^2)$, we observe that the combustion wave velocity is directly proportional to square root of the slope. Equation 7 describes a thermodynamic path the gas takes to across the combustion wave from state (1, 1) to state (x, y).

8

The Hugoniot curve represents an agglomeration of all possible attainable downstream states, for a given specific set of initial conditions, as depicted in Figure 6. By eliminating velocities in Equation 3, we obtain the following equation for the Hugoniot curve:

$$h_1 - (h_0 + q) = \frac{1}{2}(p_1 + p_0)(v_0 - v_1)$$ (8)

We also know that solutions to the conservation equations must satisfy both Rayleigh and Hugoniot curves simultaneously. In other words, the evolution of reactants (x=y=1) to products state (x, y) follow a Rayleigh line until intersection on a Hugoniot curve, seen again at Figure 6. For finite heat addition q, the Rayleigh line will intersect four points on the Hugoniot curve, two in each of the detonation and deflagration branches. In the strong detonation region, both pressure and density increase drastically and require overdriven initial conditions.
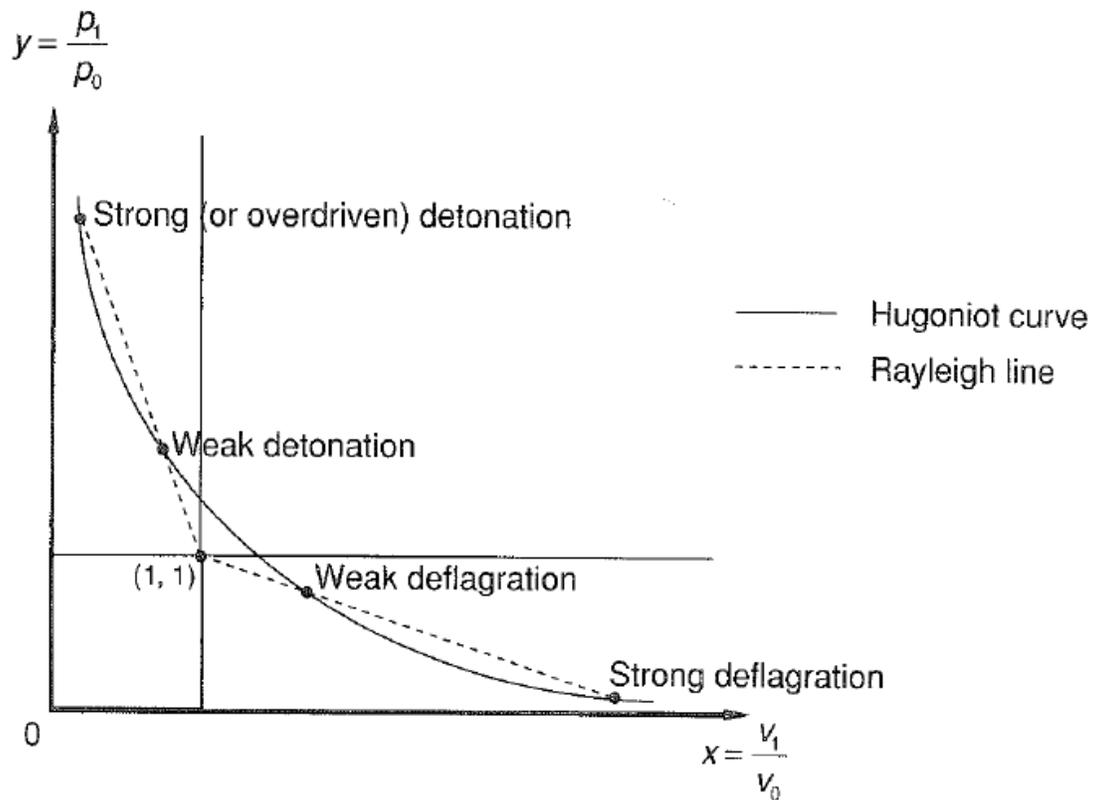
Figure 6.   Rayleigh line and Hugoniot curve (From [7])

Two other solutions exist when the Rayleigh line is tangent to the Hugoniot curve. In this case, we obtain a minimum velocity on the detonation branch and a Mach number of the burned gas of $M_1=1$. The tangency solutions are known as Chapman–Jouguet solutions seen in Figure 7. The upper solution agrees quite well to the experimental data and is easily calculated using Newton–Raphson iterations and has been incorporated in such programs as the NASA "Chemical Equilibrium with Applications" (CEA), developed by McBride, Zehe and Gordon [9].
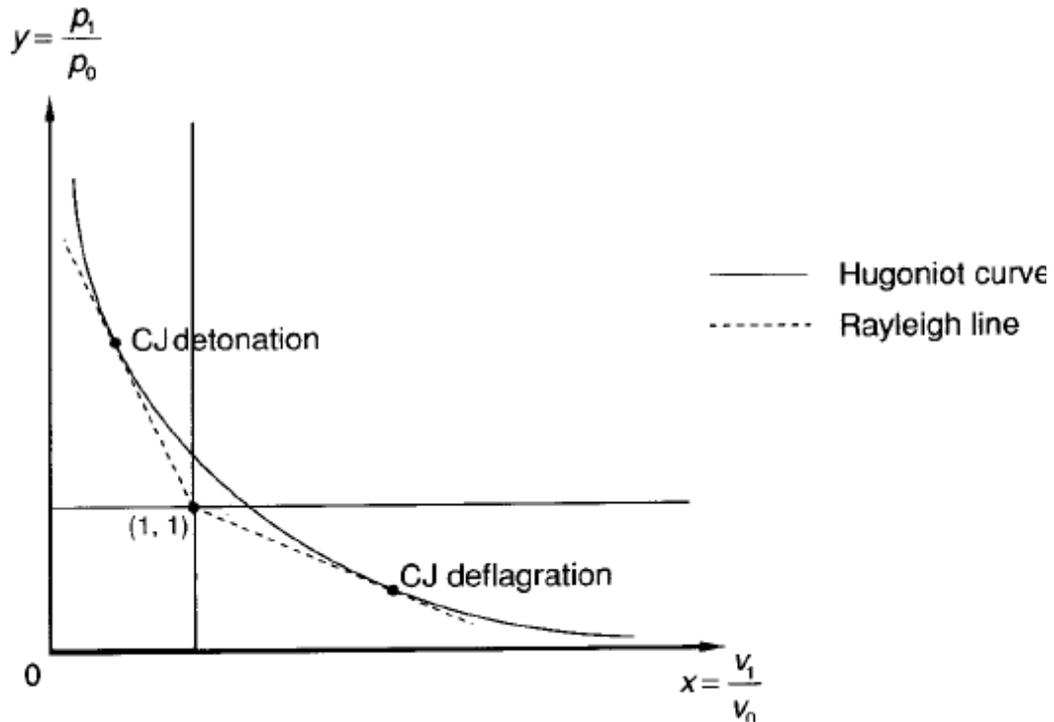
Figure 7.   Chapman–Jouguet tangency solutions   (From [7])

C.   ZEL'DOVICH–VON NEUMANN–DORING (ZND) ONE DIMENSIONAL WAVE STRUCTURE

A simple and widely accepted model of a detonation wave is the ZND model comprising of a strong shock front followed by a much thicker induction and reaction zone travelling at Chapman-Jouguet velocity. The shockwave initially adiabatically compresses the mixture to a peak pressure known as the Van Neumann state, enabling dissociation of the molecules within a thermally neutral induction zone. At a certain point, enough free radicals are created to start the chain branching reactions eventually converting all reactants into products within a reaction zone. The rapid chemical reaction rates enable a very quick rise in temperature dropping both pressure and density in the reaction zone the resulting expansion accelerate the gases away behind the front coupling it the acoustic front [7].

Induction Zone

Equilibrium Products $(w_{CJ} = a_{CJ})$

Energy Release Zone

V_{CJ}

Reactants

Normal Shock

T_{CJ}

P_{vN}

P_{CJ}

T_{vN}

Reaction Zone

P_1

T_1

x
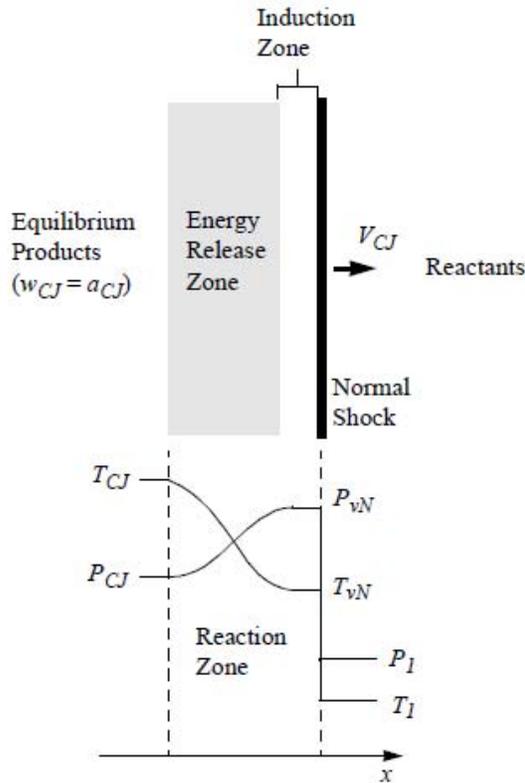
(a) Steady, one-dimensional ZND model.
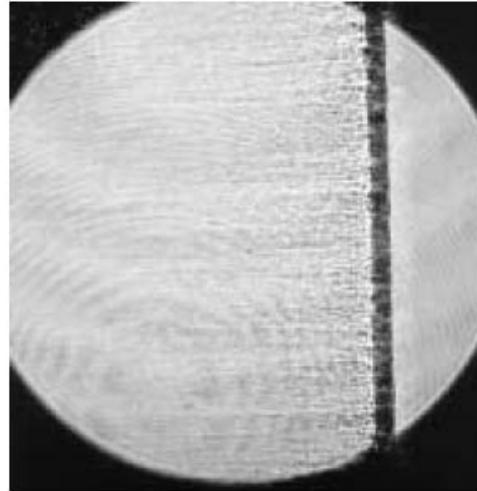
(b) Laser shadowgraph of self-propagating detonation wave ($H_2 + 0.5O_2$, $P_1 = 20$ kPa)

Figure 8.   Model and Real detonation (From [8])

D.   DETONATION CELL STRUCTURE

Detonation fronts in real life have complex three dimensional structures. The wave front contains multiple and constantly interacting curved incident, Mach stems and reflected shock waves meet at so called triple points. These structures are highly transient due to spatial and temporal instabilities. If we observe the highly resolved Schlieren photograph on Figure 9, we can see what the reaction looks like before two transverse waves collide. The accompanying sketch provides some additional explanation into all the interconnected events.

12
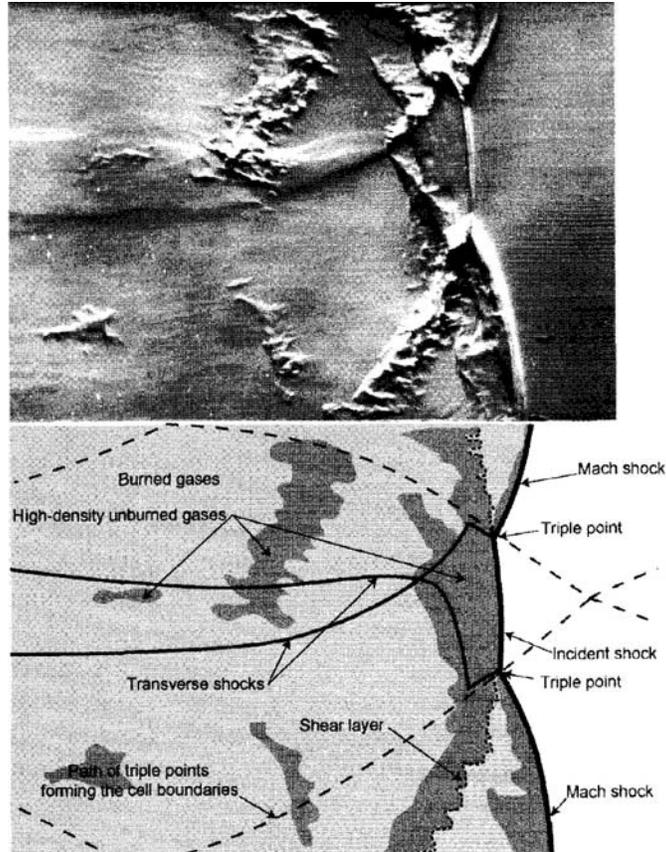
Figure 9.   Schlieren photograph of a detonation in a thin channel (From [7])

The shock front has multiple colliding waves that progress transversely across the front, creating a triple point path that forms a diamond shape. The chemical reactions are not always perfect during a detonation event; note the turbulent nature of the reaction zone behind the detonation with numerous shear layers and unburned pockets that are consumed. In highly unstable mixtures like hydrogen–air and many hydrocarbons have strong transverse waves which tend to drive the detonation. This can reduce the amount of chemical energy contributing to the main front leaving unburned pockets to be consumed later by turbulent diffusion. These mixtures can also exhibit irregular cell structures and irregular triple point trajectories. Contrary to some highly regular cell structured mixtures that contain heavy amounts of argon as depicted in Figure 10.

13

Detonations with regular cell structure are less reliant on transverse wave collisions to continue the propagation of the front. Generally, these mixtures are more reactive.
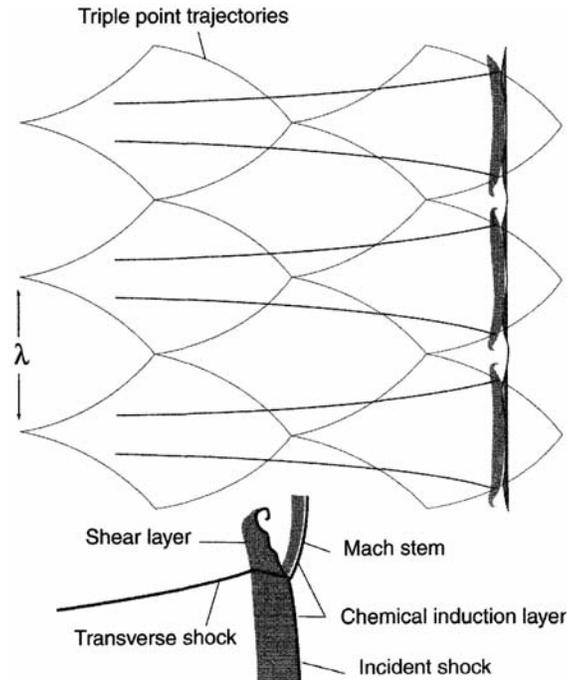
Figure 10.   Example of a regular triple point cell structure of a detonation
(From [7])

Triple point trajectories can be mapped by soot foil techniques whereby shear and pressure gradients rearrange soot particles leaving behind evidence of triple point paths. From these soot foils traces, cell width λ can be determined and provides for an estimation of mixture reactivity. The smaller the cell width is the tighter the coupling is between chemical kinetics and gas dynamic effects. It should be noted however that there is a large variance in measurements in cell structure via soot foils as observed by Shepherd [10]. Soot foil measurements can be very subjective with errors up to 50%.

14

E.   STOICHIOMETRY

Combustion conditions of fuel–oxidizer mixtures are generally specified in terms of equivalence ratio Φ. This characterizes the proportion of fuel to oxidizer in the mixture. Defined as the ratio of the fuel–oxidizer ratio to the stoichiometric fuel–oxidizer ratio and can be mathematically represented as follows:

$$\phi = \frac{m_{fuel}/m_{oxidizer}}{\left(m_{fuel}/m_{oxidizer}\right)_{stoichiometric}} = \frac{n_{fuel}/n_{oxidizer}}{\left(n_{fuel}/n_{oxidizer}\right)_{stoichiometric}} \tag{9}$$

The composition and thermodynamic properties of fuel–oxidizer mixtures during combustion and detonation are dependent on the equivalence ratio. Consequently the detonation cell width is also highly dependent on mixture fuel ratio. A ratio greater than 1 implies excess fuel or fuel rich mixtures than would be required for a stoichiometric reaction and conversely a ratio less than one implies excess oxidizer or fuel lean mixtures. Looking more closely at the dependence of detonation cell width by inspecting Figure 11, we can see a very strong relation to equivalence ratio. Cell width for a particular mixture is smallest at or very close to Φ=1.
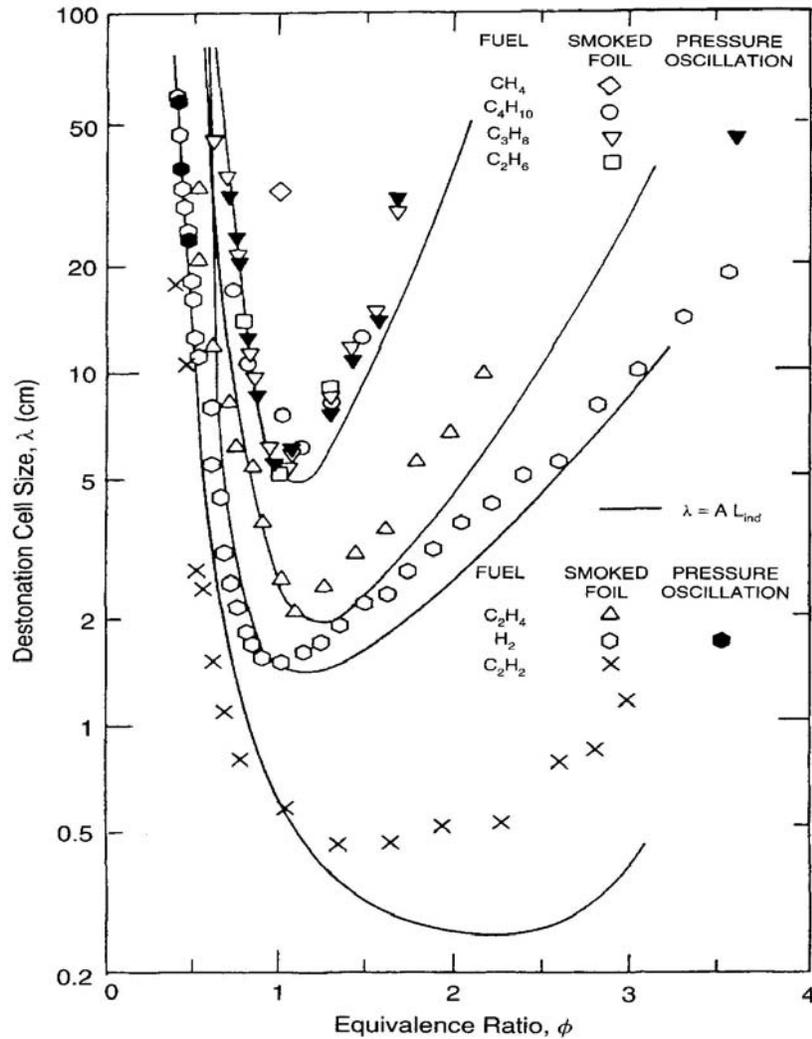
Figure 11.   Variation in detonation cell size with fuel air composition (From [1])

F.   DETONATION DIFFRACTION

Diffraction occurs when a confined detonation is allowed to expand into a larger cross sectional area at which point expansion waves are communicated to the flow from the behind the front. Diverging transverse waves affected by this perturbation produce unsteadiness and curvature in the front, which by definition also reduces chemical reaction rates. This reduces the energy is release rate thereby providing less support to the detonation front.   Lee illustrates this in

Figure 12, we see a rarefaction fan eventually propagates toward the axis of the channel or tube and the flame front decouples from the acoustic front in a total failure.
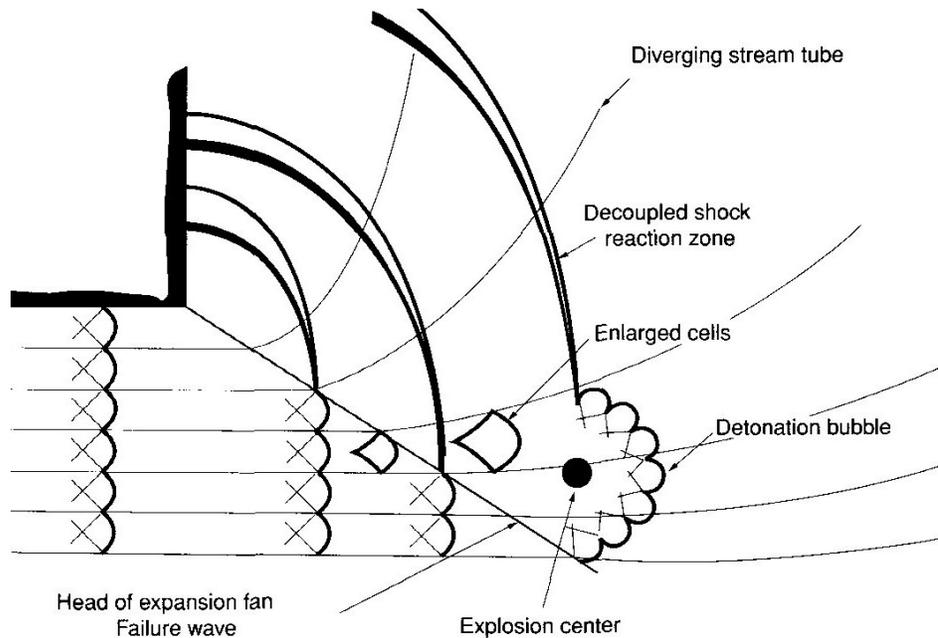
Figure 12.   Rarefaction fan penetrating propagating a toward detonation axis (From [8])

Whether a detonation survives or fails an expansion depends on a number of factors: mixture composition, thermodynamic initial conditions, confining geometry or boundary conditions and detonation velocity at diffraction plane. Three different cases have been observed: super critical where a detonation successfully transitions a diffraction plane, subcritical cases occur when a detonation wave is quenched and critical cases are known as the transition point between the two previous cases, seen in Figure 13.

17

(a) Supercritical: successful transmission.

(b) Critical: re-initiation as shock decouples from reaction zone.

(c) Subcritical: complete failure as shock decouples from reaction zone.
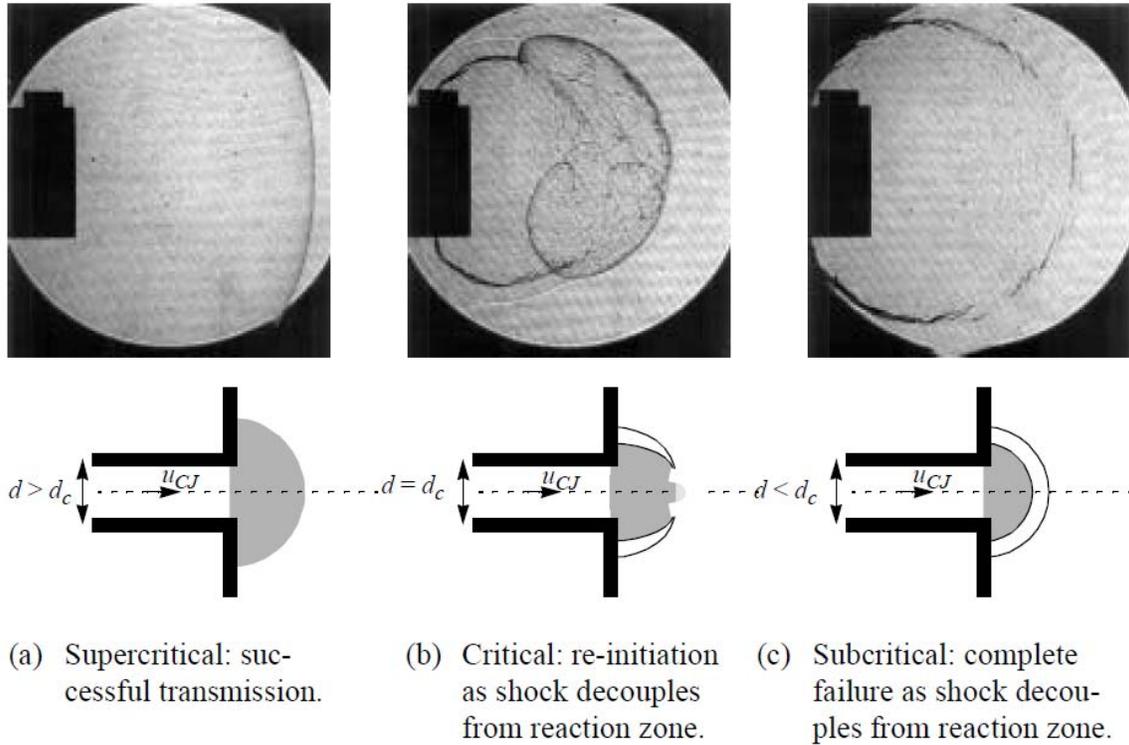
Figure 13.   Diffraction regimes (From [8])

The detonation wave diffraction phenomena is not new; however, the last 75-plus years of research in this area has still has not yielded a complete understanding of all the fluid dynamic complexities in this event.   With all detonations, high pressures and temperatures, short and varying time scales have stymied much of the research involved in this area. Lafitte [11] was the first to attempt the transition of a detonation wave from a 7mm tube into a spherical chamber using a mixture of CS_2+O_2. He was unsuccessful.   Zeldovich's [12] Streak camera experiments exhibited detonations that decayed completely into flames for some conditions while others continued to detonate across the diffraction plane, he established that for various tube diameters a critical diameter exists for successful reinitiation into a larger space, based on a mixtures initial conditions and confinement properties. With improvements in experimental

18

techniques in the 1950s through 1970s, cellular structure of the detonation wave was better characterized. Shchelkin and Troshin [13], were the first to relate cell size to the Zeldovich–Newmann–Doring (ZND) model reaction length. Mitrofanov and Solouhkin [14] noted the first empirical correlation relating detonation cell width to critical tube diameter; they proposed that the critical diameter is 13 times the detonation cell width λ. They demonstrated that for a number of hydrocarbon fuels that if a detonation front had 13 or more cell widths across a tube diameter, the detonation would survive a diffraction event into any open space with the same chemistry. Follow-on research [15, 16, 17] finds this theory breaks down for more regular cell structured fuel mixtures and higher aspect ratio rectangle configurations as seen in Figure 14. Extreme aspect ratio channels great than 5 asymptote to critical channel widths W_c of 4 times the detonation cell width λ. Such channels appear to more easily transition detonation waves as other transverse modes are suppressed and expansion is restricted to two dimensions.
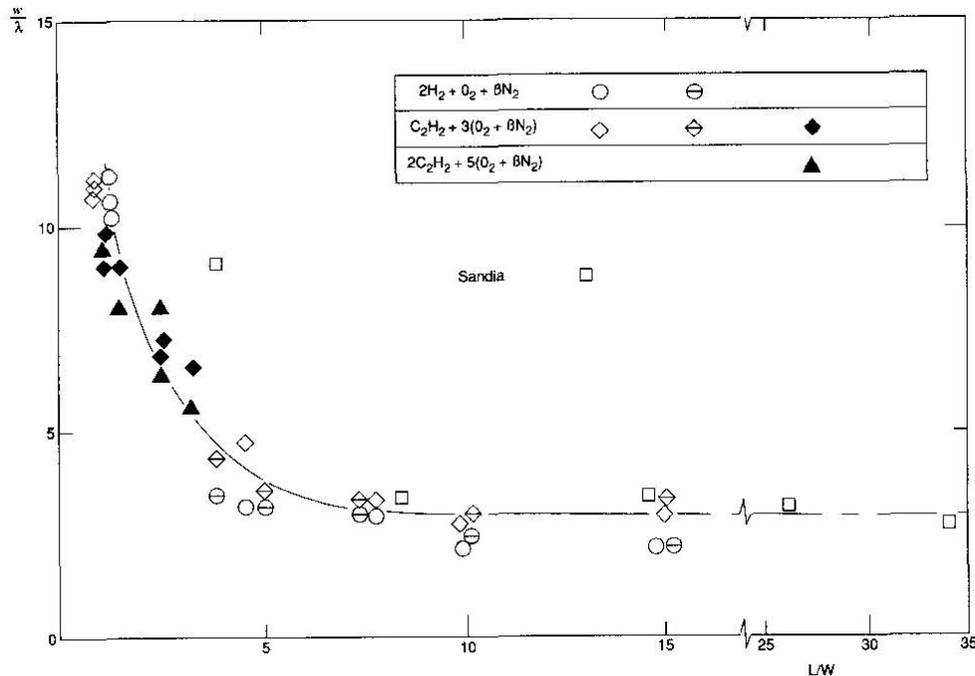
Figure 14.   Critical channel height as a function of aspect ratio (From [7])

19

Cell structure and chemical kinetics, as well as initial and boundary condition, play a major role in how detonations waves expand, break down and reinitiate, as well as the initial and boundary conditions [17, 18].

III. COMPUTATIONAL SETUP

A. INTRODUCTION

Computational fluid dynamic (CFD) software was used extensively during the research in order to compliment experimental results and to better understand all the complexities of a diffracting gaseous detonation wave. Numerical results also provided additional details of the flow field that were difficult or impossible to do so experimentally. Simulations were largely based on solving the two dimensional non-linear compressible inviscid reactive conservation equations known as the Reactive Euler equations below in conjunction with multi–step reduced chemistry sets with nine species (H_2, O_2, H, O, OH, HO_2, H_2O_2, H_2O, and N_2) and 18/19 elementary reactions in rectangular coordinates..

$$\frac{\partial \rho}{\partial t} + \frac{\partial (\rho u)}{\partial x} + \frac{\partial (\rho v)}{\partial y} = 0,$$

$$\frac{\partial (\rho u)}{\partial t} + \frac{\partial (p + \rho u^2)}{\partial x} + \frac{\partial (\rho u v)}{\partial y} = 0,$$

$$\frac{\partial (\rho v)}{\partial t} + \frac{\partial (\rho u v)}{\partial x} + \frac{\partial (p + \rho v^2)}{\partial y} = 0,$$

$$\frac{\partial (\rho e)}{\partial t} + \frac{\partial (\rho u e + p u)}{\partial x} + \frac{\partial (\rho v e + p v)}{\partial y} = 0,$$

$$\frac{\partial (\rho \lambda)}{\partial t} + \frac{\partial (\rho u \lambda)}{\partial x} + \frac{\partial (\rho v \lambda)}{\partial y} = \dot{\omega}$$

$$\dot{\omega} = -k\rho\lambda \, \exp\left(-\frac{E_a}{RT}\right),$$

$$e = \frac{p}{(\gamma - 1)\rho} + \frac{u^2 + v^2}{2} + \lambda Q \quad \text{and} \quad p = \frac{\rho RT}{M}.$$

(10–17)

In short conservation of mass, momentum in both x and y directions, energy along with all species equations in terms of Arrhenius rates and an equation of state were used. Metacomp's CFD++ software was used to solve this equation set. Structured meshes were generated using Pointwise meshing software package. In order to set–up a baseline for the study, a number of sensitivity studies were conducted using computational cell size, degree of overdrive, stoichiometry and chemistry. Sensitivity simulations were obtained using both implicit and explicit schemes. Due to the transient nature of detonations, implicit simulations, a CFL of 1 was used to ensure maximum stability. In all explicit time-marching schemes, CFL number was ramped from 0.5–1 during the first 1500 iterations allowing the simulation to resolve initial deflagration to detonation formation. Consequently, the time step selection in explicit time-marching simulations were critical for stability, in our case as a detonation wave crosses a discrete grid, the time step must be small enough to resolve it.

B.   REDUCED CHEMISTRY

In order to correctly predict where and how detonation waves would diffract and whether or not the end state survived or failed, heavy reliance on reduced chemistry was required. Simple H_2 and O_2 reactions systems have been known to encompass hundreds of reactions. However, computational resources are normally limited. There has been significant research in using reduced chemical models that capture the most important characteristics with respect to a particular application. Models in the past have either assumed one-step equilibrium based chemistry having limited success in predicting detonations. This has tended to over simplify the reaction and over predict product temperature. Computational power today has allowed for multistep finite rate chemistry allowing better prediction of heat release and ignition delay times (induction time) during a detonation.

This research looked at three reduced sets that have less than 20 reactions, none of which were developed exclusively for detonation based

combustion. The first set developed by Kurkov & Burrows at NASA for scramjets was based on lower combustion pressure regimes [19]. The second set was a modified Kurkov set that included the some energy absorbing NO chemistry based on a reduction scheme from Kuo [1]. The last set used was developed at Stanford by Peterson and Hanson for ram accelerators for a range of higher pressures for up to pressured of 50 atm [20], as seen in Table 2. Hydrogen air detonations as explained earlier are highly unstable reactions and have tremendous pressure fluctuations that can range from 10 atm to 27 atm or from $0.5P_{cj}$ to $1.5P_{cj}$. [7]. The reaction rates were expressed in Arrhenius form as follows:

$$k = AT^n \exp\left(-\frac{E_a}{RT}\right) \tag{18}$$

The reaction rate constant, k was a function of temperature, pre-exponential parameter A described the frequency of collisions for the species that result in a reaction as well as the preferred orientation of the molecular species that favor a reaction. The exponent n expresses the temperature dependence of the pre-exponential parameter. Activation energy, E_a defines the minimum amount of energy required for a reaction to occur and R is the universal gas constant.

Table 2.   Peterson & Hanson reduced set for high pressure H_2/O_2, N_2 reaction mechanism for ram accelerator (From [20])

Number	Reaction[a]	Rate coefficient[b]			Comments[c]
		A	n	E	
1	$O + H_2 = H + OH$	5.00×10^4	2.70	6,290	(R3)
2	$H + O_2 + M = HO_2 + M$	2.80×10^{18}	-0.90	0	(R33)[d]
3	$H + O_2 + O_2 = HO_2 + O_2$	3.00×10^{20}	-1.70	0	(R34)
4	$H + O_2 + H_2O = HO_2 + H_2O$	9.38×10^{18}	-0.80	0	(R35)
5	$H + O_2 + N_2 = HO_2 + N_2$	2.60×10^{19}	-1.20	0	(R36)
6	$H + O_2 = O + OH$	8.30×10^{13}	0.00	14,413	(R38)
7	$H + HO_2 = O_2 + H_2$	2.80×10^{13}	0.00	1,068	(R45)
8	$H + HO_2 = OH + OH$	1.34×10^{14}	0.00	635	(R46)
9	$H + H_2O_2 = HO_2 + H_2$	1.21×10^7	2.00	5,200	(R47)
10	$OH + H_2 = H_2O + H$	2.16×10^8	1.50	3,430	(R84)
11	$OH + OH + M = H_2O_2 + M$	7.40×10^{13}	-0.40	0	k_{inf}, (R85)[e,f]
		2.30×10^{18}	-0.90	$-1,700$	k_0
12	$OH + HO_2 = O_2 + H_2O$	2.90×10^{13}	0.00	-500	(R87)
13	$OH + H_2O_2 = HO_2 + H_2O$	1.75×10^{12}	0.00	320	k_a, (R88)[g]
		5.80×10^{14}	0.00	9,560	k_b, (R89)[g]
14	$HO_2 + HO_2 = O_2 + H_2O_2$	1.30×10^{11}	0.00	$-1,630$	k_c, (R115)[h]
		4.20×10^{14}	0.00	12,000	k_d, (R116)[h]
15	$O + O + M = O_2 + M$	1.20×10^{17}	-1.00	0	(R1)[i]
16	$O + H + M = OH + M$	5.00×10^{17}	-1.00	0	(R2)[e]
17	$H + OH + M = H_2O + M$	2.20×10^{22}	-2.00	0	(R43)[j]
18	$H + H + M = H_2 + M$	1.00×10^{18}	-1.00	0	(R39)[k]

Note: species = H, O, OH, H_2, O_2, HO_2, H_2O_2, H_2O, and N_2 (or Ar, He, etc.).
[a] All reactions are reversible.
[b] $k(T) = AT^n \exp(-E/RT)$; units are in cal, mol, cm^3, and s.
[c] Corresponding RAMEC[28] reaction numbers are in parentheses.
[d] M does not include O_2, H_2O, or N_2; all collision efficiencies = 1.0.
[e] Collision efficiencies for M; $N_2 = 1.0$, $H_2 = 2.0$, $H_2O = 6.0$, and Ar = 0.70, all others = 1.0.
[f] See Table 2 for Troe parameters.
[g] Rate coefficient is non-Arrhenius; $k_{13} = k_a + k_b$.
[h] Rate coefficient is non-Arrhenius; $k_{14} = k_c + k_d$.
[i] Collision efficiencies for M: $N_2 = 1.0$, $H_2 = 2.4$, $H_2O = 15.4$, and Ar = 0.83, all others = 1.0.
[j] Collision efficiencies for M: $N_2 = 1.0$, $H_2 = 0.73$, $H_2O = 3.65$, and Ar = 0.38, all others = 1.0.
[k] Collision efficiencies for M: $N_2 = 1.0$, $H_2 = 1.7$, $H_2O = 7.0$, and Ar = 0.63, all others = 1.0.

C.   COMPUTATIONAL MESH

The computational mesh used was a two dimensional channel with an open step in the positive y direction with a 1:6 height expansion ratio. A resolution of 50 μm or roughly 300 computation domains in one detonation cell for H_2 was used equaling to approximately 4.5 million cells. The mesh was developed using Pointwise 64-bit meshing software and converted to run in a

CFD++ environment, as seen in Figure 15. Some researchers have reported that the resolution requirement to fully resolve complex chemistry simulations is an element size of only 0.1 μm for the CJ H2–air detonations at 1 atm and 298 K [21]. Essentially three orders of magnitude finer of the induction zone thickness. Such resolutions would be well beyond currently available computational resources and could not be attempted in this study. Additionally, previous studies at NPS [22] have shown that this resolution predicts detonation velocity within 5–10% of CJ values. It was hoped that this resolution would be sufficient to capture failure modes of a detonation diffracting around an open step.

The model was scaled down slightly from the original experimental setup, with channel height scaled down to 1:2 and the channel length scaled down 1:5, this allowed for solutions within a week.
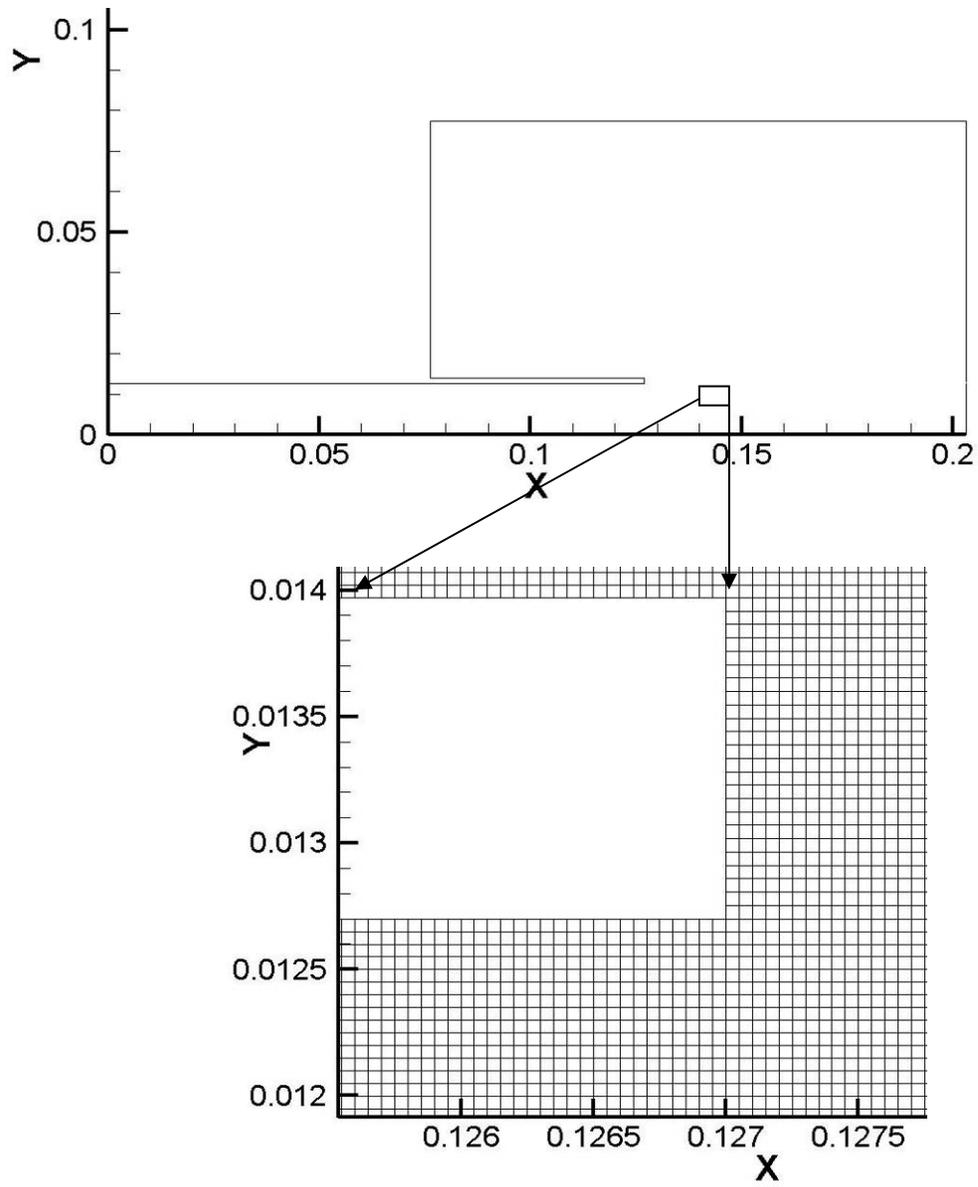
Figure 15.   Computational domain (in m) for diffraction studies

D. BOUNDARY AND INITIAL CONDITIONS
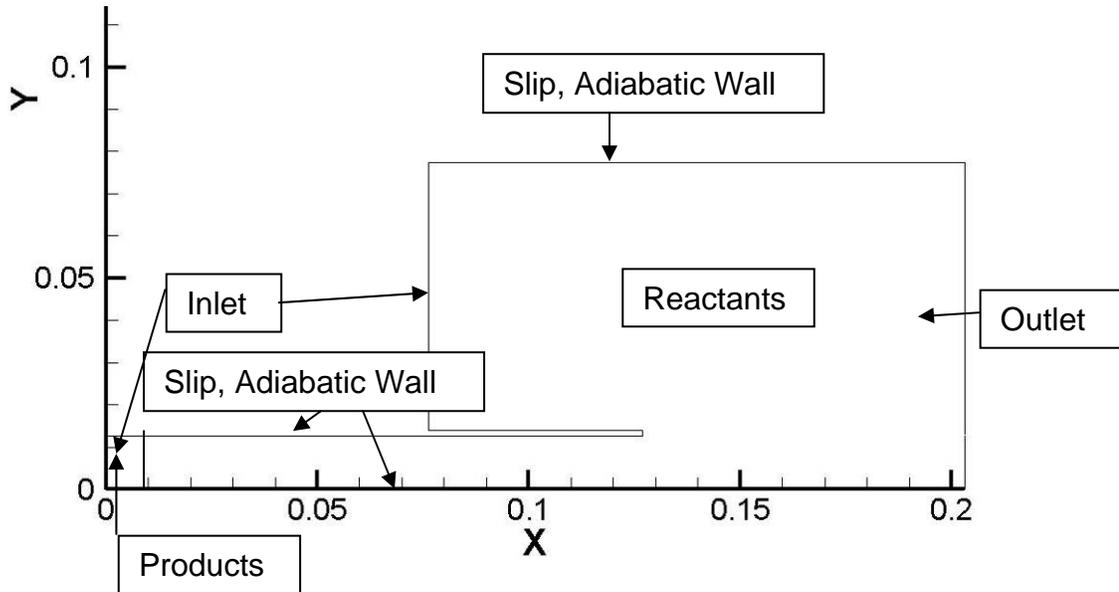
Figure 16.   Boundary and Initial Conditions Computational results

Detonation waves in the simulations were created by introducing overdriven high pressure products in small region at the beginning into a main body of reactants. Detonation products were initiated at two times CJ Pressure and at CJ Temperature conditions, which as alluded to above was found to be the minimum overdrive found for given conditions to initiate a detonation wave characteristic of the fuel-oxidizer mixture as part of the initial conditions. Mass fraction of the detonation products were obtained from NASA Chemical Equilibrium Analysis (CEA) [9] and a sample is included in Appendix A. Reactant initial conditions were assumed to be at 1 atm and 298 K, essentially matching experimental conditions for further validation. Typical run set structure was as follows:

Equation Set Type
- Unsteady Compressible Euler
- Equation of State: Ideal Gas

Riemann Solver
- Minimum Dissipation: LHS
- No pressure switching

Boundary Conditions (See Figure 16)
Time Integration
- Implicit CFL=1
- explicit (for some runs) based a CFL ramped from 0.5 − 1 over the first 1500 iterations

Spatial Discretization
- 2nd Order Accuracy in Space
- Dimension of polynomial: 2–D XY
- Axis stability enhancement: Yes
- Types of Total Variation Diminishing (TVD) Limiter: Minmod

IV.   EXPERIMENTAL SETUP

A.   DETONATION CHANNEL MAIN COMPONENTS

The combustor design was driven by three main requirements, the desire to use hydrogen and air as reactants, a large field of view in the test section in order to facilitate both shadowgraph and particle image velocimetry and lastly, the ability to adapt the existing main tube design in test cell one. The main components of the detonation diffraction test setup consists of an inlet manifold, a 48-inch long rectangular channel in which an inner split flow channel is inserted with a one 3.5-inch tall by 1-inch wide inner channel dimensions and an optical section. This configuration allows for detonations to pass through a lower section and diffract through an upper section carrying unreacted fuel-air mixture into a viewable optical section seen at Figure 17. Appendix B includes all engineering drawings for the split flow insert and optical section components as well as the new manifold
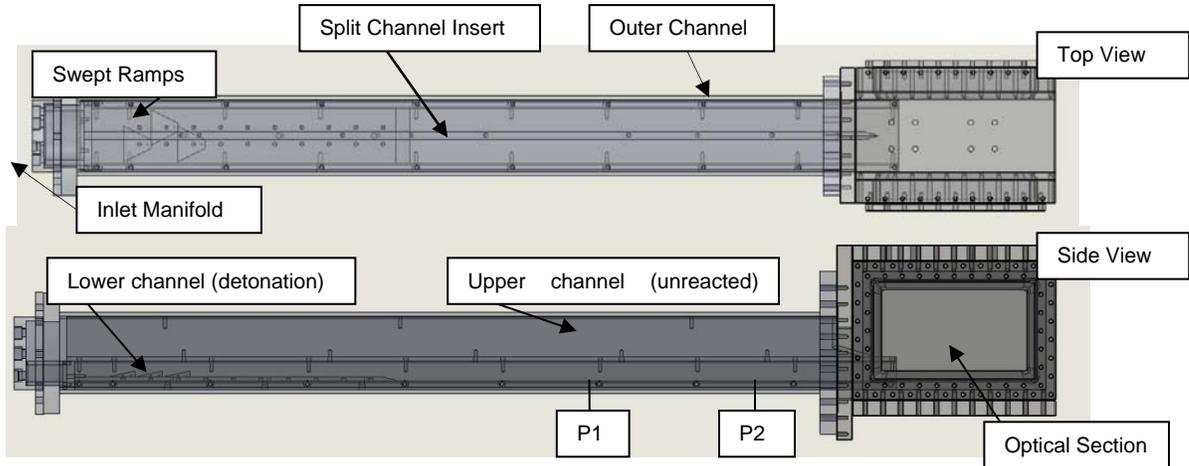

Figure 17.   Schematic of detonation diffraction channel, top and side view
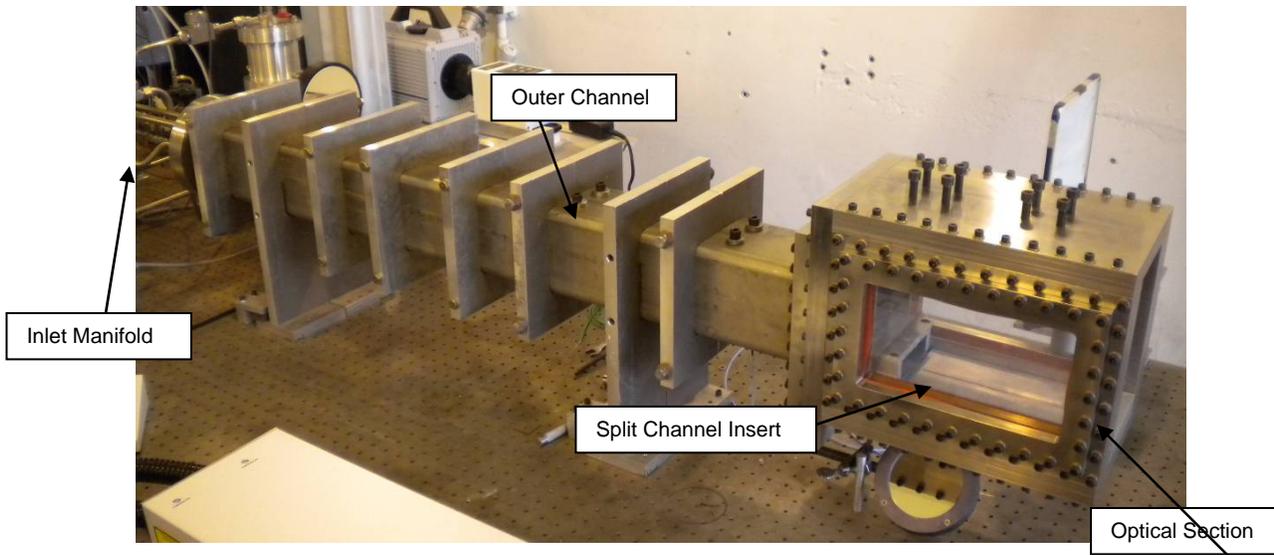
Figure 18.   Main test section components

B.   COMBUSTOR OPERATION

This pulse detonation combustor setup operates on a relatively simple single cycle mode in order to facilitate optical experimental observations with shadowgraph and Particle Image Velocimetry (PIV). It was operated on an optics table consisting of two electro pneumatic ball valves that controlled fuel and seeding air along with a main air duct regulated by a computer controlled pressure regulator. Also, various check valves, two hand pressure regulators to set precise pressures for fuel and seeding along with two mass metering chokes. Two lasers were employed to illuminate the detonation front for image capture for their respective camera system using a continuous Argon-Ion for shadowgraph and a double pulsed Nd–Yag for PIV, seen in Figure 19. Two kistler high-speed pressure transducers acquired high speed data and were used to determine detonation velocity as well as trigger the PIV system via a BNC 555 pulse delay generator. Labview commercial control and automation software was used to operate the test engine. The standard sequence consisted of filling the upper on lower channel with a seeded titanium dioxide hydrogen/air mixture and igniting it

and subsequently measuring pressure, detonation velocity, acquiring high speed shadowgraph images and particle image velocimetry images. See Appendix C for standard operating procedures.
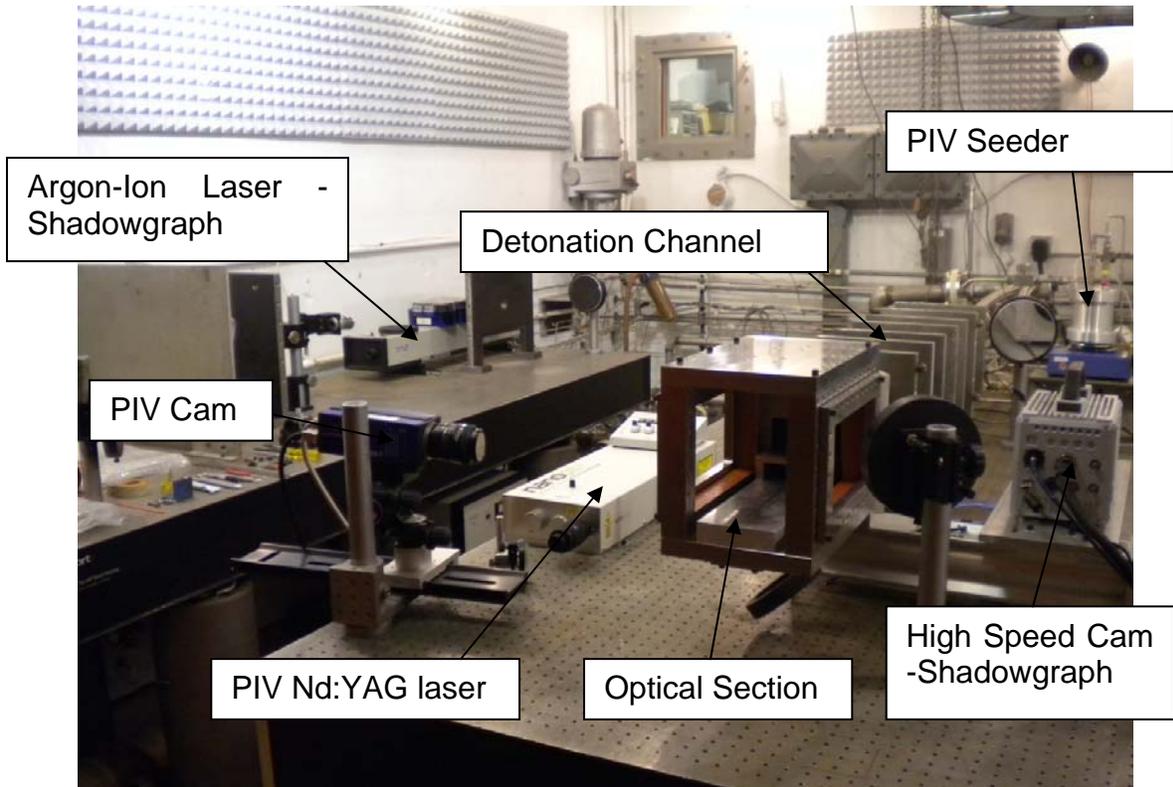
Figure 19.   Overall experimental setup
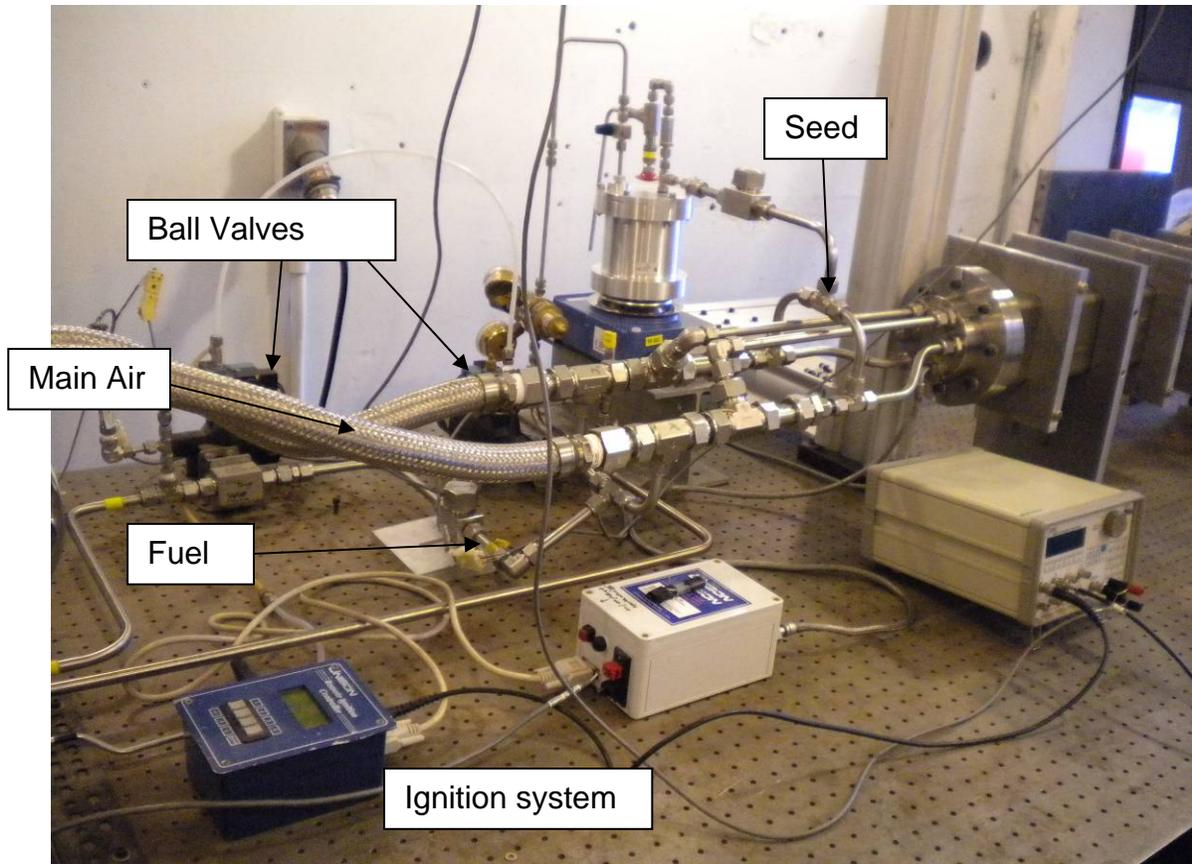
Figure 20.   Overall experimental Setup

C.   OPTICAL SECTION

The tube was attached to an 8.5-inch tall by 12.5-inch long and 4.5-inch wide optical section with opposing 5-inch by 9-inch viewing areas using 45-degree chamfered flush fit BK7 optical glass. Various step configurations can be installed into the section. The design was based on a previous section by Fludovich [4], however the new section was designed to be more modular with a larger optical viewing area bolting directly to the detonation channel with access ports above and below, seen in Figure 21. The entire section was machined into mainly one inch thick 304 stainless steel sections and was assembled with socket cap head screws. The strong design is required in order to withstand any bending that could compromise the 1.75 inch BK7 optical glass it was designed to encase.
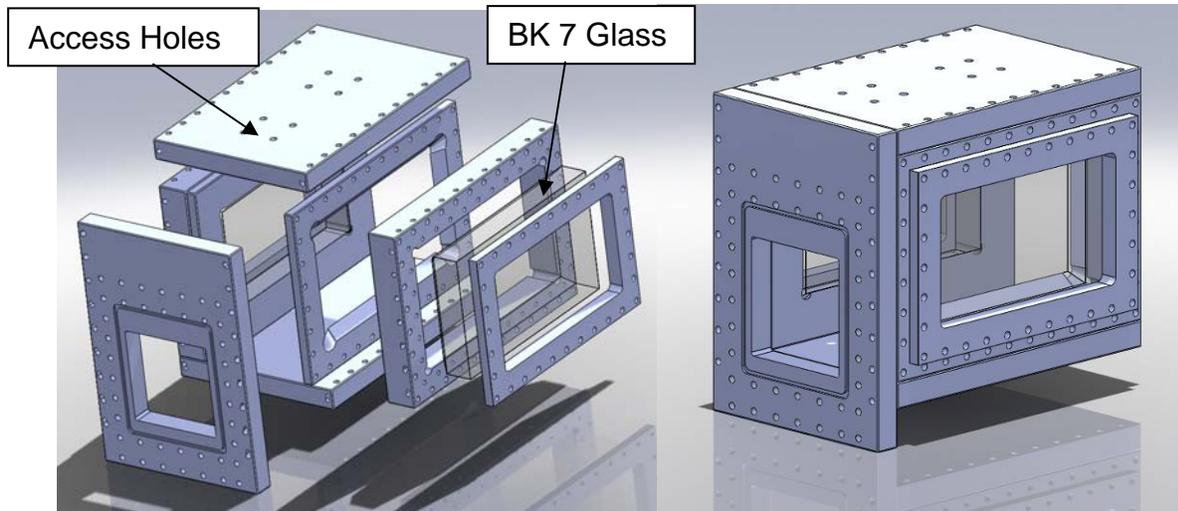
Figure 21.   Stainless Steel 304 optical section

Finite element analysis was performed on the BK7 glass components of the older and newer designs to ascertain maximum stress and deflection under shock loading conditions in order to ensure that the new design would perform equally or better.   A glass thickness of 4.45 cm (1.75 in) was selected to accommodate the detonation impulse pressures of up to 36 atm for up to 1 µs shock loading.   Results of these analyses are presented in Figures 22 and 23.
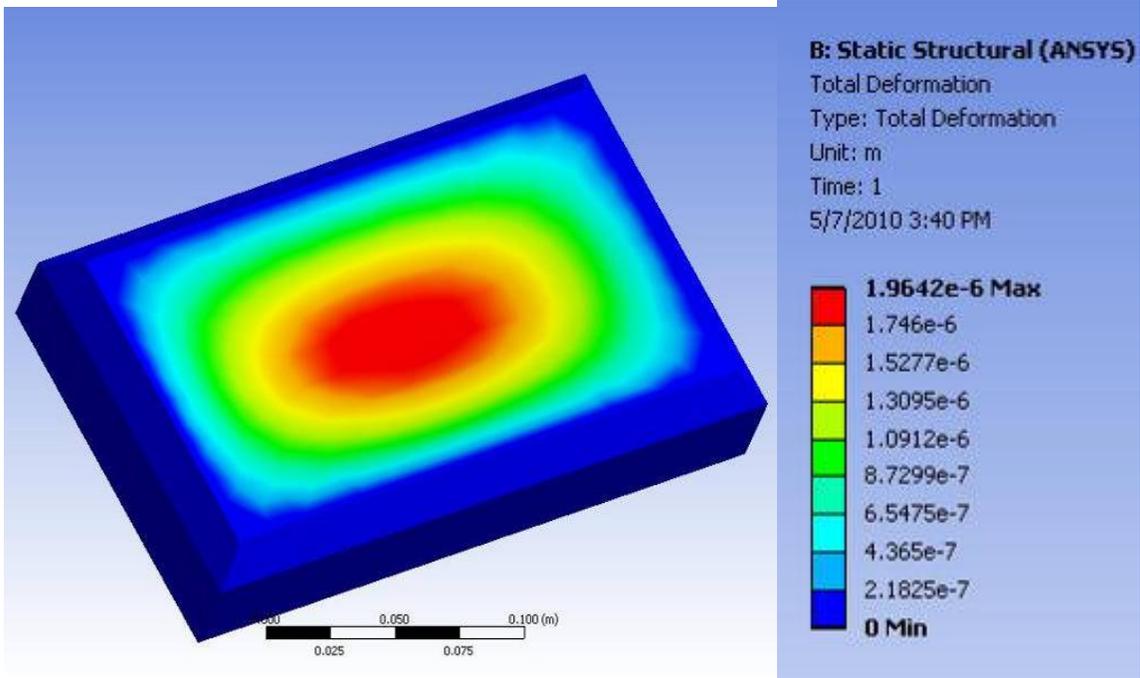
Figure 22.   Deflection results for BK7 glass
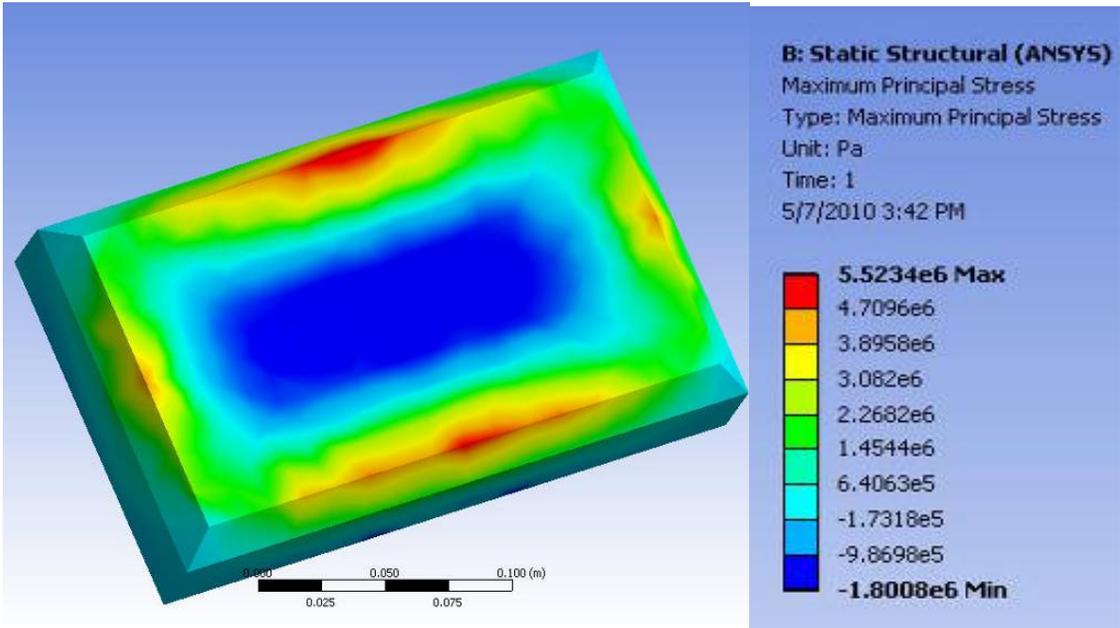
Figure 23.   Principal stress results for the BK7 glass

D. LOWER CHANNEL SPLIT FLOW INSERT

In order for a detonation to diffract into an open step using the existing main square channel, a split flow channel assembly was designed to easily slide into the existing hardware, essentially separating the flow into two channels, an upper and lower allow for a detonation to initiate. The detonations were initiated in the lower section expanding into an adjacent top channel at the diffraction plane directly observed through the optical section. The flame was transitioned into a detonation using 10 interspaced 30-degree swept ramps with a total blockage ratio of 40%. This section was machined from 6061 Al stock and is socket cap screw assembled, more detailed drawings can be viewed in Appendix B.

Figure 24.   Split flow insert.

E.   IGNITION SYSTEM

The detonation is initiated by a Unison Vision-50 variable capacitative discharge using an aviation grade spark plug mounted at the head end of the tube. Prior to testing, the igniter was configured manually to provide a 2 Joule spark and was remotely triggered by the Labview software (Figure 25).

Figure 25.   Unison variable capacitative system (From [23])

F.   FUEL AND AIR DELIVERY SYSTEM

High pressure air was provided to the test cell from the rocket lab facility air system with hydrogen provided from a single bottle. Main control room computers controlled supply pressures for both air and hydrogen with the Tescom ER3000 Version 2.0 software, allowing reactant pressures to be set remotely as required. Fuel, air and seed delivery revolved around the main six port inlet manifold which was designed to adapt to the existing pair of 1 inch main air lines. Further upstream air is fed through a 1.5-inch pipe using a 0.235-inch flow metered choke. The manifold design delivers a high enough mass flow,

ensuring swept ramp effectiveness and thus reliable detonations. The design allows for low pressures seed particulate penetration into the main flow and ensured the seed reservoir's 2 bar pressure limit was not exceeded. Main air lines were broken down into two successive pairs of half inch lines where fuel and seed was fed to the main flow in two stages into the six-holed manifold that accepted up to five lines with one hole tapped for a standard turbine plug., as depicted in Figure 26. Hydrogen was supplied using half-inch tubing that in turn fed two main air arms just prior to the four line split.
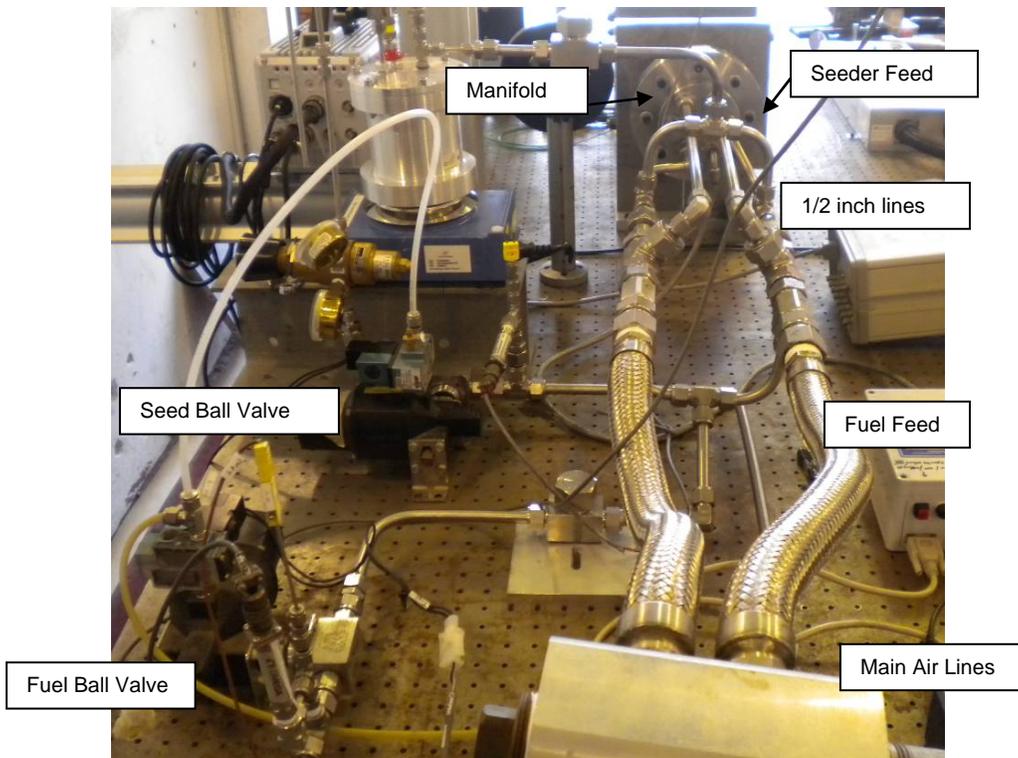
Figure 26.   Inlet manifold and feed lines

Unfortunately hydrogen and seeding could not be regulated using the ER3000 systems since operating pressures were lower then what this system was capable of delivering to within reasonable errors. Hand ball valve regulators were used instead, since typical operating pressures were under 100 psig and 10

psig, respectively. All pneumatic ball valves were controlled by LabVIEW software via Crydom control solenoid switches located in an electronics cabinet located in the test cell as seen in Figures 27 and 28. Choke diameters used during this testing were 0.236 inch for the air supply and 0.157 inch for the hydrogen supply. Two check valves located in the fuel and seed lines were installed to prevent the possibility of backflow due to the detonation event.
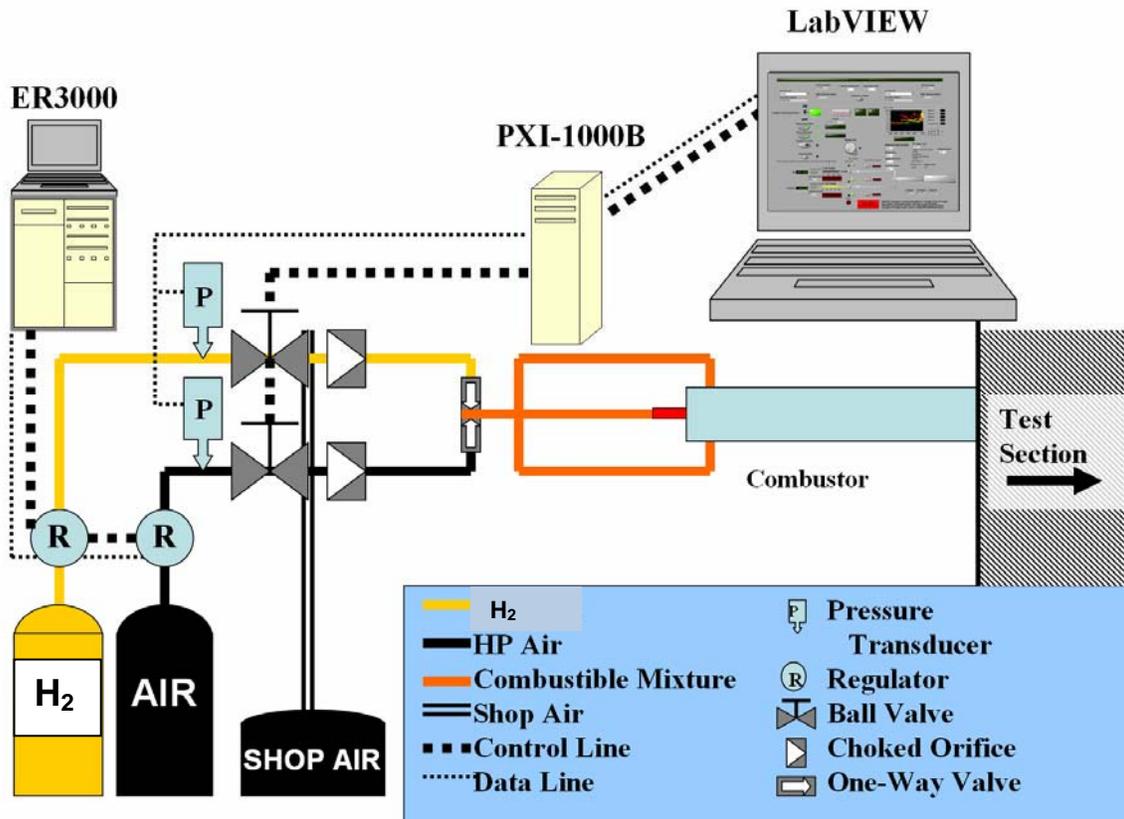
Figure 27.   Fuel and air delivery system (From [23])

G.   INSTRUMENTATION

Instrumentation employed all through the testing controlled initiation as well as data collection. Each of the pressure signals were routed through one of four National Instruments (NI) 14-bit PXI-6115 cards mounted in the NI PXI-1000B chassis, shown in the upper half of Figure 28. This chassis interfaced

with the computers in the control room through the NI PXI-MXI-4 PXI Bridge and was capable of collecting either real-time or high-speed buffered data. Optical data imaged from the high-speed camera and PIV systems were routed to a dedicated desktop computer in the control room.
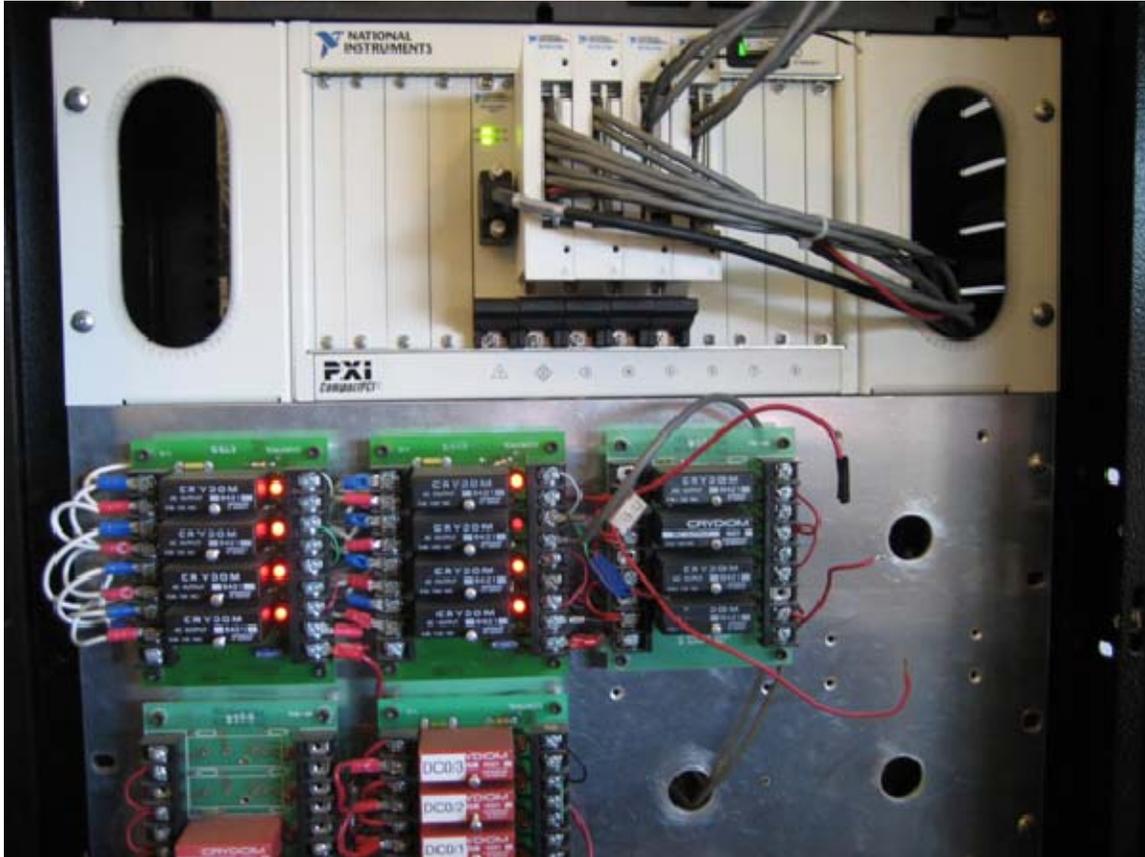
Figure 28. National Instruments PXI–1000B Chassis (upper section) and Crydom Control Solenoid Switches (lower section) (From [23]).

H. DYNAMIC PRESSURE TRANSDUCERS

Inside the channel, two high-frequency Kistler dynamic pressure transducers were mounted as a pair in order to calculate the wave velocity based on the pressure transients. The transducers were connected to Kistler Type 5010 Dual Mode amplifiers which route the data to two NI PXI–6115 data cards in the PXI–1000B for high-speed data collection. Once testing was initiated, the cards were configured to begin collecting data with the triggering of the

capacitive discharge igniter and collected data at a rate of 500 kHz. Data was stored via card buffer and later saved to computers located in the control room. Pressure data supplied from Kistler transducers provided high-resolution confirmation of shock passage.

I.   CONTROL

Every test sequence was initiated and controlled using Labview software. All pressure transducers were linked into to the code to allow for active monitoring during every test sequence. A sample control panel can be seen in Figure 29.

Figure 29.   Sample Labview control panel

J. SHADOWGRAPH

Opposing optical windows allow for the transmission of a shadowgraph light source to pass through the section during a detonation. Shadowgraph setup utilizes an Ion Laser Technology Model 55001 Argon Ion laser emitting 750 mW beam at 488 nm passing into a 6.3 µm spatial filter placed in front of the laser aperture. This produced a spatially filtered light source, which became collimated after being reflected from a concave mirror. The resulting beam was directed through the optical test section using a flat mirror. On the opposite side of the optical test section, a flat mirror directs laser light toward a focusing mirror placed which in turn is directs the light directly into the ultra 17 intensified high-speed camera.

The main rationale for choosing shadowgraph as opposed to Schleiren technique was due to the high coherence length of the argon ion laser system. Such high coherence length, do not provide for good Schleiren images. The argon ion system was used as monochromatic light source.

Invisible Vision's Ultra 17 high-speed camera suite was used to capture all shadowgraph images. The system was triggered from the P1 kistler high speed pressure probe with delays ranging from of 225–275 µs depending on what portion of the optical window was being captured. At the 150,000 fps mode, a resolution of 512 X 512 pixels was possible with this system. Exposure settings varied between 50–500 ns, depending on the amount of light in the test cell while allowing gain to be lower than 30%. Inter frame times were 6.17 µs.
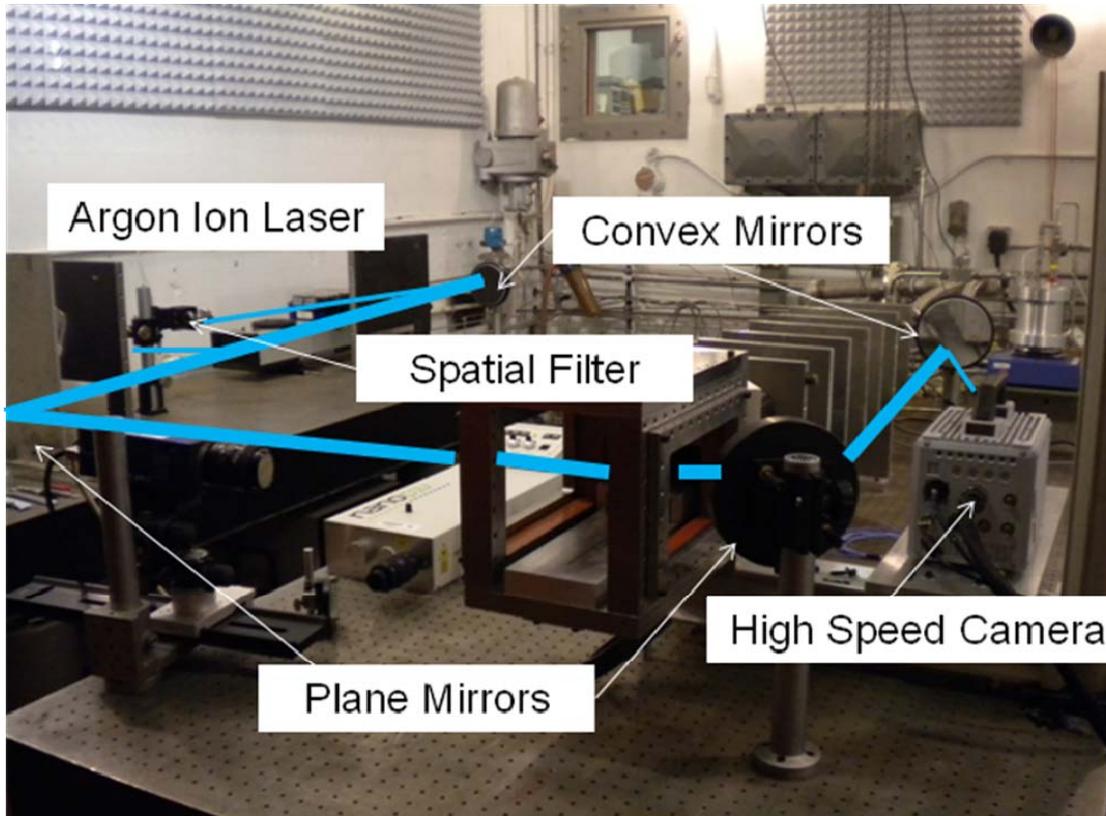
Figure 30.   Shadowgraph setup

K.   PARTICLE IMAGE VELOCIMETRY (PIV)

The PIV arrangement used a Litron Nd:YAG Dual Cavity pulsed laser 2 x 200 mJ at 532 nm with up to 15 Hz pulse rate with variable light optics. The laser sheet was passed underneath perpendicular to the flow through a narrow optical slot   Image as seen in Appendix B. Image capturing was done using a Lavsion Imager Pro X 2M 1648 x 1214 pixel resolution camera fitted with a 50 mm f1.4 Nikon lens and 532 nm filter. Laser and camera timing was accomplished using a PC based programmable timing unit (PTU–9). All image post-processing was completed with DaVis software installed on a standard quad core PC.

In order to properly seed, a reacting and detonating proper seed material would be required to withstand high temperature ad pressures while also exhibiting minimum interference to the flow. Micron particle Titanium Dioxide

was selected for its good stability at high temperatures and its relative inertness. As eluded to earlier manifold flow seeding was accomplished using the Lavision's Particle blaster 100 and titanium dioxide seeding particles. Since testing involved simultaneous PIV and shadowgraph, the PIV camera was angled out of the shadowgraph optical path, requiring calibration within the DaVis software
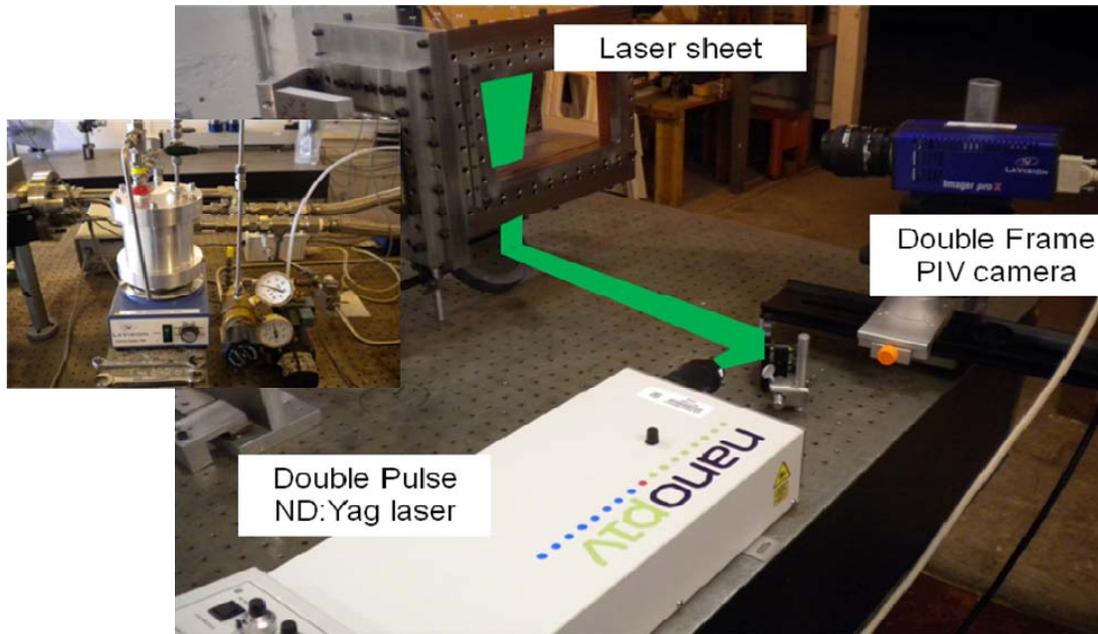
Figure 31.   PIV setup

L.   OPTICAL SECTION TEST CONFIGURATIONS

There were five major test configurations: Configuration 1 consisted of open diffraction with no step sections and a series of cold flow tests. Configuration 2, 3 and 4 were single step diffraction setups of various height ratios; 5 and 6 were double step diffraction setups with two different height ratios. Figure 32 depicts common setup configurations.

Figure 32.   Single and double step configurations

V.   COMPUTATIONAL RESULTS

A.   OVERVIEW OF RESULTS

It was originally envisioned that the CFD portion of this thesis could potentially shed light and perhaps help us better understand the complexities of gaseous diffraction detonation wave phenomena while also assisting in the design of some of the components. Simulations in general were effective in forming a detonation given the various parameters but once the detonation front was formed, failure of the front during diffraction was not attained. Unfortunately, not one simulation was observed to completely fail across the diffraction plane and thus precluded us from any useful results in computational diffraction detonation.

Two main reasons were suspected for simulations that could not resolve a failing detonation front, namely poor mesh resolution and the reduced chemistry sets utilized.   Poor Resolution (causing artificial reactivity) resulted in an unresolved the triple shock system at the front.   Incorrect chemistry could not predict the proper heat release and ignition delay time (induction time), as well as not enough diffusive elements in the simulation. This resulted in solutions that were overly reactive and not capable of failure during a diffraction event.

Simulations for the smallest mesh size of 0.05 mm used for the study ran for roughly 240 hours on 128 processors on the new NPS hamming Linux cluster, while the largest mesh sizes took only 24 hours to run with the same computational settings.   CFL number for all simulations was in between 0.5 and 1 and with varying time steps depending on the mesh size.   Table 3 is a summary of all the computed cases.

Table 3. Summary of computed results with ATM initial conditions

Run #	Mesh Size (mm)	φ	Reduced Chemistry Set	Numerical Scheme & other settings	Result
1 –23jul	0.05	1	Kurkov Burrows	Implicit, CFL 1	No failure
2 –26jul	0.1	1	Kurkov Burrows	Implicit, CFL 1	No failure
3–16aug	0.1	1	Kurkov Burrows	Explicit, CFL ramped 0.5–1	No failure
4–20aug	0.05	1	Kurkov Burrows	Explicit, CFL 1, IC $1.5P_{cj}$	No detonation
5–23aug	0.05	1	Kurkov Burrows	Explicit, CFL 1, IC $2P_{cj}$	No failure
5–23aug	0.05	1	Kurkov Burrows	Explicit, CFL 1, IC $2P_{cj}$	No failure
6–27aug	0.05	1	Kurkov Burrows	Implicit, CFL 1, LHS dissipation	No failure
7–30aug	0.05	1	Kurkov Burrows	Implicit, CFL 1, LHS dissipation, IC $1.5P_{cj}$, viscosity on walls	No detonation
8–31aug	0.05	1	Kurkov, Burrows	Implicit, CFL 1, LHS dissipation, IC $2P_{cj}$, viscosity on walls	No failure
9–2sep	0.05	1	Modified Kurkov Burrows	Implicit, CFL 1, LHS dissipation, IC $2P_{cj}$, added NO chemistry	No failure
10–7sep	0.05	1	Modified Kurkov Burrows	Implicit, CFL 1, LHS dissipation, IC $2.5P_{cj}$, viscosity on walls, added NO chemistry	No failure
11–10sep	0.05	0.8	Modified Kurkov Burrows	Implicit, CFL 1, LHS dissipation, IC $2P_{cj}$, added NO chemistry	No failure
12–1oct	0.05	0.8	Modified Kurkov Burrows	Implicit, CFL 1, LHS dissipation, IC $2P_{cj}$, added NO chemistry, symmetry plane	No failure
13–2oct	0.05	0.6	Modified Kurkov Burrows	Implicit, CFL 1, LHS dissipation, IC $2P_{cj}$, added NO chemistry, symmetry plane	No failure
14–12oct	0.05	0.6	Modified Kurkov Burrows	Implicit, CFL 1, LHS dissipation, IC $2P_{cj}$, added	No failure

					NO chemistry	
15–26oct	0.05	1	Modified Kurkov Burrows		Explicit, CFL ramped from 0.5 –0.95, ran faster, $2P_{cj}$, added NO chemistry	No failure
16–5nov	0.05	1	Hanson, Peterson		Explicit, CFL ramped from 0.5 –0.95, ran faster, $2P_{cj}$, added NO chemistry	No failure
17–16nov	0.05	1	Hanson, Peterson		Explicit, CFL ramped from 0.5 –0.95, ran faster, $2P_{cj}$, added NO chemistry, symmetry plane	No failure

B.   DETONATION FRONT STRUCTURE

The following figures show the computed contours of pressure, OH mass fraction, pressure and temperature plots for 0.1 mm and 0.05 mm mesh sizes. The combustion front at these resolutions did not capture enough front details. Best resolved fronts came from the OH contours at the finest resolution.

Upon first inspection at the detonation front on the OH mass fraction contours right before the diffraction plane, the front appears to lack real sharpness of a triple point that we would normally from a two dimensional simulation. Very faint keystone structures were only observed with a 0.05 mm mesh. There was no defined zone where the three shocks meet. Looking at Pintgen's extensive PHD work using planar laser induced florescence (PLIF) of the OH radicals he revealed their presence near the front in the distinct keystone patterns is clear in Figure 33.

.
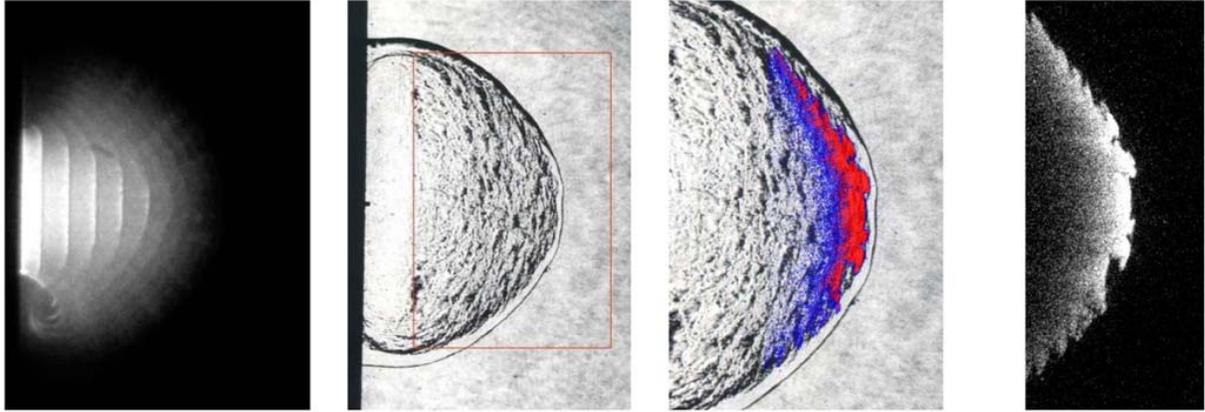
Figure 33.   Observations in the sub-critical regime, combined Shlieren, OH*
and PLIF imaging of the highly irregular H_2–N_2O mixture (From [18])

The H_2 N_2O mixture in Pintgen work has a much more irregular cell structure and is much more reactive than our H_2 air case with cell sizes averaging 1–4 mm. We use the case only to compare irregular and subcritical type trends. Normally during high temperature and pressure events, dissociation occurs immediately after shock passage resulting in high mass fractions in vicinity of the front, this is just barely apparent with these contours. A run with a 5µm mesh size or smaller would have been attempted except that but such runs would have taken months for results with NPS' current computational resources and would not have been feasible given current time constraints. It is understood that for structured meshes a 5 µm resolution has been reported as the starting point for adequate detonation front structure [21]. Looking at Figure 34 OH mass fraction contour plots, there are drastic improvements in front details moving from 100 µm to a 50 µm structured mesh—regrettably, not enough to resolve any jagged edges or keystones that we can clearly see in Pintgen's results.
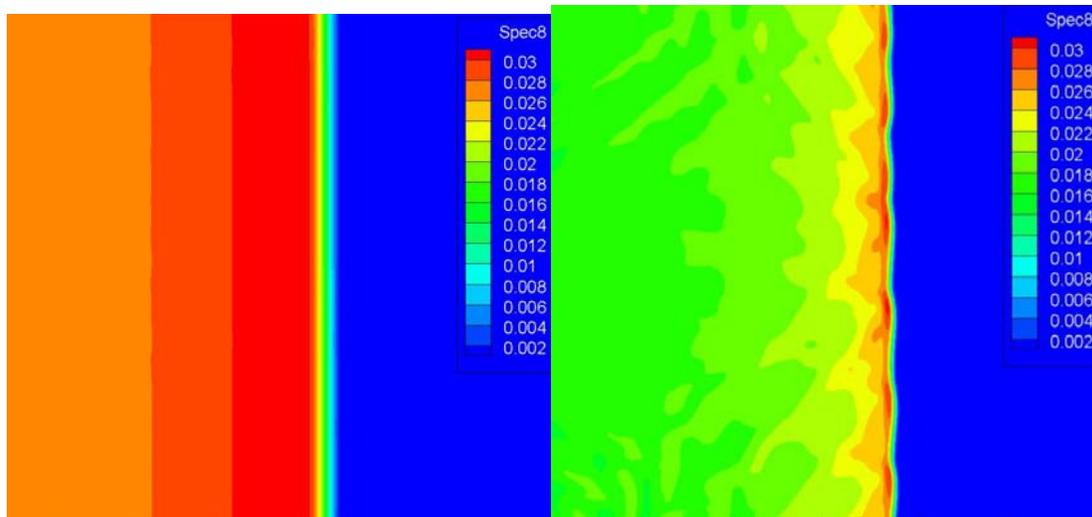
Figure 34.   Mass fraction OH contour plots of detonation front using a 100 μm and 50 μm structured mesh

With the pressure contours for all three mesh sizes, we can measure detonation cell size λ from remnant transverse pressure waves right behind the front. It is interesting to note that average cell size in each mesh size seem to be consistently smaller then experimental values of 1.5 cm for Hydrogen. For our baseline case with a mesh size of 50 μm, we found an average cell size of 0.22 cm, indicating a much more reactive mixture. Many researchers have reported that in order to computationally acquire accurate cell size, proper grid resolution is critical. Poor resolution has also been known to cause smaller than normal detonation cell sizes and in other words a much more reactive mixture. Given the computational constraints we could not confirm this since we did not run the 5μm mesh case. Transverse waves also revealed some additional irregularities; they seemed to persist much longer after the front had passed than normal. They occurred much more regularly then one would expect for such an irregular mixture like H_2–Air. Pressures in and around the front were on average 20% higher for both Von Neumann and CJ pressures. This was expected since nitrogen chemistry was not included.
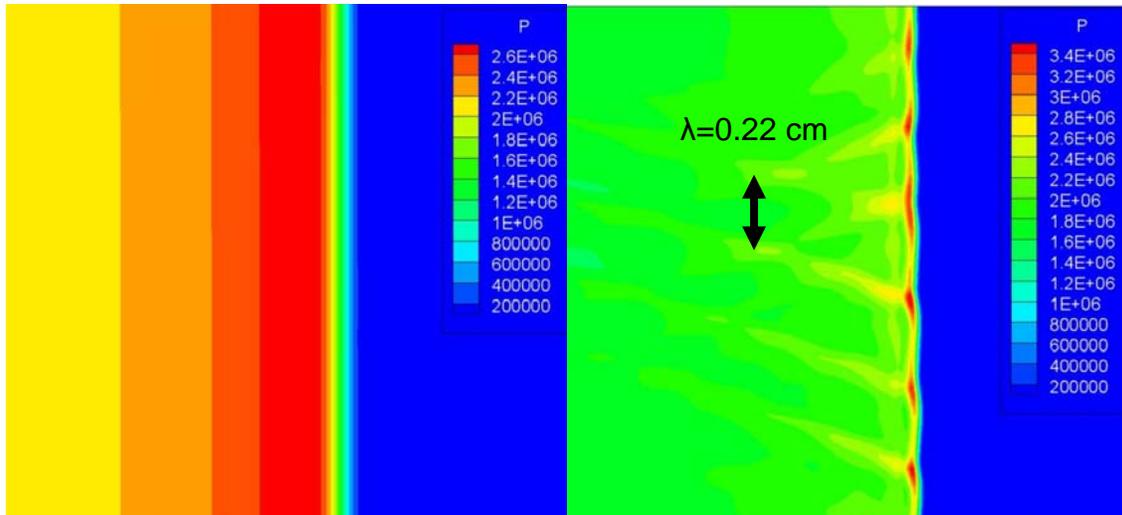
Figure 35.   Pressure contour plots of detonation front using a 100 μm and
50 μm structured mesh

Synonymous with detonations was also the turbulent nature of the reaction zone. Viscosity and transport effects played an extremely vital function within the small scale phenomena of the detonation structure. None of this detail is apparent at this mesh size in any of the contours. No shear layers were observable. Metacomp, maker of CFD++ stress that their Euler solver settings employ a behind the scenes dissipation parameter built in the code. We could not verify whether this had any effect.
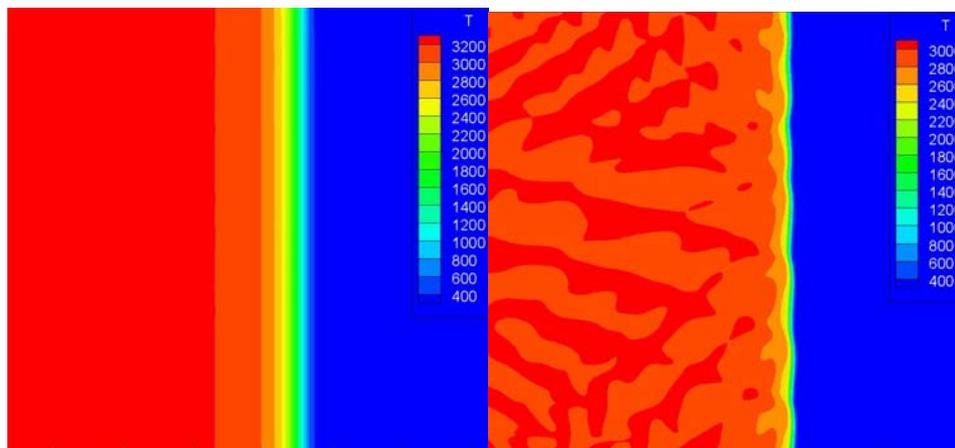

Figure 36.   Temperature contour plots of detonation front using a 100 μm and
50 μm structured mesh

Inspecting H_2 mass fraction contours also show scarce signs of unburned pockets of hydrogen right behind the front. Based on the literature, this has been observed experimentally and has been confirmed computationally. Lee explains that local fluctuations of the main shock front during the low velocity phase of the cycle can increase induction times resulting in later heat release after the front. Many irregular fuels can have significant levels of unburnt reactant.

C.   CHEMICAL KINETICS

Initial runs used the Kurkov and Burrows chemistry set for hydrogen as an initial investigation to see whether a chemistry set developed for supersonic low pressure combustion could be utilized in a detonation environment. However, we soon discovered this set was not the most ideal set, as diffractions set forth into unconfined areas would not completely fail with our smallest structured mesh. Granted it is also suspected that this may be a product of an over reactive mixture at the current grid resolution. Further investigation was deemed required at this point.

The Hanson and Peterson set was the last iteration, this reduced set was exclusively created for high pressure detonation for ram accelerator type combustion events. Unfortunately, results were not as promising as hoped, since an average was taken for 4 reaction equations, and since they were non-Arrhenius and could not be readily inputted into CFD++. These simulations also were unsuccessful in producing a failure in the diffraction front.

Detonation velocity between the various chemistry sets was compared and determined for a number of runs based on a finite difference method by measuring the front change in position between two time steps, see Table 4 some the typical values calculated. Values were on the order of 5%–10% percent higher than the CEA calculated values. This was expected as the nitrogen chemistry was omitted for all Kurkov & Burrows chemistry sets.   Our

51

modified Kurkov set included a one step NO equation which was hoped to slow down the chemical kinetics. Velocities were slower but the code still was not able to resolve a failing diffraction.

Table 4.   Calculated detonation velocity with CEA calculated values

Run #	Mesh Size (mm)	φ	Reduced Chemistry Set	Numerical Scheme & other settings	Avg Detonation Velocity (m/s)
6–27aug	0.05	1	Kurkov Burrows	Implicit, CFL 1, LHS dissipation	2010
7–30 Aug	0.05	1	Kurkov Burrows	Implicit, CFL 1, LHS dissipation, IC $1.5P_{cj}$, viscosity on walls	2000
11–10sep	0.05	1	Modified Kurkov Burrows	Implicit, CFL 1, LHS dissipation, IC $2P_{cj}$, added NO chemistry	1910
CEA		1		NASA Chemical Equilibrium V_{cj}	1964
CEA		0.8		NASA Chemical Equilibrium V_{cj}	1816

D.   DETONATION DIFFRACTION CONTOUR PLOTS

All simulations exhibited critical diffraction characteristics even though all conditions were sub critical. All detonations undergo some partial failure which starts almost immediately at the open step but inevitably a re-ignition event occurred at some point, reenergizing the entire detonation. Pressure, Temperature and OH mass fraction contour plots at one mid time step attest to the some of the true complexity of the flow system. Near the main axis of the channel the flame front never really appeared to decouple from the precursor shock. However, the flame front at the corner completely decouples. Front speeds were observed as low as $0.8V_{cj}$ near the corner to as high as $1.2V_{cj}$ and do not ever seem to slow down at the core from the diffraction event. Note the vortex at the as seen by the by the streamlines due to rapid lateral expansion.
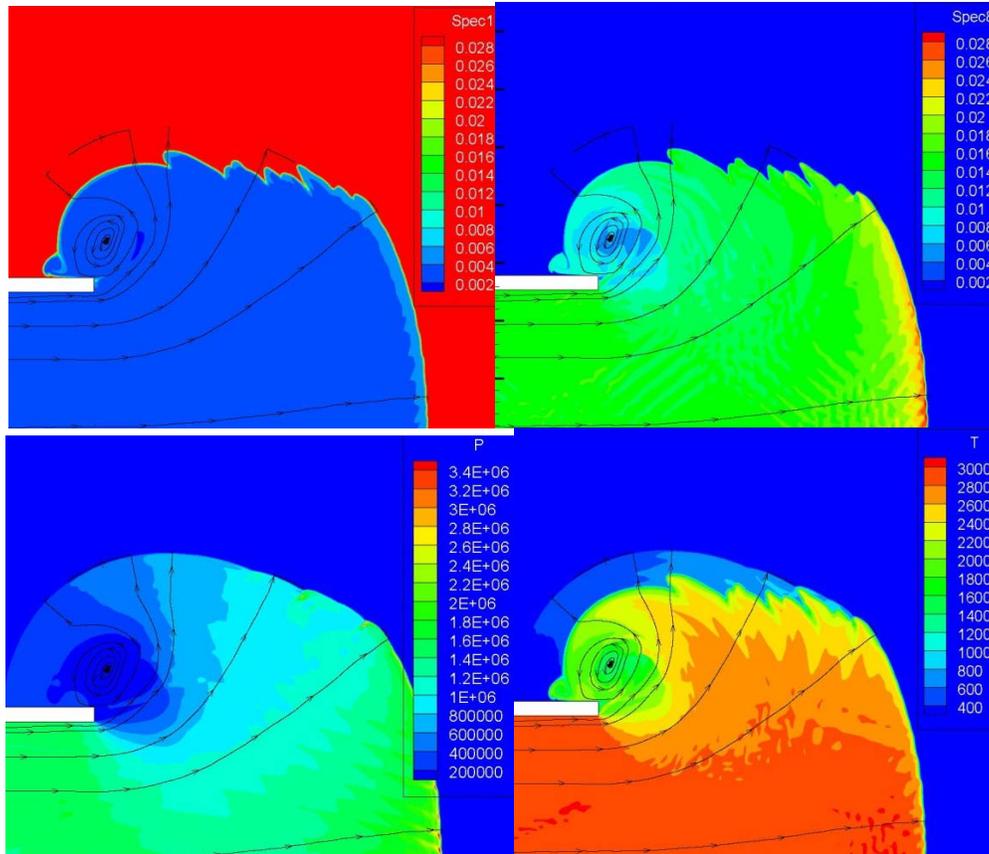
Figure 37.   From left to right H_2, OH mass fractions, pressure (in Pa)
temperature (in K)

The following two figures chronicle the detailed re-ignition of the front for the standard case with time sequenced pressure and temperature contours. As the wave works its way past the corner, a rarefaction wave originates almost immediately from the open corner begins to works its way down at an angle of 30 degrees and works to begin a decoupling of reaction front to precursor shock. By frame 6, the rarefaction wave was fully into the reaction zone and sweeps across the front starting to flatten it and adding curvature.

All simulations exhibited a decoupling shock and reaction front from the diffraction front followed by a reinitiation event as seen in the above Figures. It should be noted that even though reinitiation occurs, the shock never completely decoupled. We really only observed localized explosions resulting from

rarefaction and transverse wave collisions. This event then triggers a reaction across the unreacted zone or shell. Recoupling of the shock and reaction front then spreads over the entire front. Before any localized explosion, unburned reactants slightly affected by a precursor shock find themselves in a spherical zone between a flame front from behind and a transverse wave above. In this reinitiation event, it appears the detonation proceeds transversely across the chocked reactants in an azimuthally and polar manner of direction completing the reaction and reinitiating the entire front, as seen in both the time sequenced contours, Figures 38 and 39.
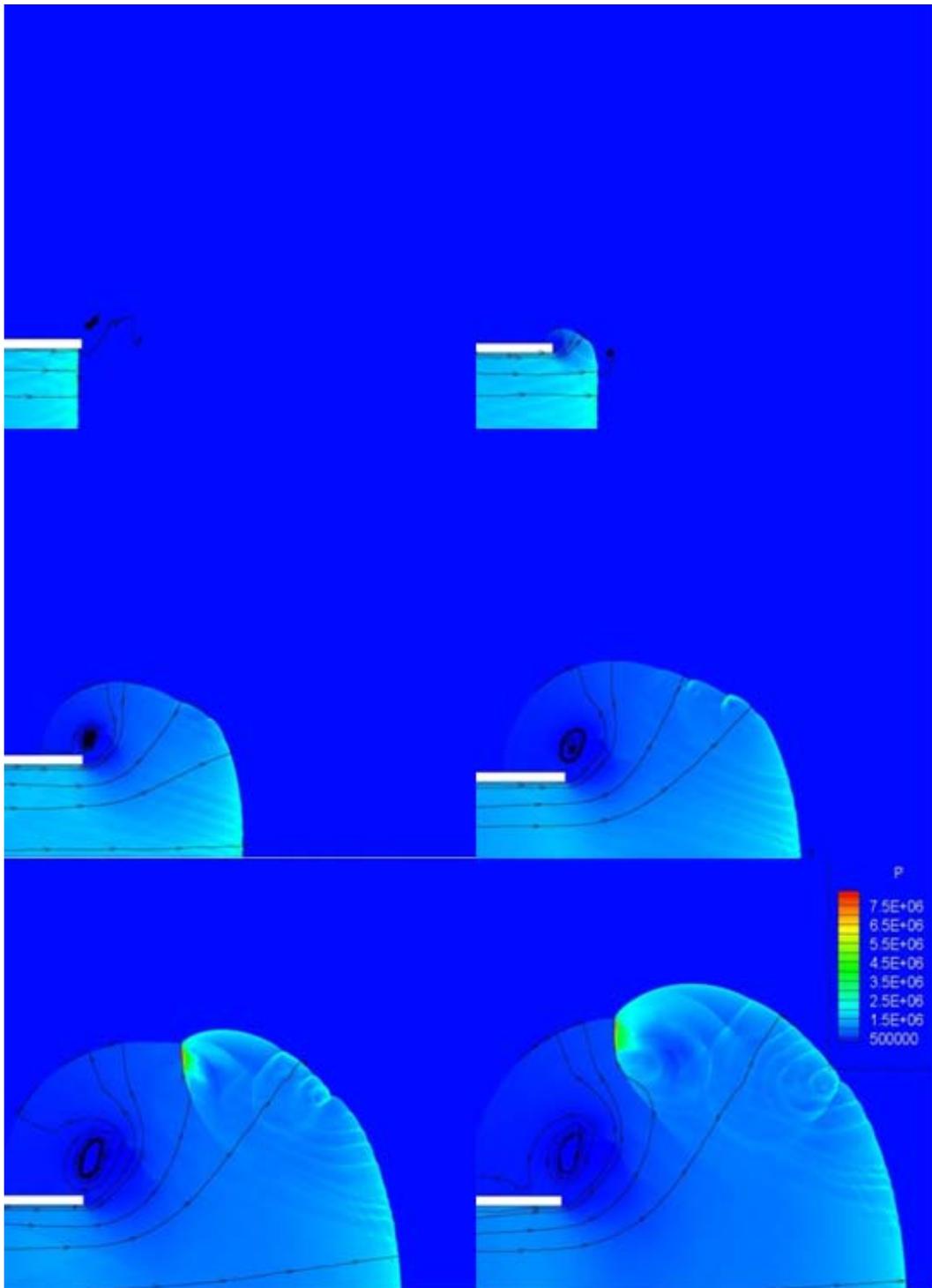
Figure 38.   Time sequence pressure contour plot with streamlines (in Pa)
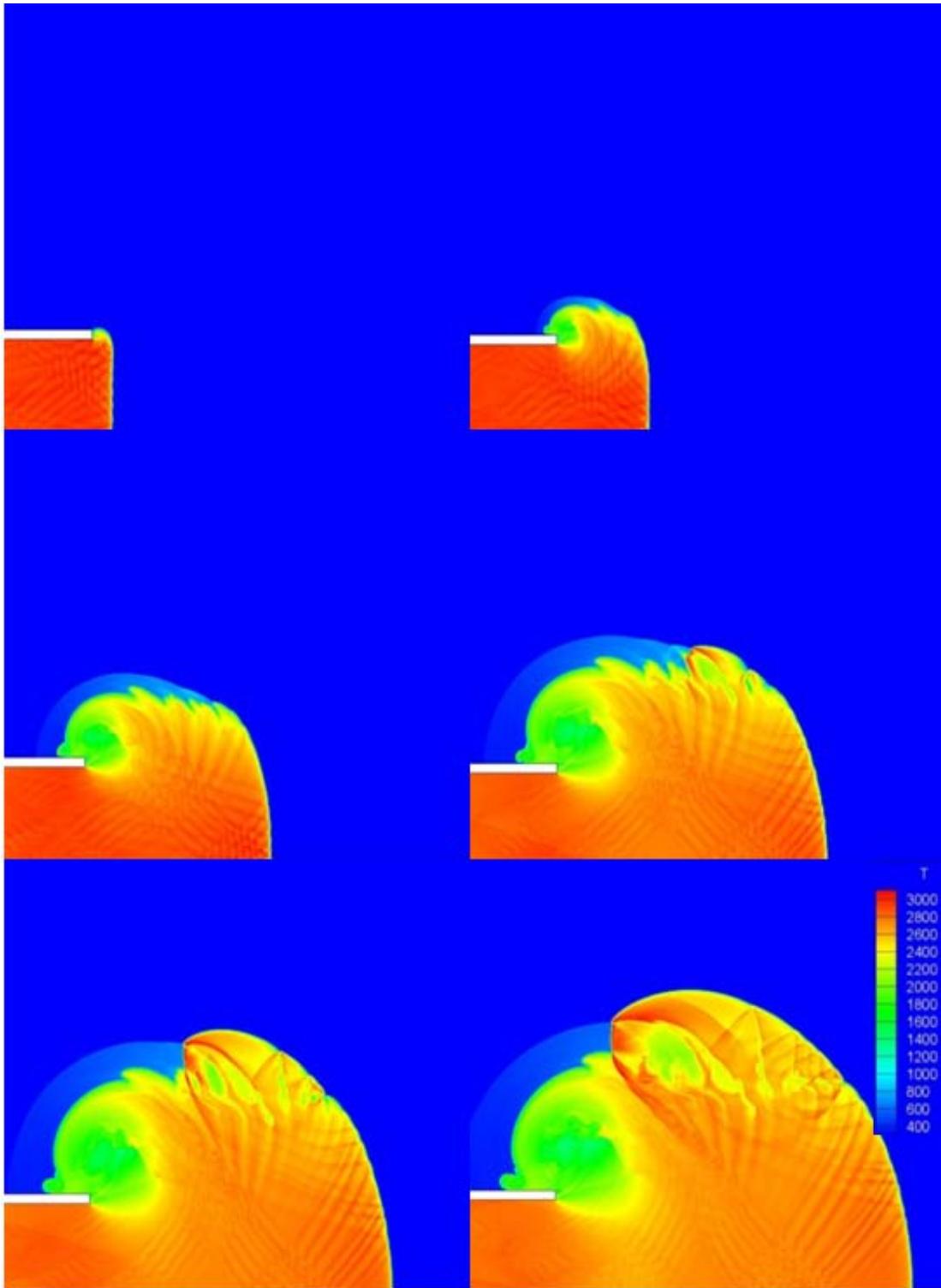
Figure 39.   Time sequenced temperature contour plots (in K)

VI.   EXPERIMENTAL RESULTS

A.   TESTING OVERVIEW

Table 5 depicts an overview of all experiments conducted with the split flow multi-stepped configured 1:3.5 aspect ratio channel. The tests comprised of detonating hydrogen and air at atmospheric conditions for various diffraction area ratios.

Table 5.   Experimental test matrix

Test #	Test Condition	Equivalence Ratio range	Diagnostic
1	No Step	0.75–1.5	Shadowgraph, PIV
2	1 Step 1:2.6 area ratio	0.75–1.5	Shadowgraph
3	1 Step 1:2.3 area ratio	0.75–1.5	Shadowgraph
4	1 Step 1:2.00 height ratio	0.75–1.5	Shadowgraph,
5	2 Steps 1:2.3 & 1:2.3 area ratio	0.75–1.5	Shadowgraph,
6	2 Steps 1:2 & 1:2 area ratio	0.75–1.5	Shadowgraph, natural emmision

B.   PRESSURE DATA

Low speed pressure measurements were primarily used to calculate reactant fuel to air ratio for all tests. With pressure data, equivalence ratio was calculated based on the choked mass flow Equation 19, with main air flow using a 0.235 inch diameter orifice plate while a 0.157 inch orifice was used for fuel

$$\dot{m} = C_D \cdot \dot{m}_{ideal} = C_D \cdot \frac{A_2 p_t}{T_t^{1/2}} \cdot \left\{ \left(\frac{p_2}{p_t} \right)^{2/\gamma} \cdot \left[1 - \left(\frac{p_2}{p_t} \right)^{(\gamma-1)/2} \right] \right\}^{1/2} \cdot \left[\left(\frac{g_c}{R} \right) \cdot \left(\frac{2 \cdot \gamma}{\gamma - 1} \right) \right]^{1/2}$$

(19)

By obtaining a ratio of mass flow rates for both air and hydrogen, the equivalence ratio could be determined with reasonable errors of about ±5%. Discharge coefficient C_d for both orifice plates was found to be 0.61 using the CRC handbook for mechanical engineers. These results were also in good agreement with measurements derived PIV flow rates.

High-speed pressure probe data was acquired using Labview and detonation speeds were determined by measuring the inter peak distance with time taken into account the probe spacing of 0.241 m. Typical plots obtained can be seen in Figure 40. Typical wave speeds ranged from 1,800±50 m/s to 2,100±50 m/s and agreed very well with wave speed calculated from high speed camera imagery and CJ wave speeds calculated from CEA.
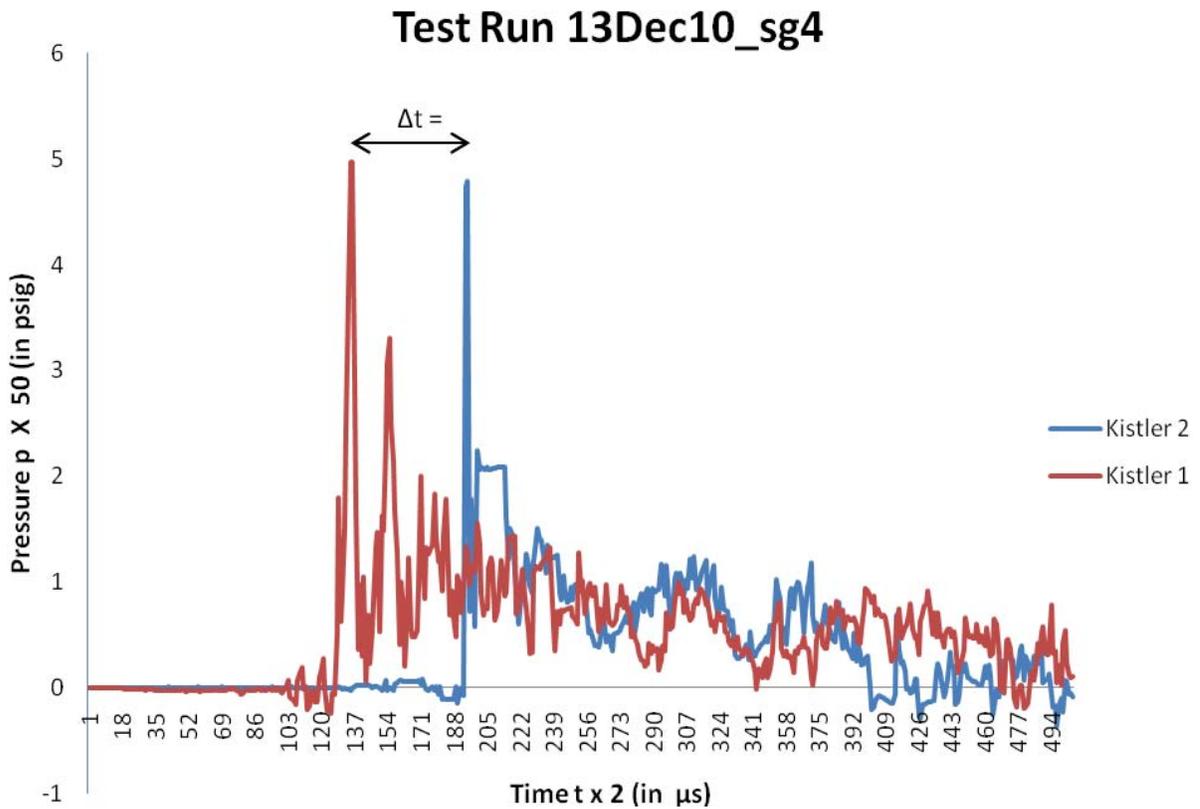
Figure 40.   High-speed pressure data

C.   RESULTS OVERVIEW

Figures 41 and 42 represents a summary of all tests performed.   The channel performed best at an area ratio of 2 for a wide range of equivalence ratios for both single and double step configurations. It was marginal for the ratio of 2.3 and did not transmit for any area ratios of 2.6.   We present the data in terms of area ratios since we are dealing with a channel that is not perfectly flush with the optical section, its support members are a half-inch thick all around so there is some diffraction occurring in the z–direction.
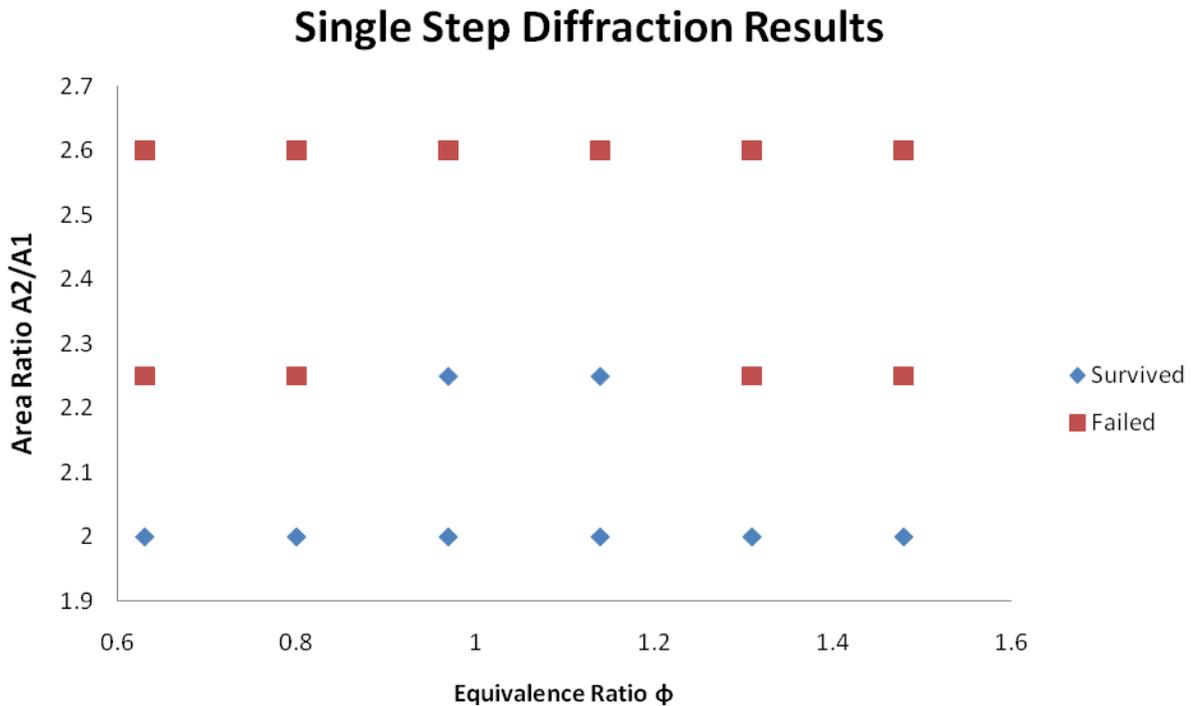
Figure 41.   Single Step diffraction results with Channel Area Ratio

Detonations transmit into the double step area ratio of 2 for three of the six equivalence ratios tested and did not transmit using a double 2.3 ratio, seen in Figure 42.

Double Step Diffraction Results
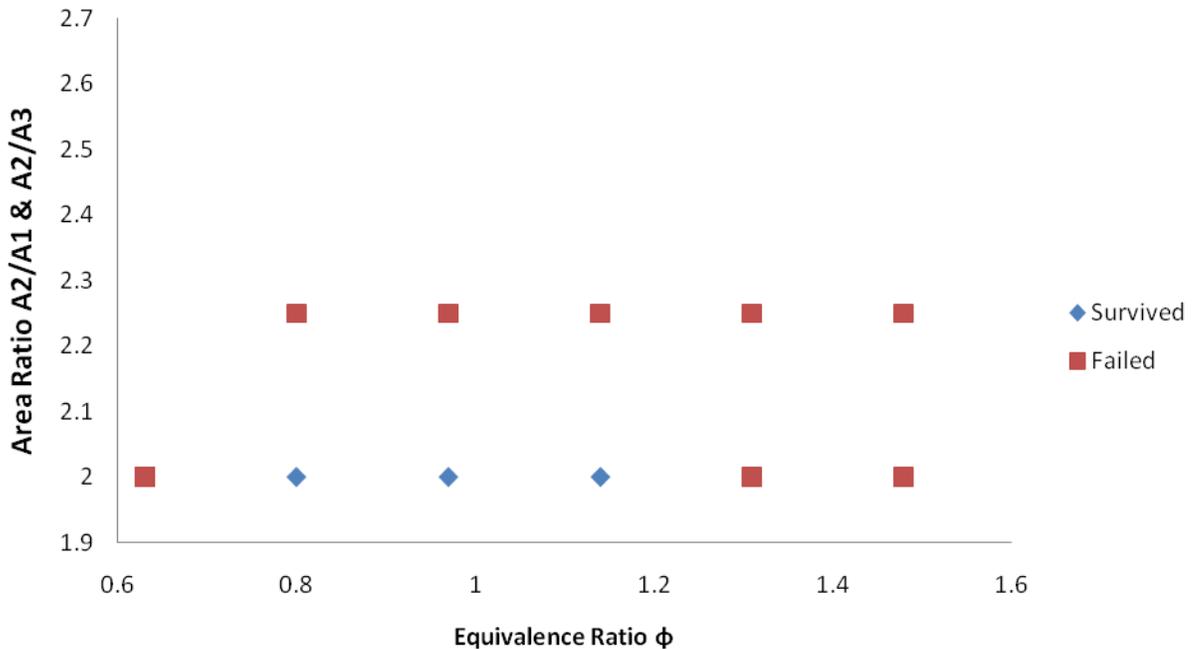
Figure 42.   Double step diffraction results with Channel Area Ratio

Based on shadowgraph imagery, centerline detonation velocity relative to CJ velocities was calculated with respect to distance from the first diffraction plane for a number of equivalence ratios and presented on 6 of the following Figures.   Figures 43, 44 and 45 depict wave velocities just after the first diffraction plane at three equivalence ratios ranging from lean to rich with our one step configuration for varying height ratios.   The area ratio of 2 performed well under all conditions as observed to reinitiate well before the second diffraction plane (located 3.75 x/h main channel heights away) coming out of the first diffraction plane as wave speed were close to CJ velocity. After the second plane the wave diffracted into an open space and maintains good strength for another 2 height distances. Area ratios of 2.3 did not fare as well, as the reinitiation seemed to occur at a later distance than 3.75 x/h. Looking at the Φ=1 case there was a reinitiation that happened, but at that point the wave did not have enough time to completely form and gain enough strength to survive once it crossed the second

60

diffraction plane. It seemed that a good step height to length ratio was 2 times x/h, so long as the wave survives the initial expansion event. For our area ratio case of 2.3, the second step height is 2 inches and so our transition length should have been at least 4 x/h, allowing enough distance for a detonation to properly reform. Our 2.6 case did not survive the first diffraction as the expansion waves were given enough time and distance to penetrate the entire front enough precluding any recovery, in all reinitiation cases.
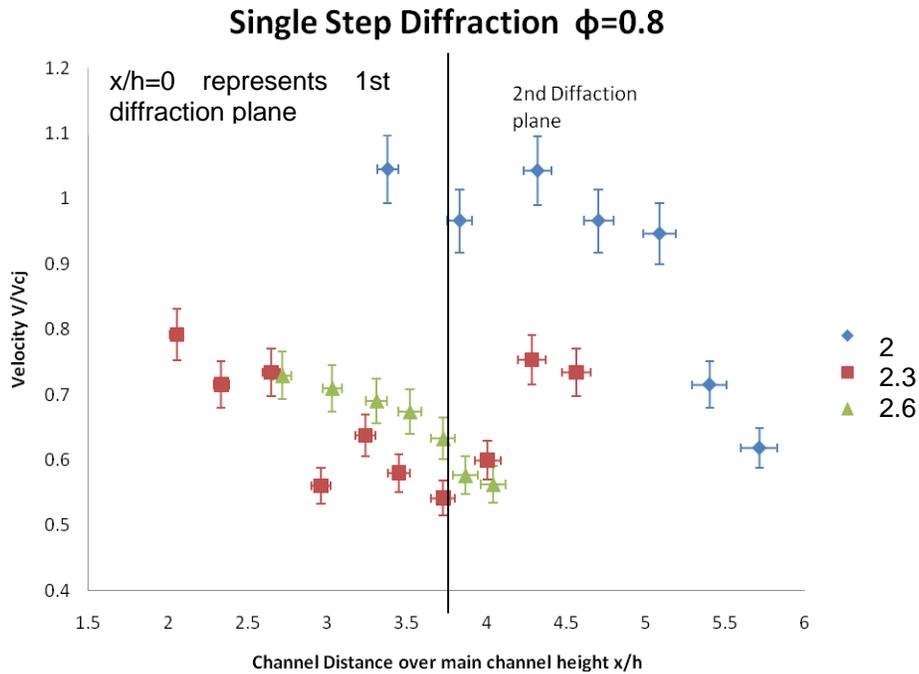

Figure 43.   Detonation velocity vs. run distance for different area ratios
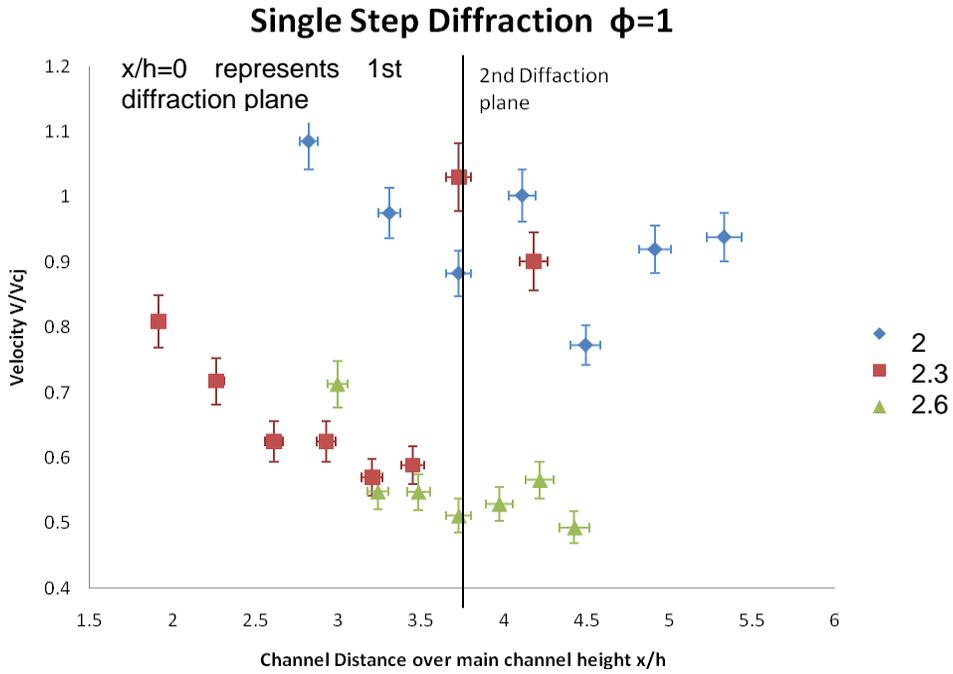
Figure 44.   Detonation velocity vs. run distance for different area ratios
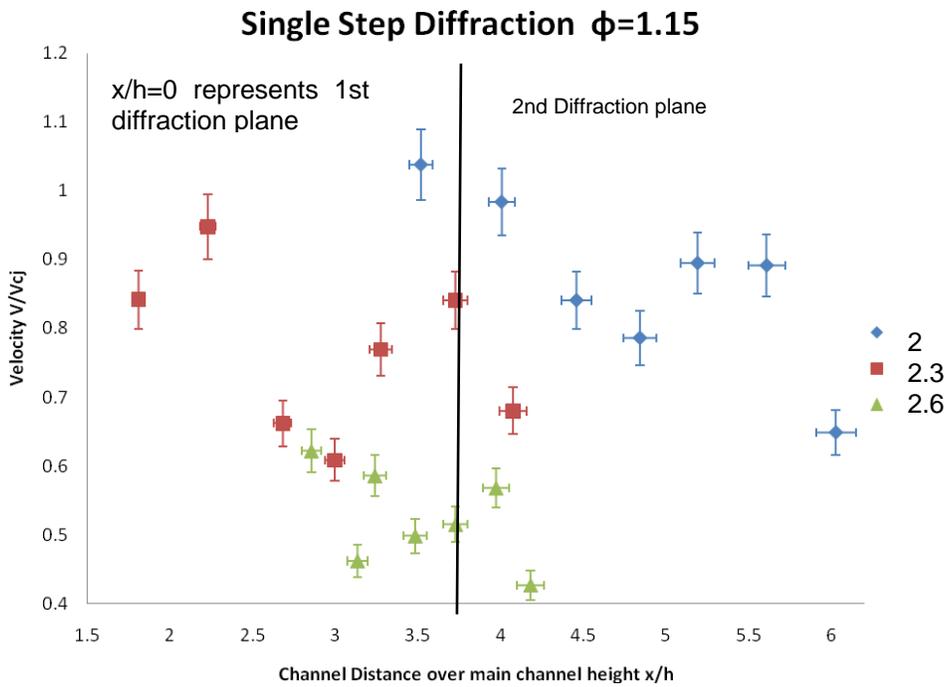
Figure 45.   Detonation velocity vs. run distance for different area ratios

Figures 46, 47 and 48 represent the results for both double step setups of Area ratio of 2 and 2.3. The double area ratio of 2 successfully transitioned both steps with velocities slightly higher in the 3.75–6 x/h zone then the previous case. The addition of another wall to created another shock to high impedance material interaction creating a Mach stem reinitiation zone due to the shock reflection. It should be noted that the range of equivalence ratios for survival was reduced. The double area ratio of 2.3 was not as successful. Longer step lengths to accommodate this ratio it may have resulted in successful reignition.
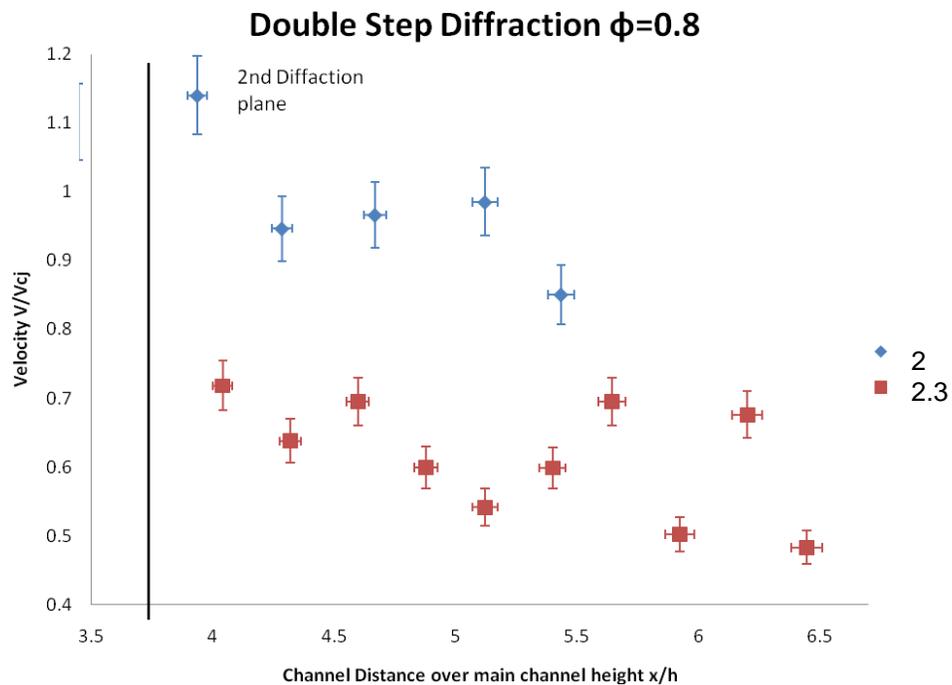
Figure 46.   Detonation velocity vs. run distance for different area ratios
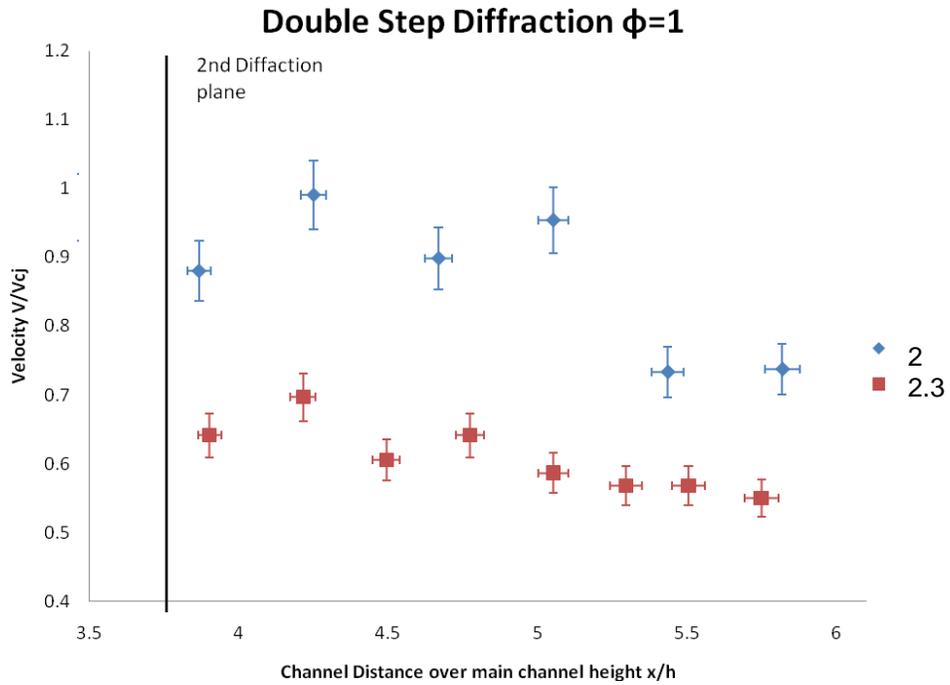
Figure 47.   Detonation velocity vs. run distance for different area ratios
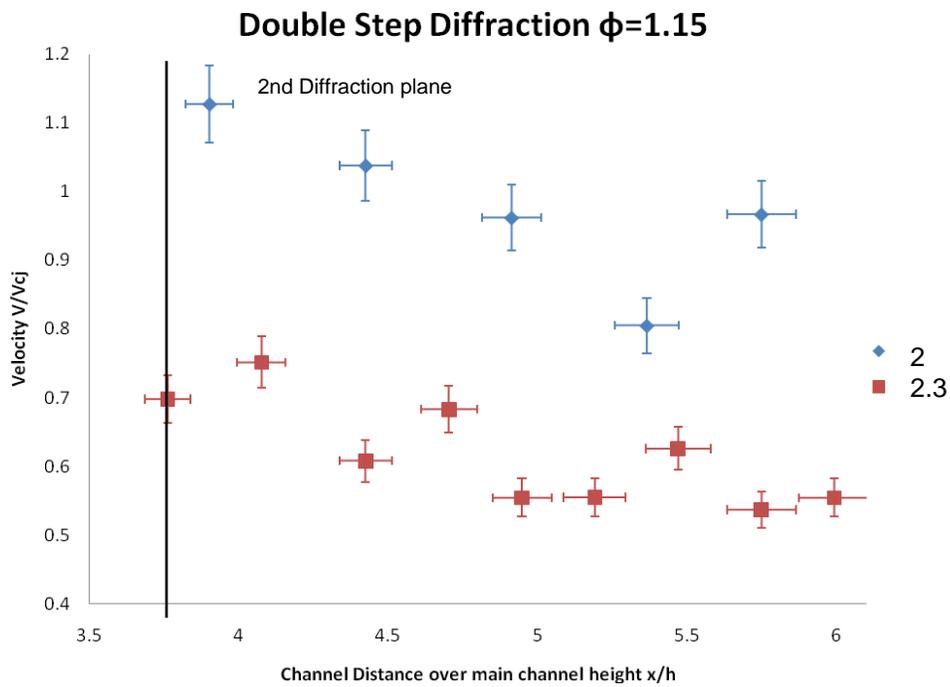
Figure 48.   Detonation velocity vs. run distance for different area ratios

D.   DIFFRACTION PREDICTION MODEL

A simple diffraction failure model was tested and validated with these experimental results.   Based on previous results both detonation cell size for hydrogen and air with respect to equivalence ratio and detonation velocities could be predicted for the various reactants as seen in Table 6. Knowing these parameters, our detonation channel's geometric dimensions and how critical our channel was for an aspect ratio of 3.5 we could predict the velocity deficit under these conditions [24].   We could also calculate either rarefaction angle from disturbance to undisturbed detonation α or a reaction zone velocity V_{rz} to the first step from Skews method [25], depending on what data was available.   In our case we calculated V_{rz} using Equation 20 and measured α based on the Shultz's high speed shadowgraph images of Hydrogen and air and our own shadowgraph images which was found to be 15 degrees [8]. Knowing our step distance and the distance required for total failure of the front, we could predict the health of the front by the time the wave hits the step wall. Degree of criticality in Table 6 refers to how many detonation cell widths we were across the cross section in a particular case with respect to the critical height for a 3.5 aspect ratio channel which is 7λ. For most cases, we were about 5 times smaller than this so called critical length. With this information, we could apply a velocity deficit linked to criticality [7].

$$\tan\alpha \ = \ \frac{v}{V_{CJ}} \ = \ \frac{\sqrt{c_{rz}^2 - (V_{CJ} - u_{rz})^2}}{V_{CJ}}$$

(20)
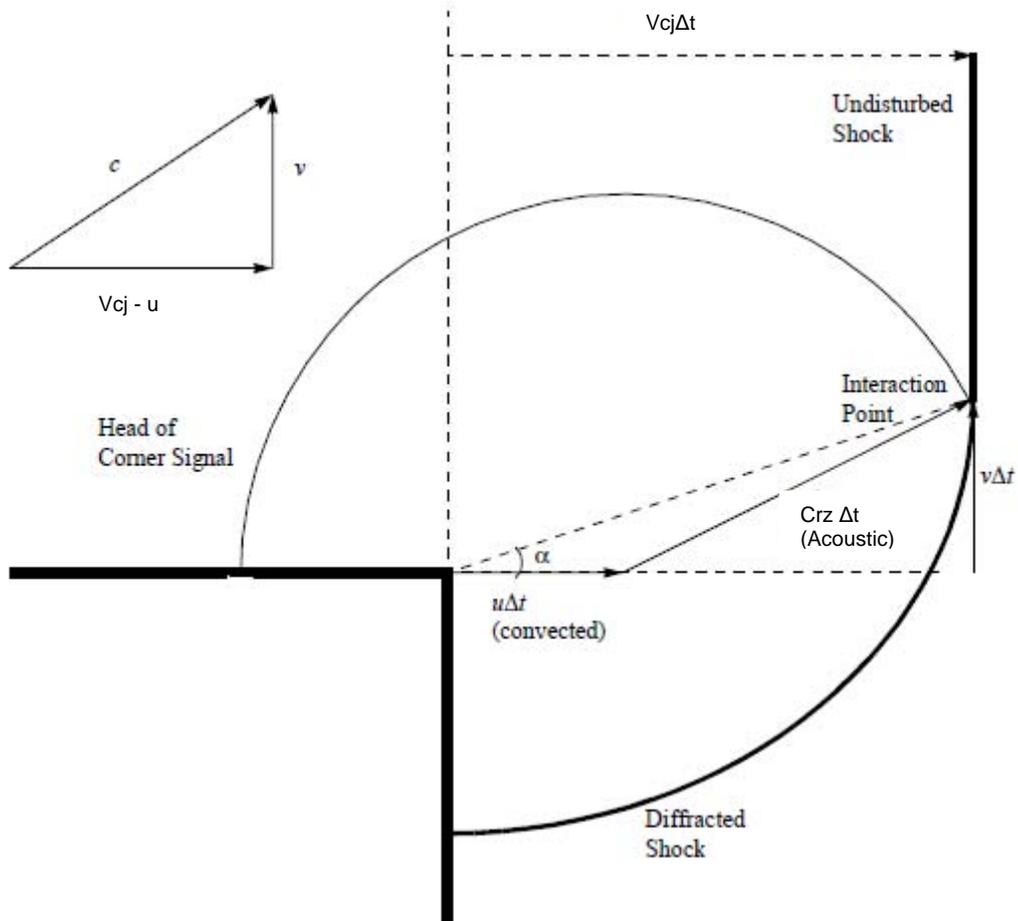
Figure 49.   Schematic of a diffracted shock (From [8])

Based on our experiments, it appeared that once the entire front had curvature the diffracted chock had no chance of survival. However, if some portion of the reaction zone was still coupled to the pre-cursor shock there was a chance of survival if a Mach stem developed quickly enough from the wall area and had time to progress into the rest of the front.

Our case with an area ratio of 2.6 failed every time experimentally and was predicted in our model. We also find experimentally that the front has already been completely disturbed, seen in Table 7. Whereas area ratio of 2 detonations survived every single step expansion experimentally and we predict that this wave was about 80% failed.

Table 6.   Predicted numerical results with α=15°, λcr=7

φ	λ (in cm)	λ's across area	λcr/λ's across (criticality)	area ratio (AR)	criticality /AR
0.8	2	1.25	5.60	2.00	2.80
0.8	2	1.25	5.60	2.30	2.43
0.8	2	1.25	5.60	2.60	2.15
1	1.5	1.67	4.20	2.00	2.10
1	1.5	1.67	4.20	2.30	1.83
1	1.5	1.67	4.20	2.60	1.62
1.15	1.7	1.47	4.76	2.00	2.38
1.15	1.7	1.47	4.76	2.30	2.07
1.15	1.7	1.47	4.76	2.60	1.83

Table 7.   Predicted numerical results cont.

φ	area ratio	Vcj (m/s)	V deficit (m/s)	v (m/s)	Time t to wall (s)	% failed	Exp results
0.8	2.00	1866	1810.02	905.01	4.88E−05	84.19	passed
0.8	2.30	1866	1810.02	905.01	5.61E−05	96.76	passed
0.8	2.60	1866	1810.02	905.01	6.35E−05	109.52	failed
1	2.00	1966	1946.34	973.17	4.54E−05	84.19	passed
1	2.30	1966	1946.34	973.17	5.22E−05	96.76	passed
1	2.60	1966	1946.34	973.17	5.91E−05	109.52	failed
1.15	2.00	2015	1974.7	987.35	4.48E−05	84.19	passed
1.15	2.30	2015	1974.7	987.35	5.15E−05	96.76	passed
1.15	2.60	2015	1974.7	987.35	5.82E−05	109.52	failed

E.   TEST CONDITION 1: COLD FLOW AND WIDE OPEN DIFFRACTION

Test condition 1 included all experiments that would help understand all the conditions the detonation front would be exposed to in the simplest configuration, i.e., diffraction into a wide opening without the stepped sections in the optical section.   Tests included basic PIV tests of the cold flow and diffractions into an open channel as well shadowgraph shots.

Cold flow tests were conducted to better understand the pre detonation flow conditions and seeding quality of the flow. Figure 49 was a typical test run with main air flow mass flow rate of 0.017 kg/s depicting camera bit count (intensity level) of the seed. The laser sheet illuminates an 80 mm by 80 mm zone in the flow immediately following the diffraction plane, flow moves from left to right. Note that these counts were slightly high as the bulk of the seed was biased towards lower main detonation channel. Although seed density was higher in this region than required at these low speed fills, it was found that such levels were required for sufficient seed density required for good vector correlation for wave speeds in the order of 2,000 m/s as such waves would tend to disperse the seed after the front, as particles can be accelerated to as much as 1,000 m/s just after the front applying significant seed density variations.
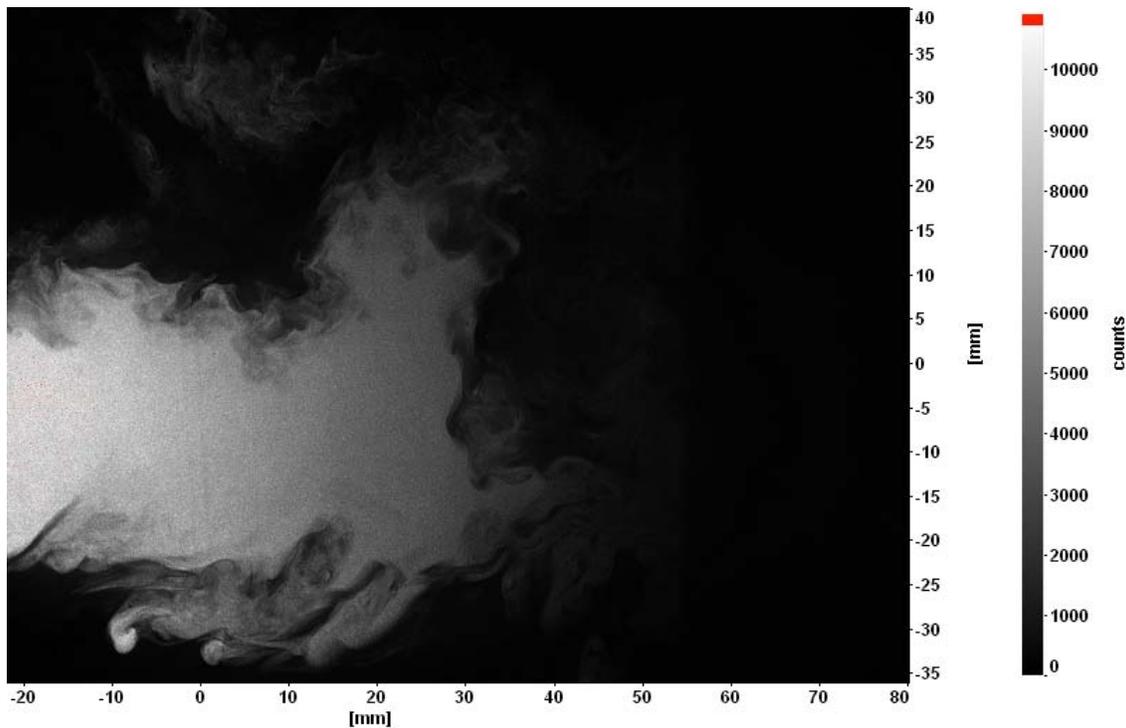
Figure 50.   Seed bit counts with low speed cold flow run

The postprocessed vector plot for Figure 50 can be seen at Figure 51. Flow on average was very turbulent and fluctuated significantly during the filling

process. On average, velocities in the top channel were higher by a factor of 2 compared to flow in the lower channel. A shear layer of lower velocity can be found in between both channels.
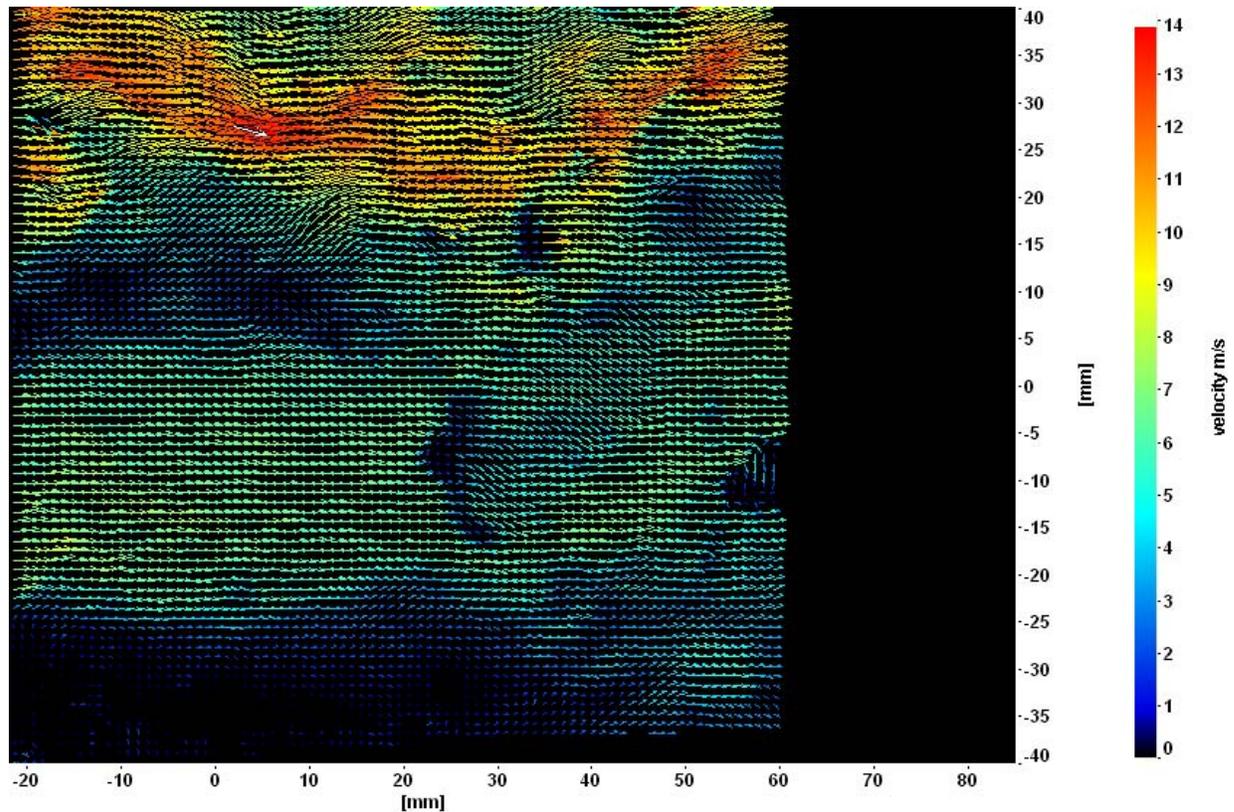
Figure 51.   Cold Flow PIV velocity vector plot

The following Figures depict PIV vector plots of one snapshot of the detonation front without any steps with a Φ=1. The first Figure is frame two of the two frame camera showing the good seed density in and around the diffracting detonation front. A pressure of 5 psig was applied to the seeding system for reasonable seeding density. Inter laser time was calculated in Davis, Lavision's in house PIV code based on estimated 800 m/s particle velocity behind the front, resulting in a 710 ns time deference between frames dt. The trigger delay was set to 230 µs and triggering was off of the first Kistler pressure probe with a laser power of 50% of max.

69

Figure 52 was the post processed vector plot of the flow field. We observed particle speeds in the 800 m/s range near the core dropping to as low as 400 m/s if we follow around the perimeter. Unfortunately, with such a small dt we missed capturing lower end velocities and similar test runs would be needed with various dt's to get the whole event. Additionally, because we used a low frame rate PIV speed system to capture detonations at various diffraction times many runs would have been required.
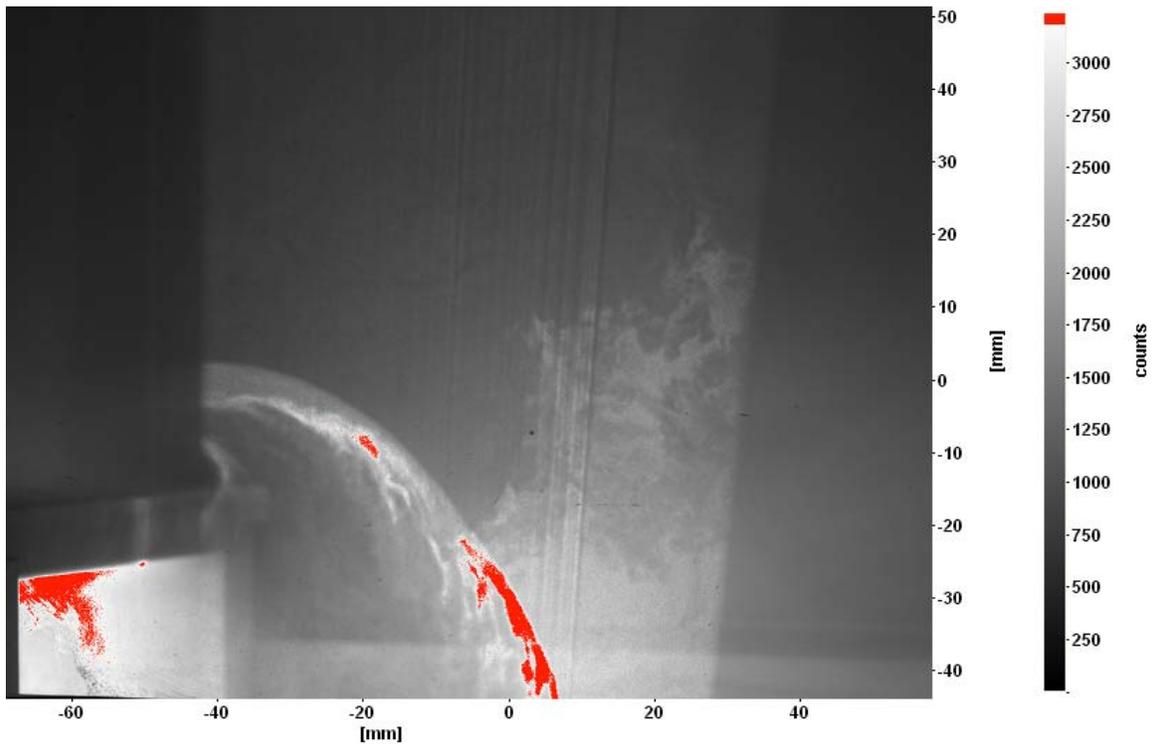
Figure 52.   Seed bit counts with high speed settings

The postprocessed plot was quite noisy around the front. It is suspected that fine tuning camera focus and seed density would have improved the proportion of noise and we would have obtained better correlation with calculated vectors.
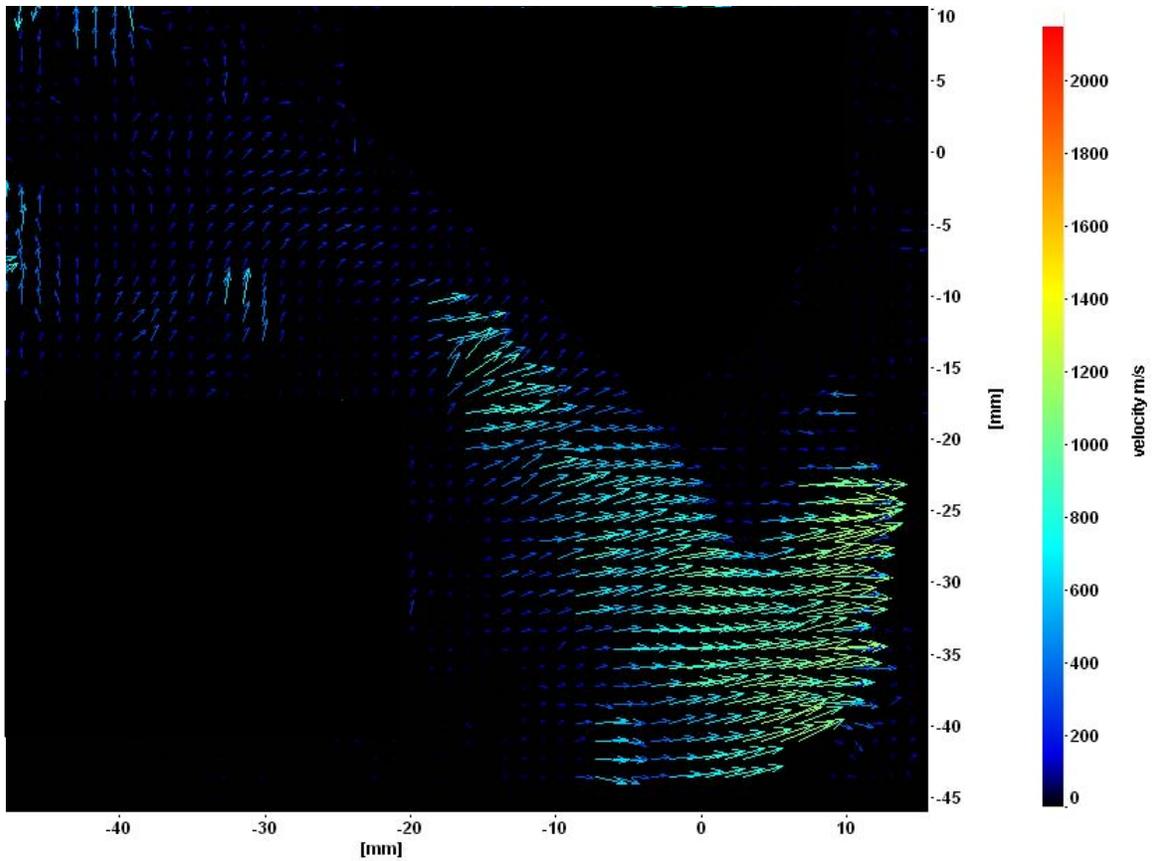
Figure 53.   Post processed vector PIV vector plot of a diffracting detonation front

Shadowgraph sequences were also taken without any step sections this can be seen in Figure 54. All images were shot at 150,000 frames per second with a total of 17 frames with the Ultra 17 high-speed camera system.
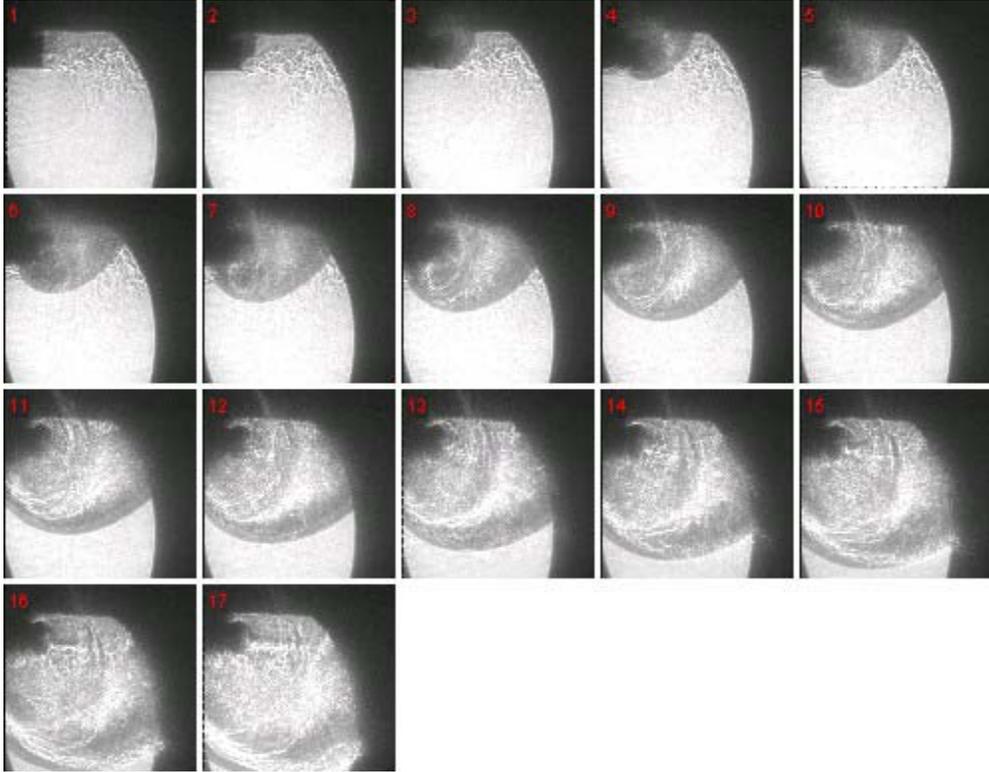
Figure 54.   Shadowgraph sequence of diffraction into unconfined area

## F. TEST CONDITION 2: SINGLE STEP AREA RATIO 2 WITH SHADOWGRAPH
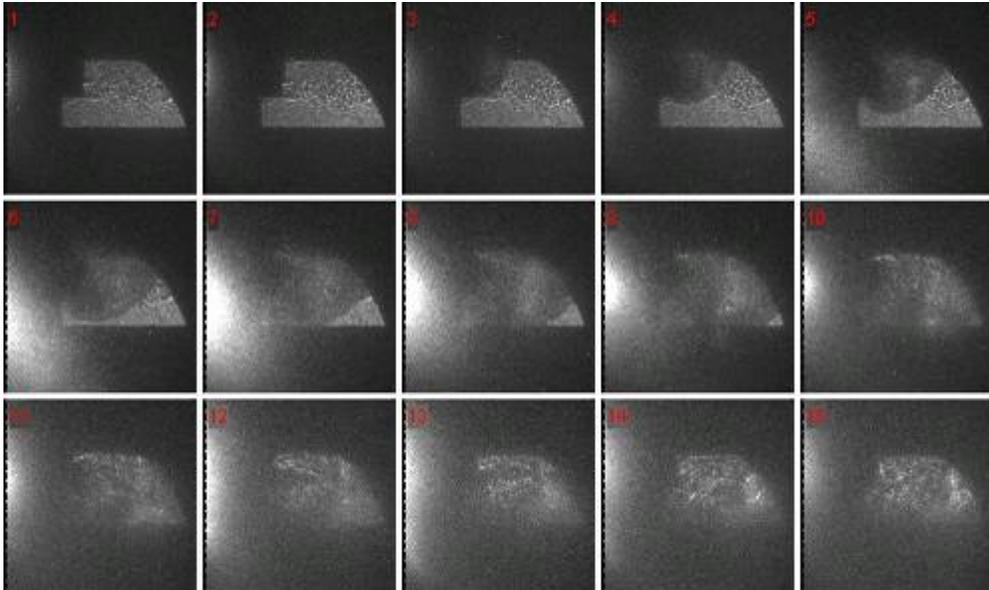

Figure 55.   One step, Φ=1, 2.00 A_2/A_1
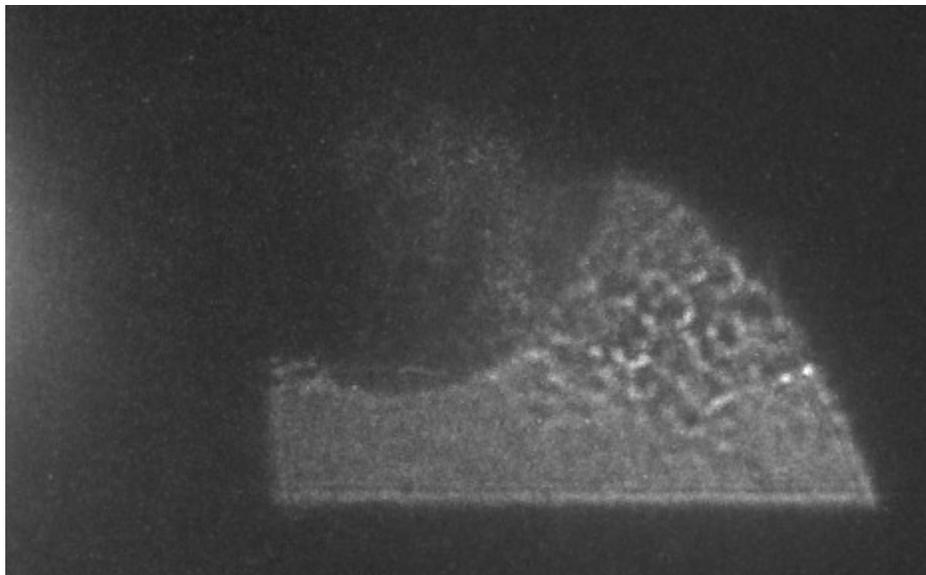
Figure 56.   Frame 4 From above, x/h 1–3.5

**G. TEST CONDITION 3: SINGLE STEP AREA RATIO 2.3 WITH SHADOWGRAPH**
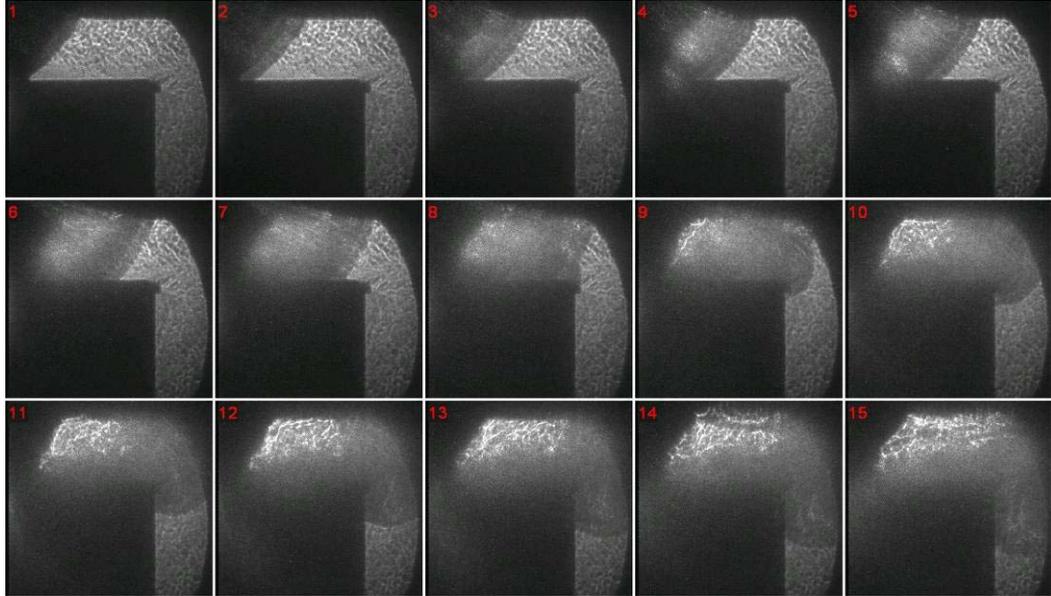
Figure 57.   One step, Φ=1, 2.30 A_2/A_1
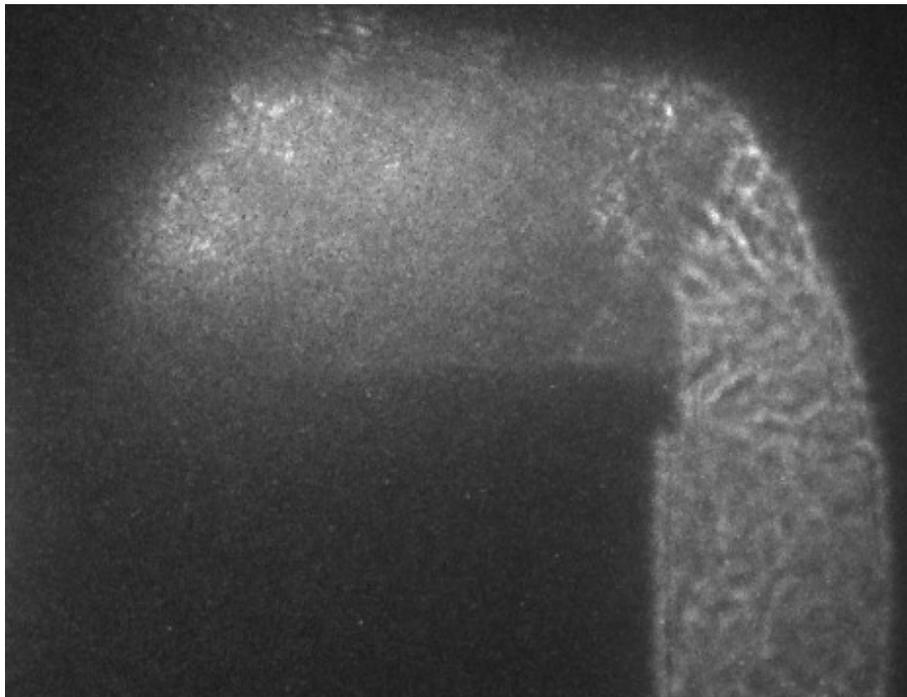
Figure 58.   Frame 8 from above, x/h 2–4.5

74

H. TEST CONDITION 4: SINGLE STEP AREA RATIO 2.6 WITH SHADOWGRAPH
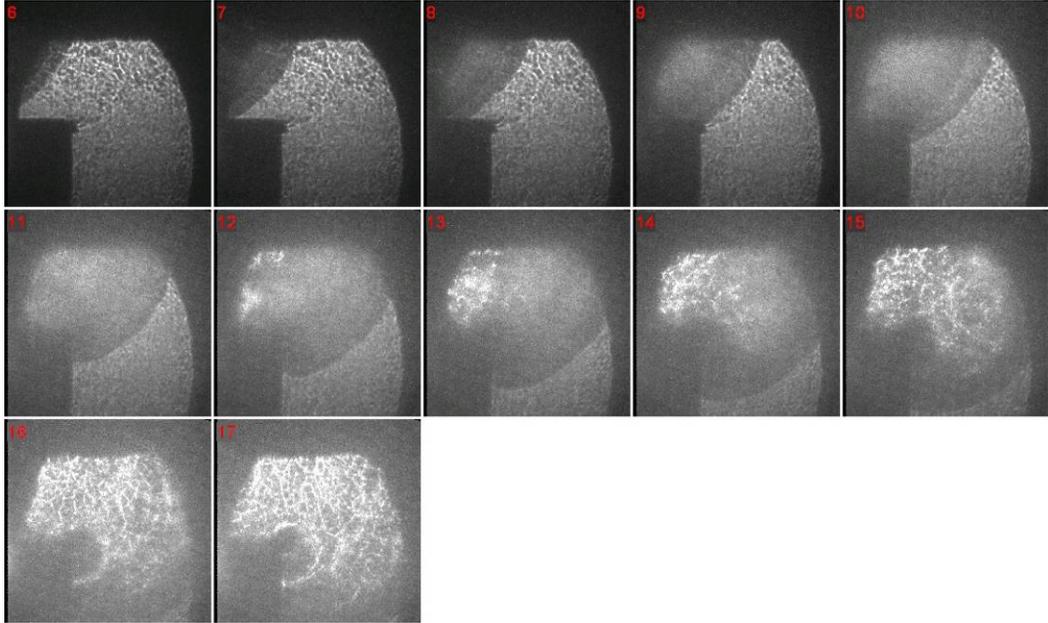

Figure 59.   One step, $\Phi=1$, 2.6 A_2/A_1
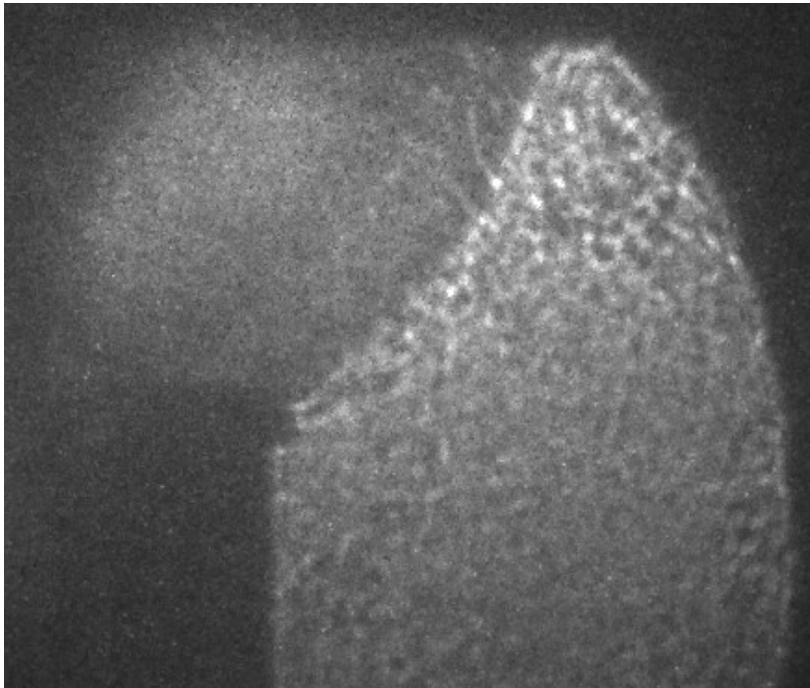
Figure 60.   Frame 9 from above, x/h 2 – 4.5

I.   TEST CONDITION 5: DOUBLE STEP AREA RATIO 2.00 WITH NATURAL EMISSION

The following two images were taken with high-speed camera looking directly at the optical section without laser illumination. A reinitiation event can be observed moving azimuthally across what was once a decoupled reaction zone. In Figure 62, the front is still planar at a distance of 5.5 x/h.
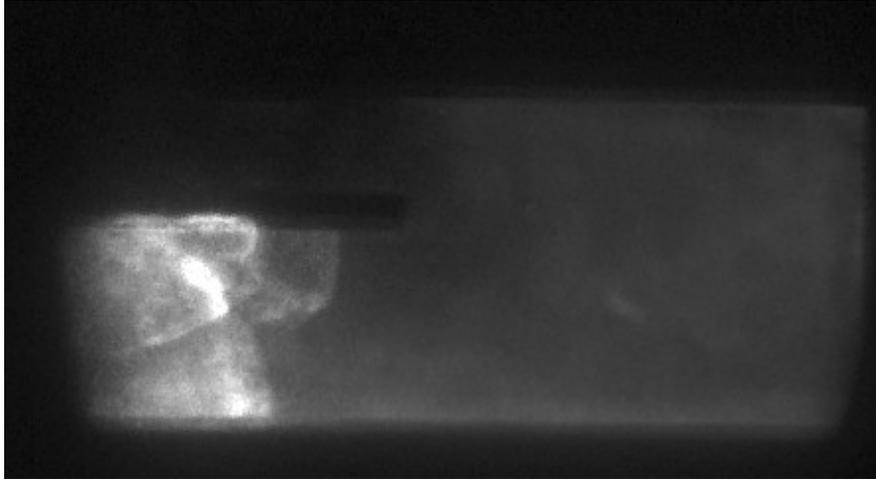

Figure 61.   Natural emission, Φ=1, 2.00 A_2/A_1, x/h 1 – 6
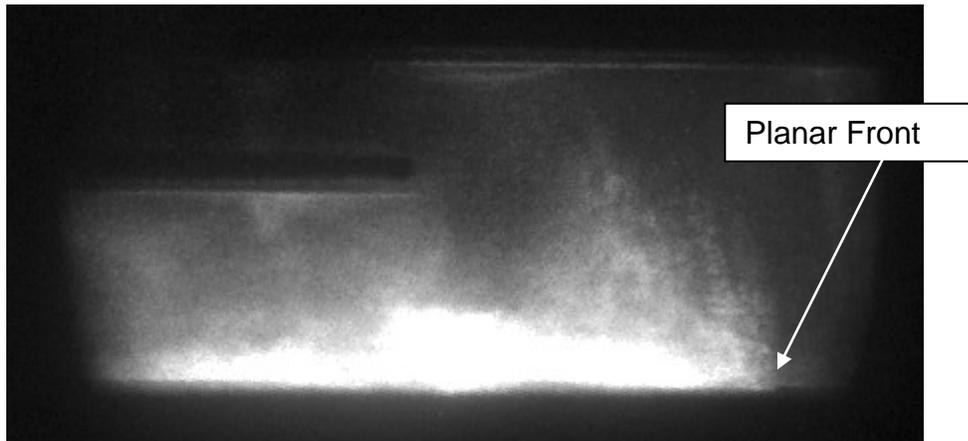
Figure 62.   Natural emission, Φ=1, 2.00 A_2/A_1, x/h 1 – 6

J. TEST CONDITION 6: DOUBLE STEP AREA RATIO 2.3 WITH SHADOWGRAPH
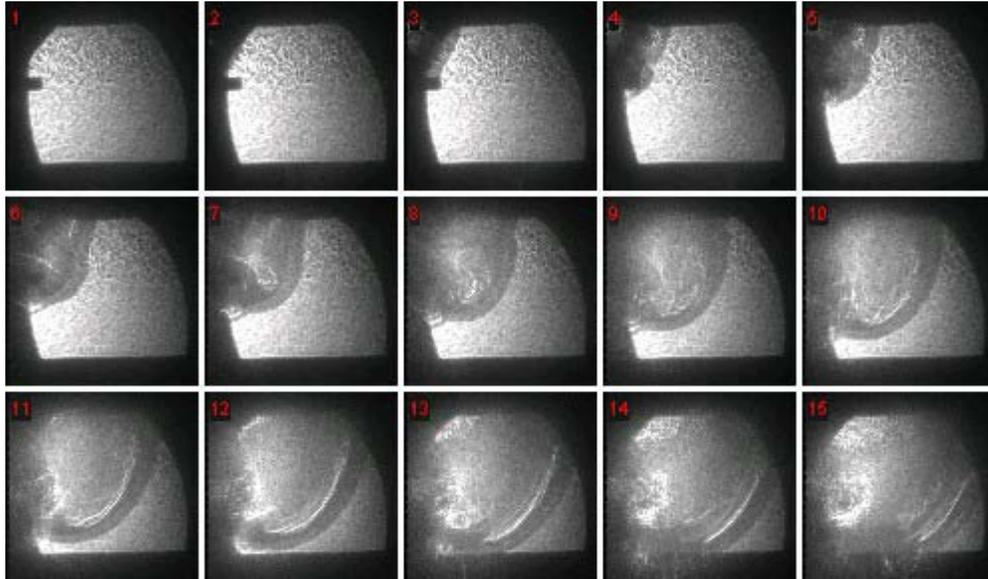

Figure 63.   Two step, Φ=1, 2 A_2/A_1
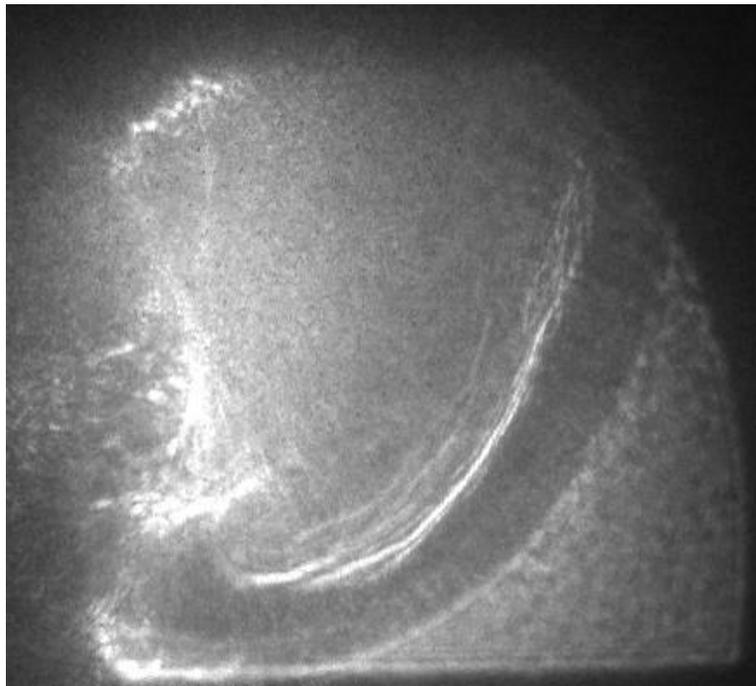
Figure 64.   Frame 12 from above

THIS PAGE INTENTIONALLY LEFT BLANK

VII. FUTURE WORK

Future work could encompass both computational and experimental aspects. Computationally, the next step would be to rerun these results with a more refined structured mesh and to develop a better chemistry set for detonations.

Experimentally, longer step sections could be manufactured to ensure proper full transition during diffractions events. Also, different fuels could be used to test the predictions model as well as a performance comparison to hydrogen. Additional PIV work is required once Lavision rebuilds the lab's existing camera. With the new optical section more diffraction experiments could be conducted using CH* and PLIF.

THIS PAGE INTENTIONALLY LEFT BLANK

VIII. CONCLUSIONS

A new optically-accessible test section was designed and built to image the detonation diffraction of hydrogen and air mixtures across multi-step configurations. Shadowgraph and PIV imaging techniques were used to determine shockwave profiles, velocities, and re-ignition mechanisms throughout the diffraction process. Computational models were investigated but failed to produce any useful information due to the artificial high reactivity of the mixtures for the various reduced chemistry kinetics and also inadequate mesh resolution utilized.

Experiments revealed that hydrogen/air detonations could survive single and double diffraction across an area ratio of 2.0 for an equivalence ratio range of 0.8 to 1.14. Successful detonation diffraction was observed for area ratios of 2.3 but only for the primary diffraction event and only for equivalence ratios near stoichiometric for the given step length. Increasing the step length would improve the likelihood of subsequent diffraction events by allowing the detonation to reform before encountering another diffraction condition. No successful detonation diffraction reinitiations were observed for area ratios of 2.6.

THIS PAGE INTENTIONALLY LEFT BLANK

APPENDIX A. NASA CHEMICAL EQUILIBRIUM OUTPUT

```
            NASA-GLENN CHEMICAL EQUILIBRIUM PROGRAM CEA2, FEBRUARY 5, 2004
                   BY  BONNIE MCBRIDE AND SANFORD GORDON
            REFS: NASA RP-1311, PART I, 1994 AND NASA RP-1311, PART II, 1996


 *******************************************************************************
 ********

 output massf
 prob case=00002142 det
 phi=1

 p(atm)=1
 output short
 output trace=1e-10

 reac
 oxid  Air  t,k= 298 wt%=  100.
 fuel  H2   t,k= 298 wt%=  100.
 end

                    DETONATION PROPERTIES OF AN IDEAL REACTING GAS
  CASE = 00002142

              REACTANT                        WT FRACTION        ENERGY
 TEMP
                                            (SEE  NOTE)         KJ/KG-MOL
 K
  OXIDANT      Air                            1.0000000         -129.895
 298.000
  FUEL         H2                             1.0000000           -4.325
 298.000

  O/F=   34.29623  %FUEL=  2.833164  R,EQ.RATIO= 1.000000  PHI,EQ.RATIO=
 1.000000

 UNBURNED GAS

 P1, BAR         1.0132
 T1, K           298.00
 H1, KJ/KG        -4.36
 M1, (1/n)       21.008
 GAMMA1          1.4015
 SON VEL1,M/SEC   406.6

 BURNED GAS
```

```
T, K                2943.63
RHO, KG/CU M        1.5500 0
H, KJ/KG             1333.33
U, KJ/KG              313.90
G, KJ/KG            -29833.7
S, KJ/(KG)(K)        10.5880

M, (1/n)              24.008
(dLV/dLP)t          -1.00954
(dLV/dLT)p            1.2062
Cp, KJ/(KG)(K)        3.3542
GAMMAs               1.1637
SON VEL,M/SEC        1089.2

DETONATION PARAMETERS

P/P1                 15.595
T/T1                  9.878
M/M1                 1.1428
RHO/RHO1             1.8042
DET MACH NUMBER      4.8335
DET VEL,M/SEC        1965.1

MASS FRACTIONS

*Ar                 1.2550-2
*CO                 1.3093-4
*CO2                2.6525-4
COOH                2.6149-9
*H                  2.4760-4
HCO                 1.0225-9
HNCO                2.395-10
HNO                 3.1235-6
HNO2                8.9839-7
HNO3                1.028-10
HO2                 1.5250-5
*H2                 2.6254-3
HCOOH               3.735-10
H2O                 2.2035-1
H2O2                2.3080-6
*N                  1.1146-6
*NH                 4.5040-7
NH2                 2.7000-7
NH3                 3.4969-7
NH2OH               4.217-10
*NO                 9.4235-3
NO2                 6.6339-6
*N2                 7.2938-1
N2O                 2.7711-6
*O                  1.3571-3
*OH                 1.3522-2
*O2                 1.0117-2
O3                  6.2078-9
```

84

APPENDIX B.   CAD DRAWINGS

The following set of Figures were all generated with the Solidworks 2010 mechanical modeling software package. Optical section and the new head end inlet flange were made from Type 303 Stainless Steel in order to meet the rigidity and strength requirements for the engine test section while also being the most readily mechineable? for an austenitic stainless steel. All internal components were made from 6061 Al. All units are in inches and degrees. Tolerances for linear dimensions are ±0.01" and radial dimensions are ±0.05º.

Detonation Channel

Inlet Manifold
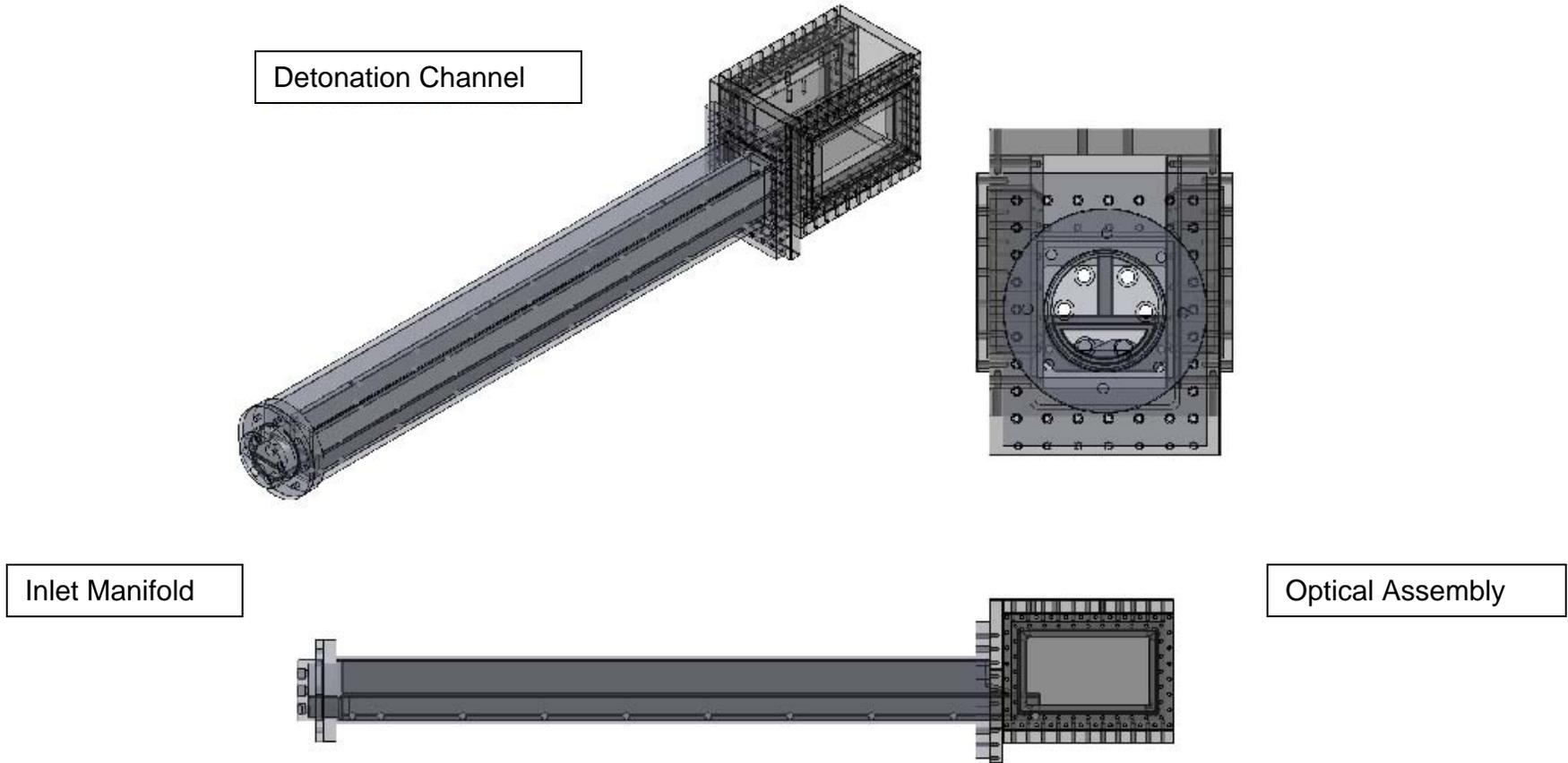
Optical Assembly

Figure 65.   Overall detonation channel assembly
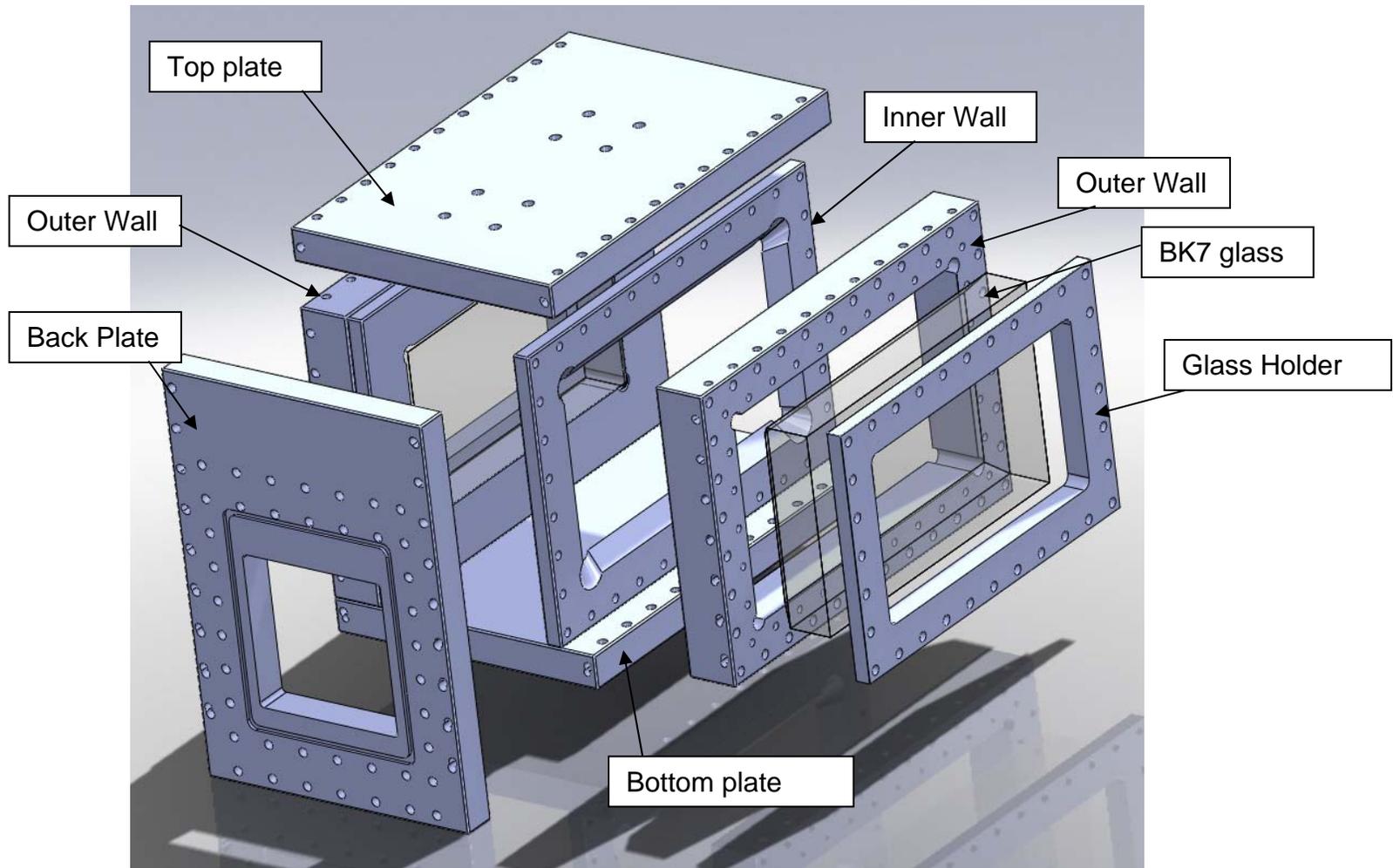
Figure 66.   Exploded view of Optical assembly
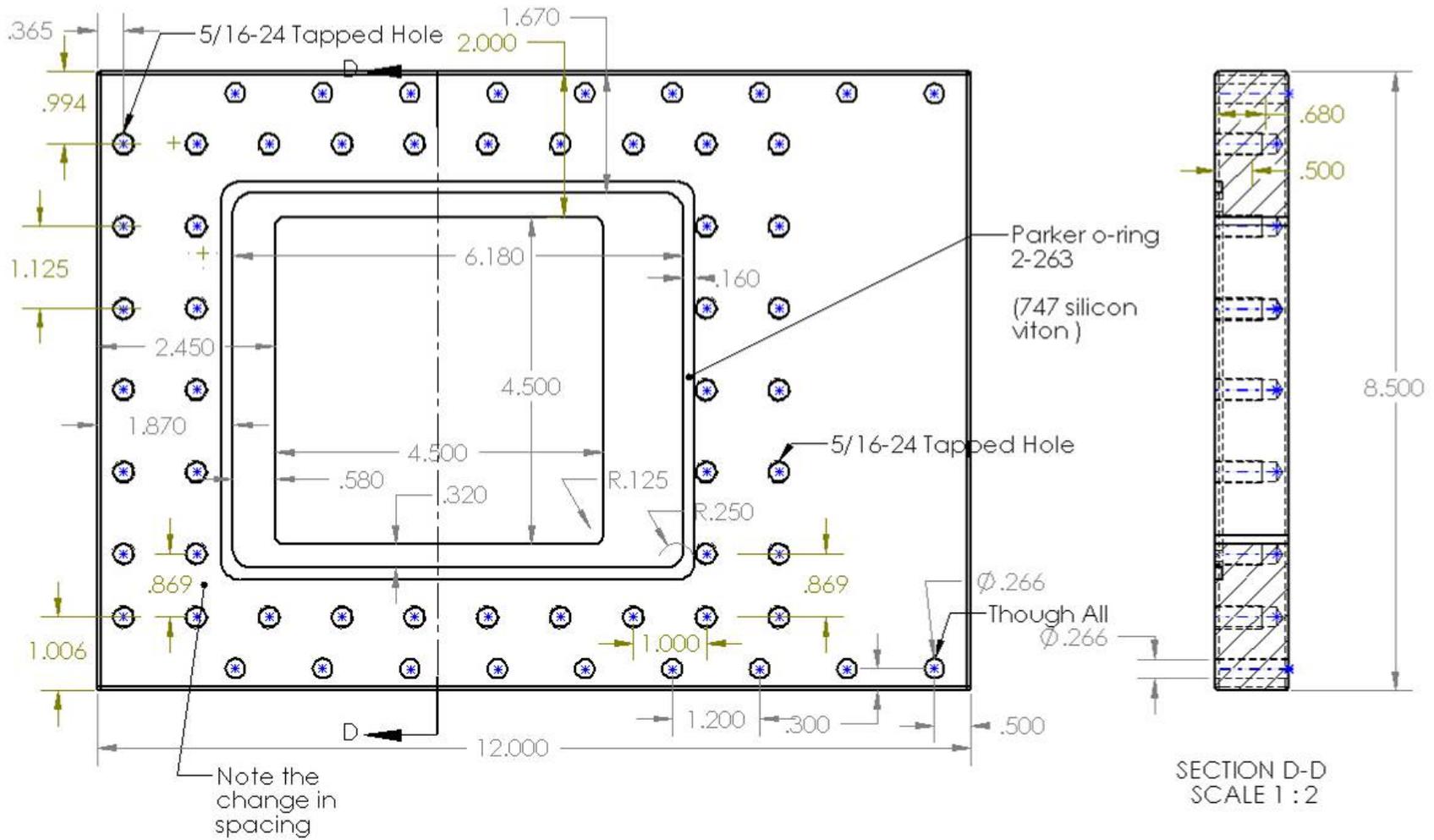
Figure 67.   Back plate (1 of 2)
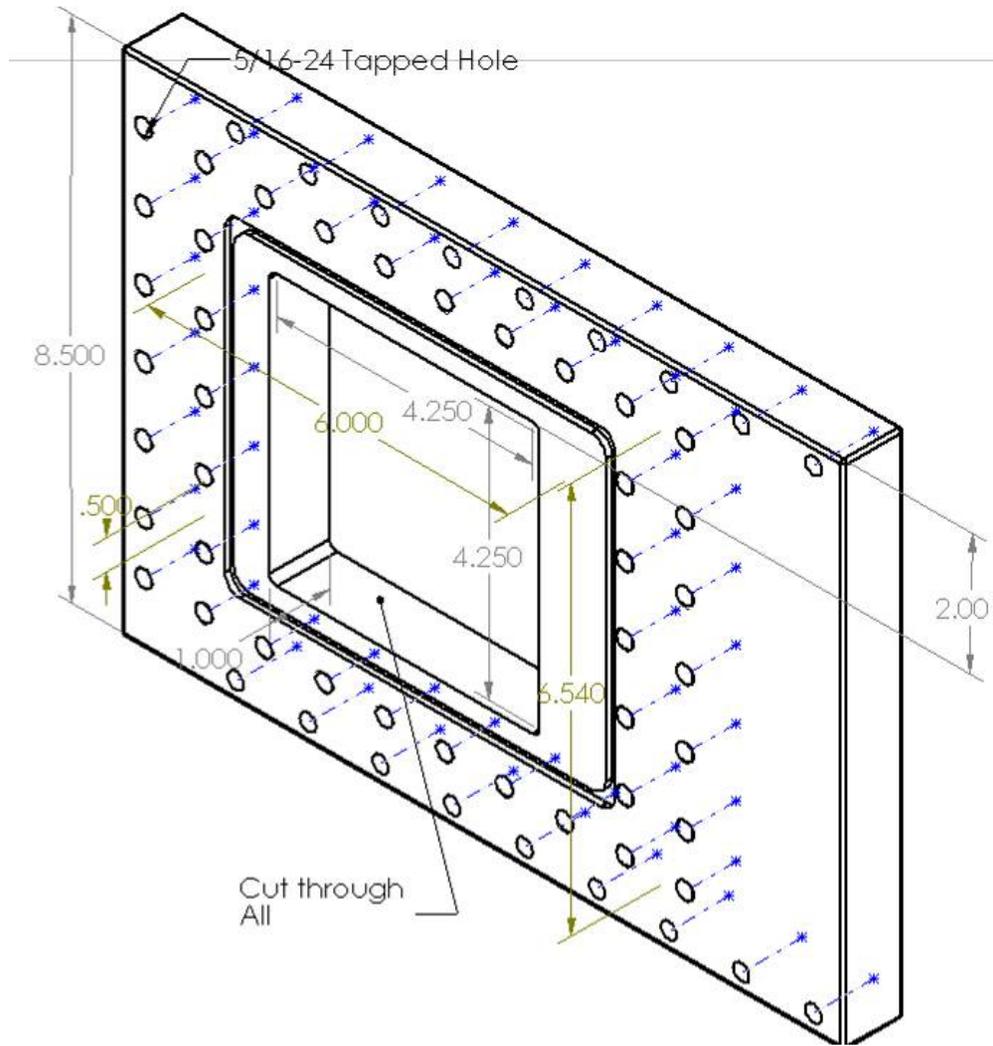
Figure 68.   Back plate (2 of 2)

22X Ø .21 ▽ .65
1/4-28 UNF ▽ .50

36X Ø .28 THRU ALL

Through all cut

1.50

32X Ø .21 ▽ .65
1/4-28 UNF ▽ .50
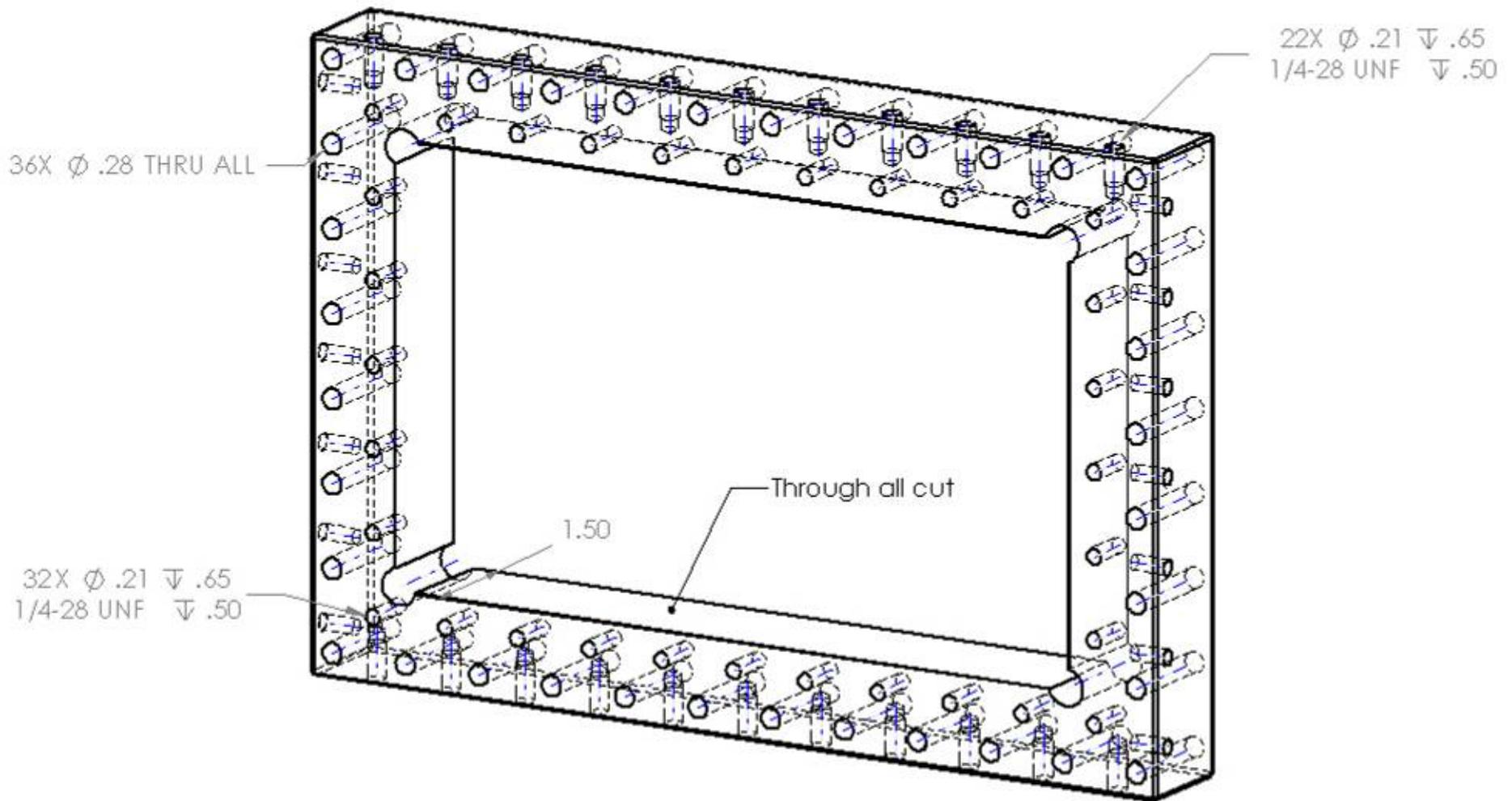
Figure 69.   Outer wall optical left and Right (1of 4)

.75

11X ∅ .21 ▽ .65
1/4-28 UNF ▽ .50

R.05

.25

.25

1.25

.30

.70

1.20

.25

1.10

∅ .25

∅ .21

7x ∅1/4-28 ▽ .50

Side view

Top view

DETAIL D
SCALE 1 : 1

.30

.65

1.50
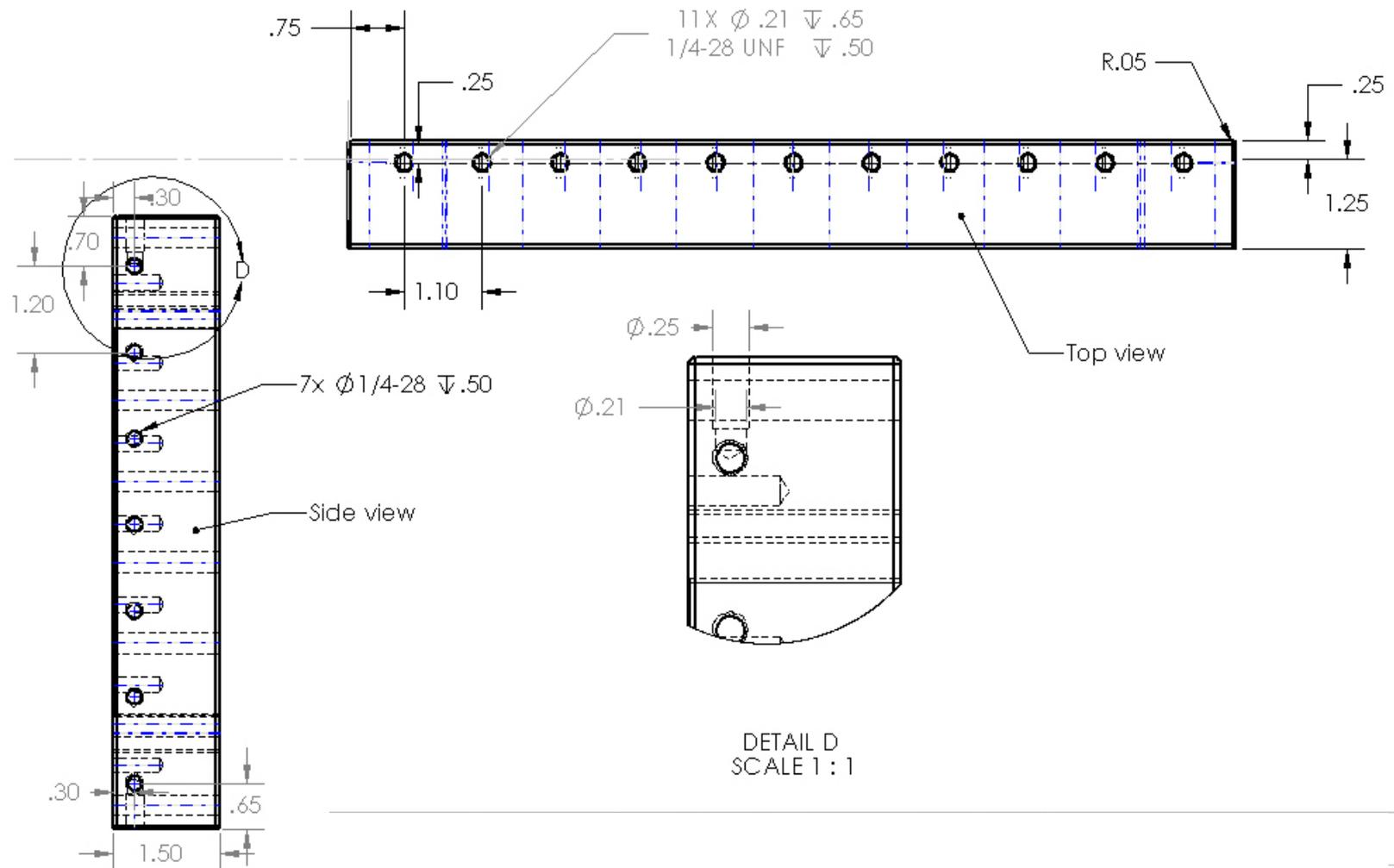
Figure 70.   Outer wall optical Left and Right (2 of 4)

91
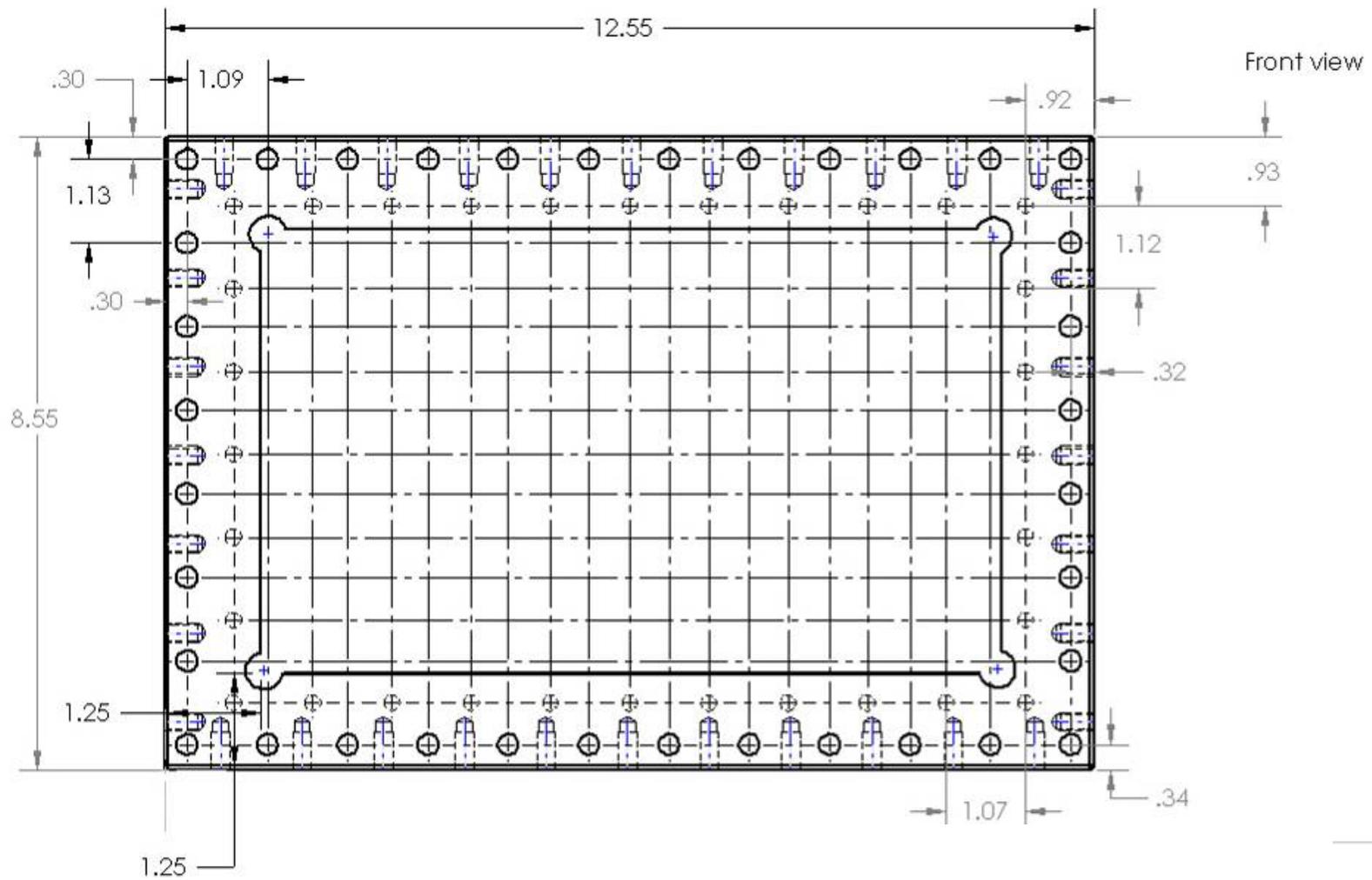
Figure 71.   Outer Wall optical Left and Right (3 of 4)
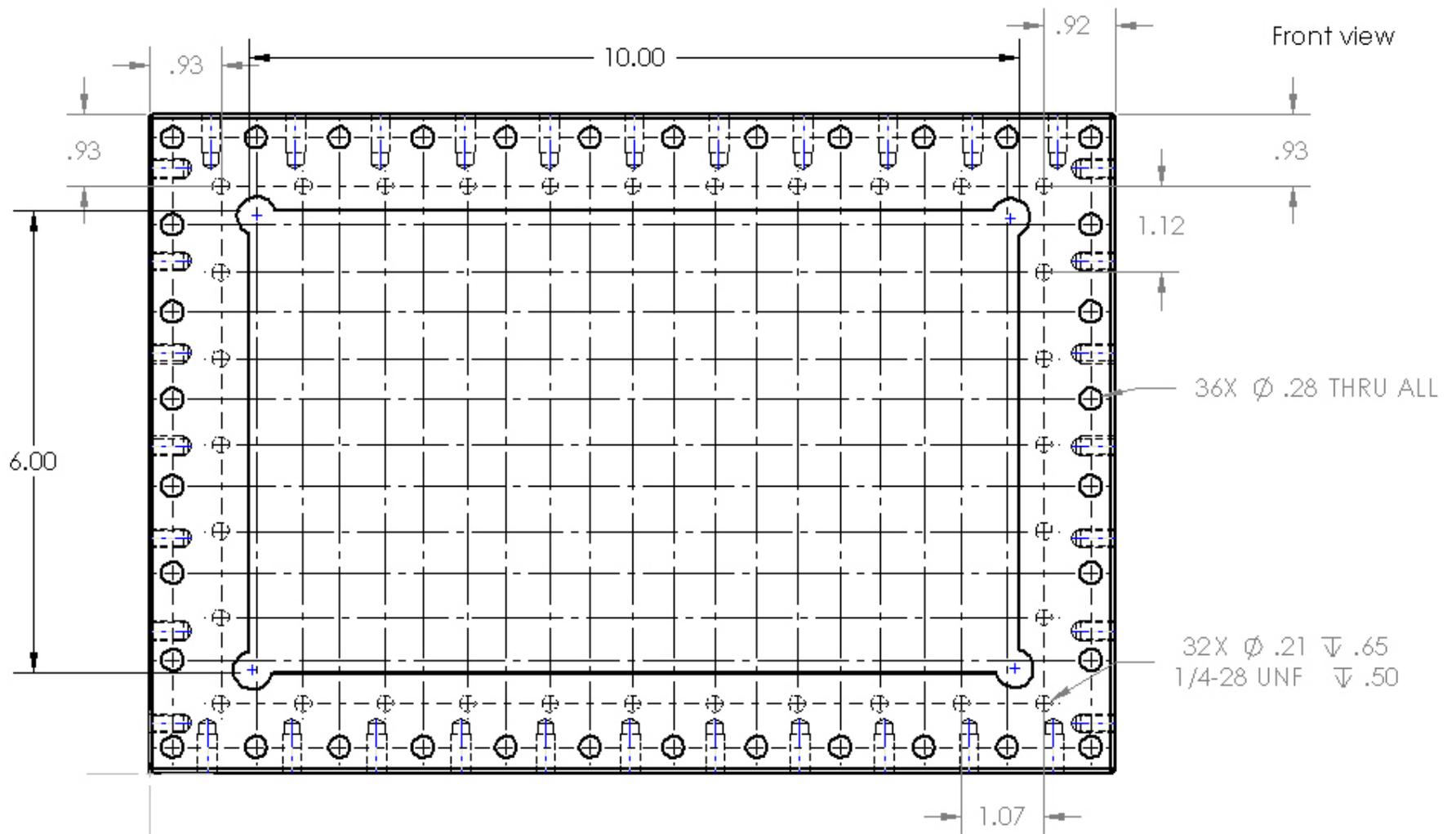
Figure 72.   Outer Wall optical Left and Right (4 of 4)
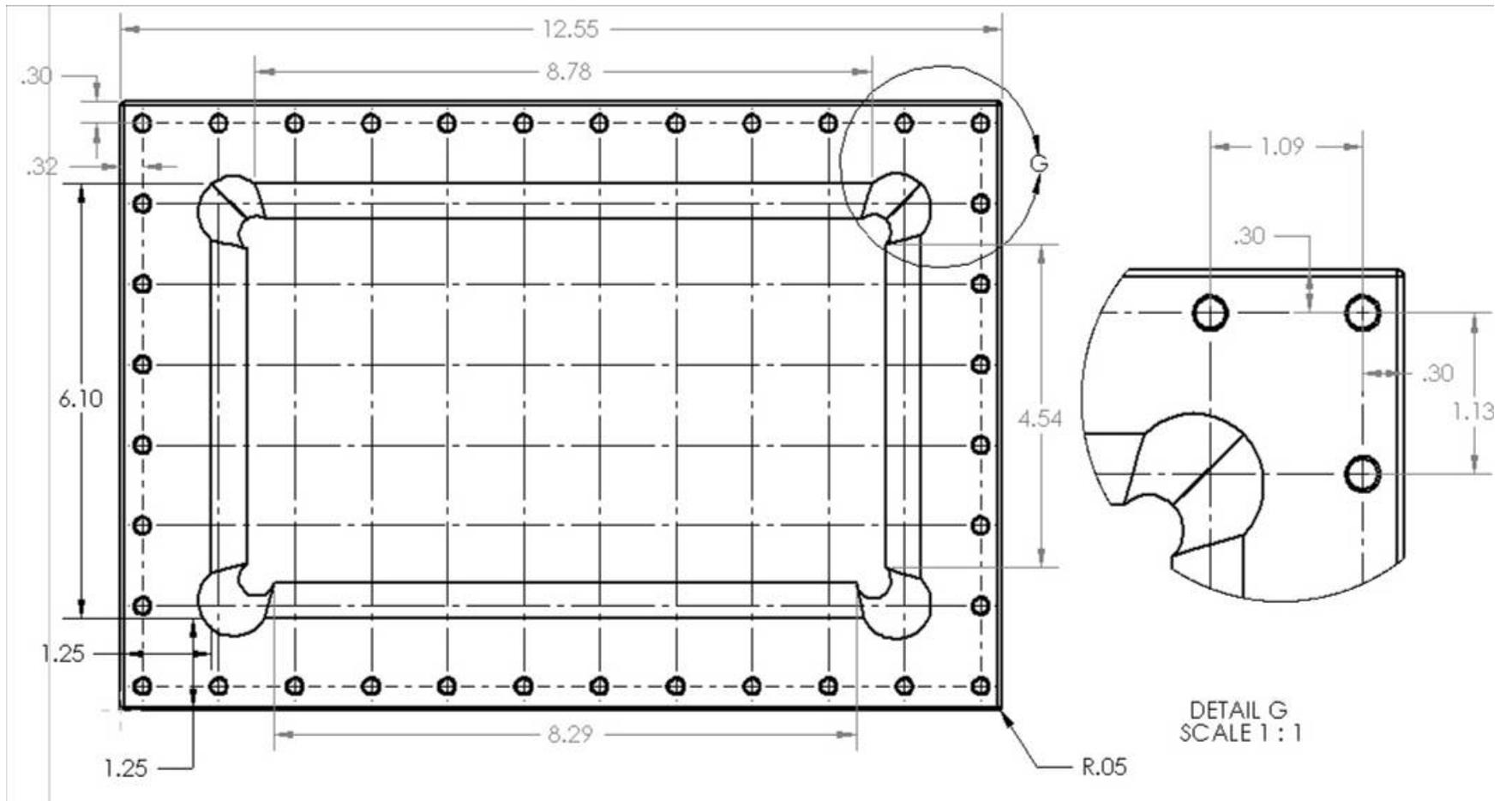
Figure 73.   Inner Wall optical (1 of 2)

94

45.00°

1.13

Cut through all with a 45
degree chamfer

8.55

36X Ø .21 ▽ .36
1/4-28 UNF ▽ .25

12.55

.50

1.09

Cut through all with a 45
degree chamfer
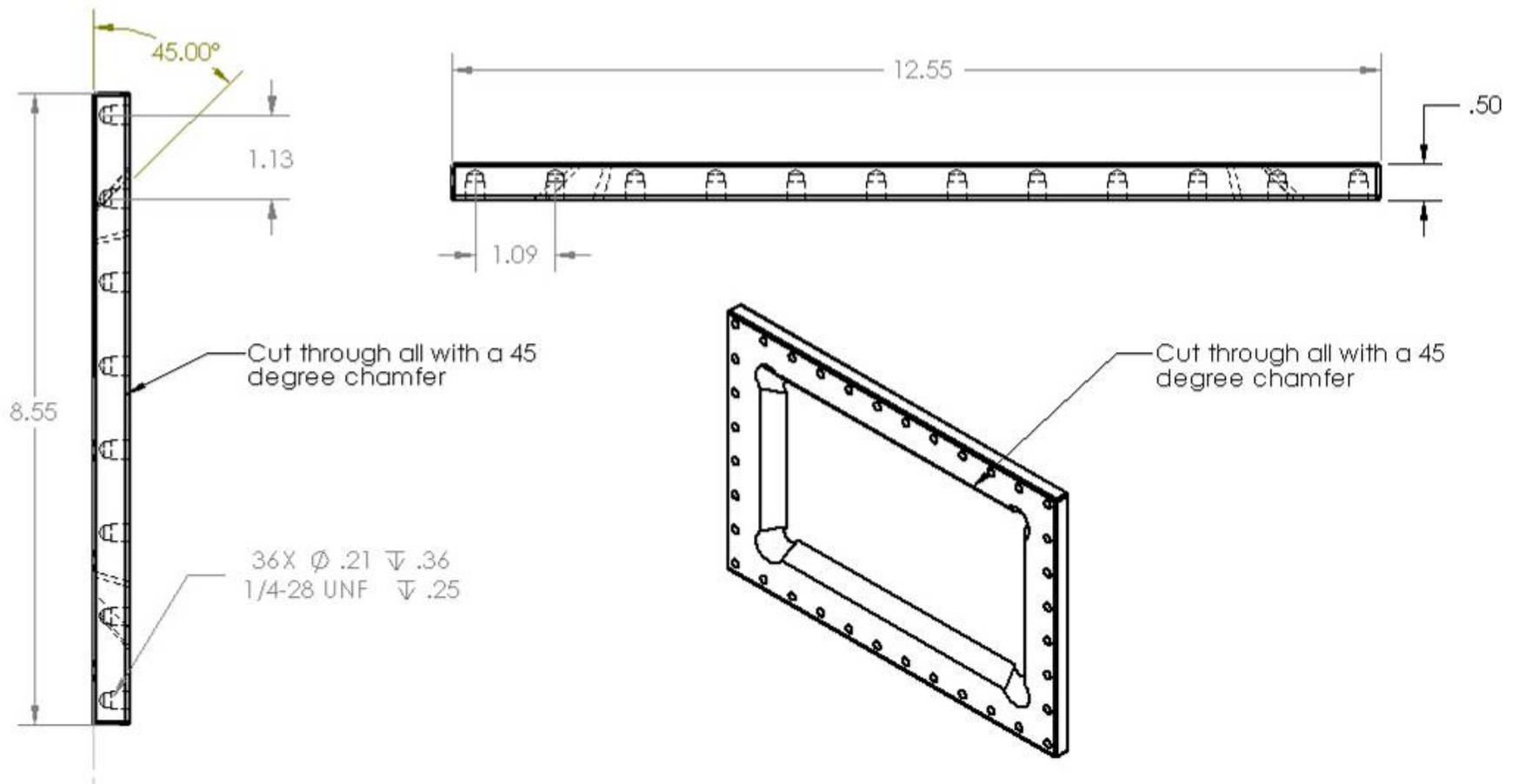
Figure 74.   Inner wall optical (2 of 2)

32X Ø .28 THRU ALL

5.02

9.02
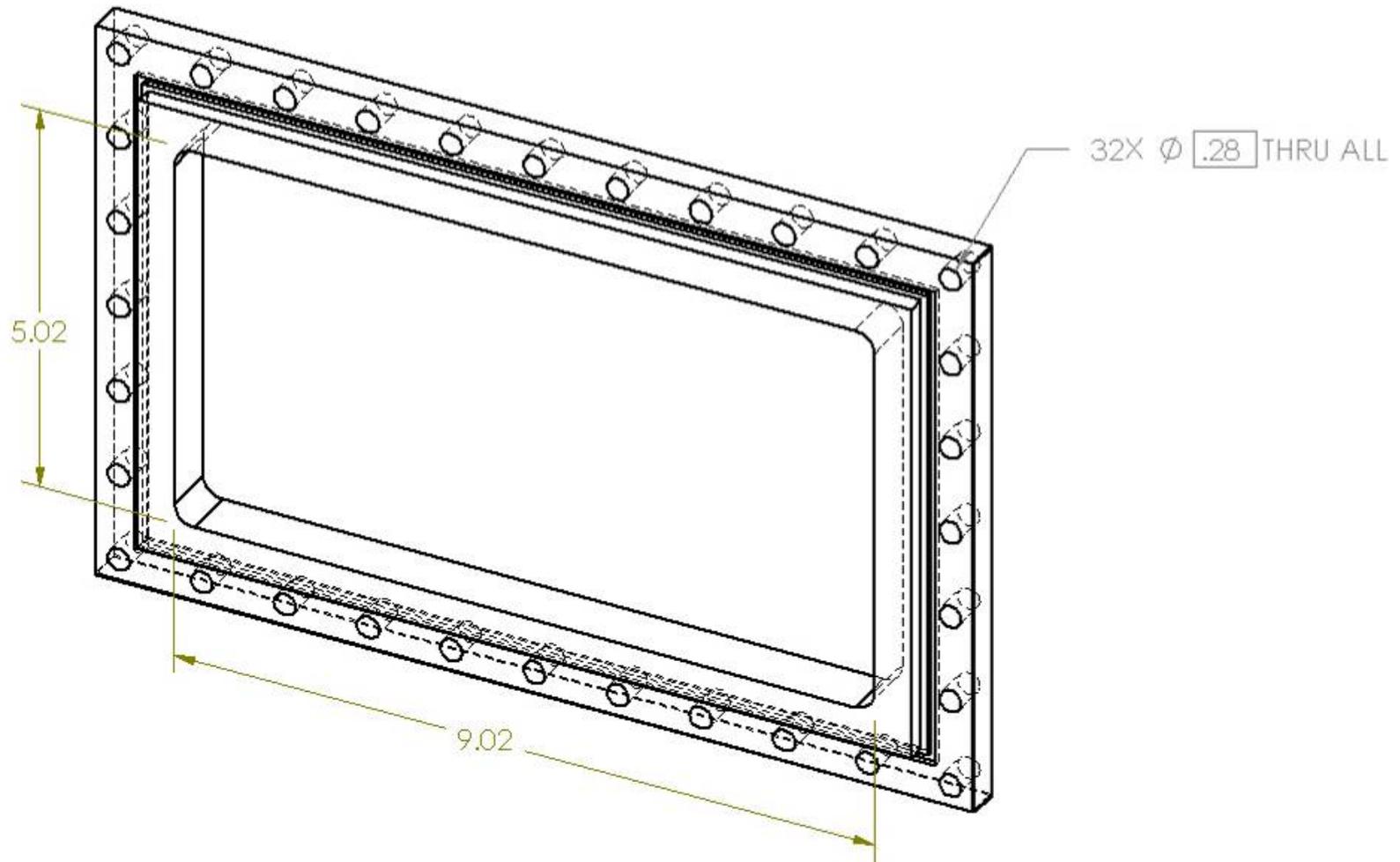
Figure 75.   Glass holder optical (1 of 2)

Figure 76. Glass Holder optical (2 of 2)
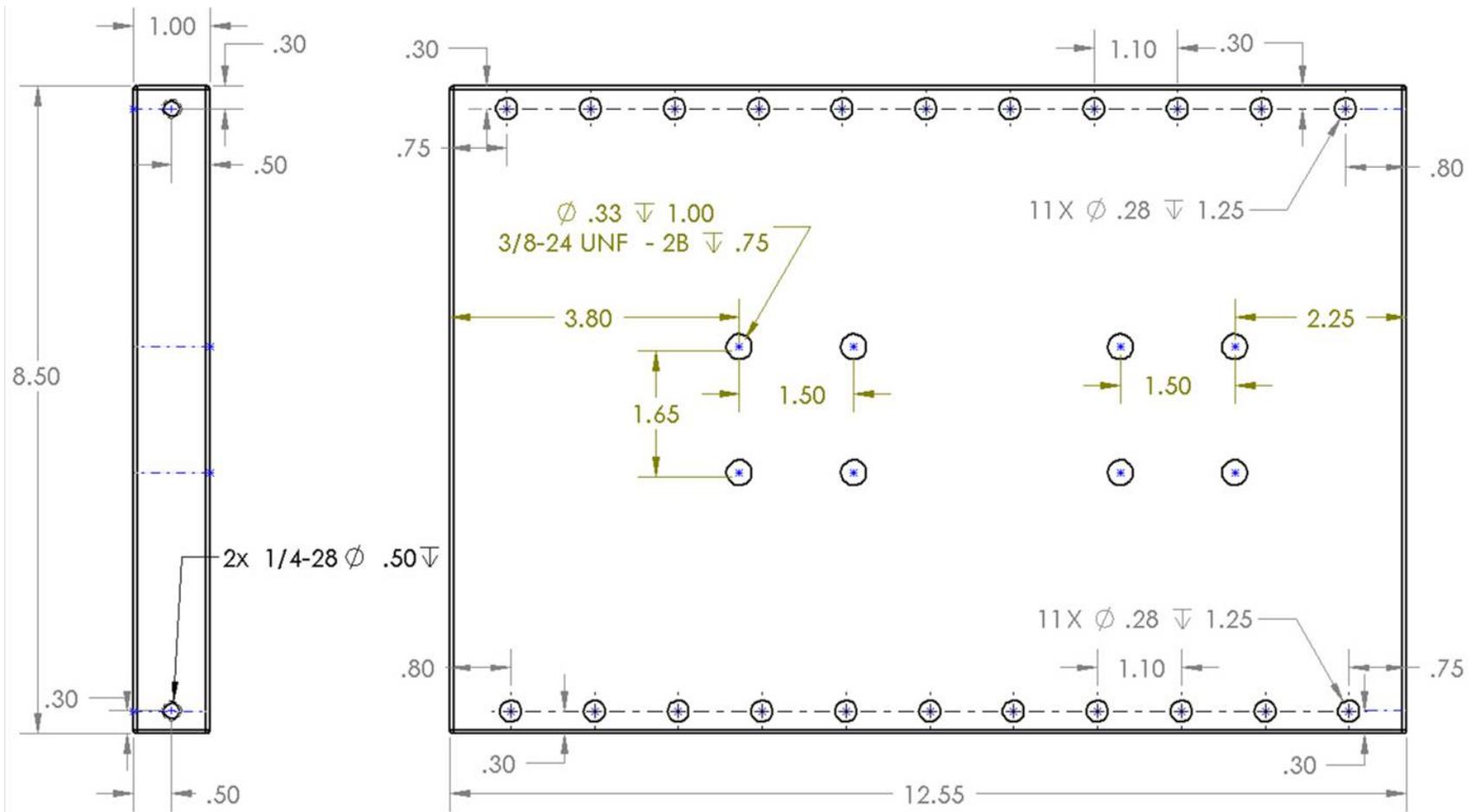
Figure 77.   Top Plate

98
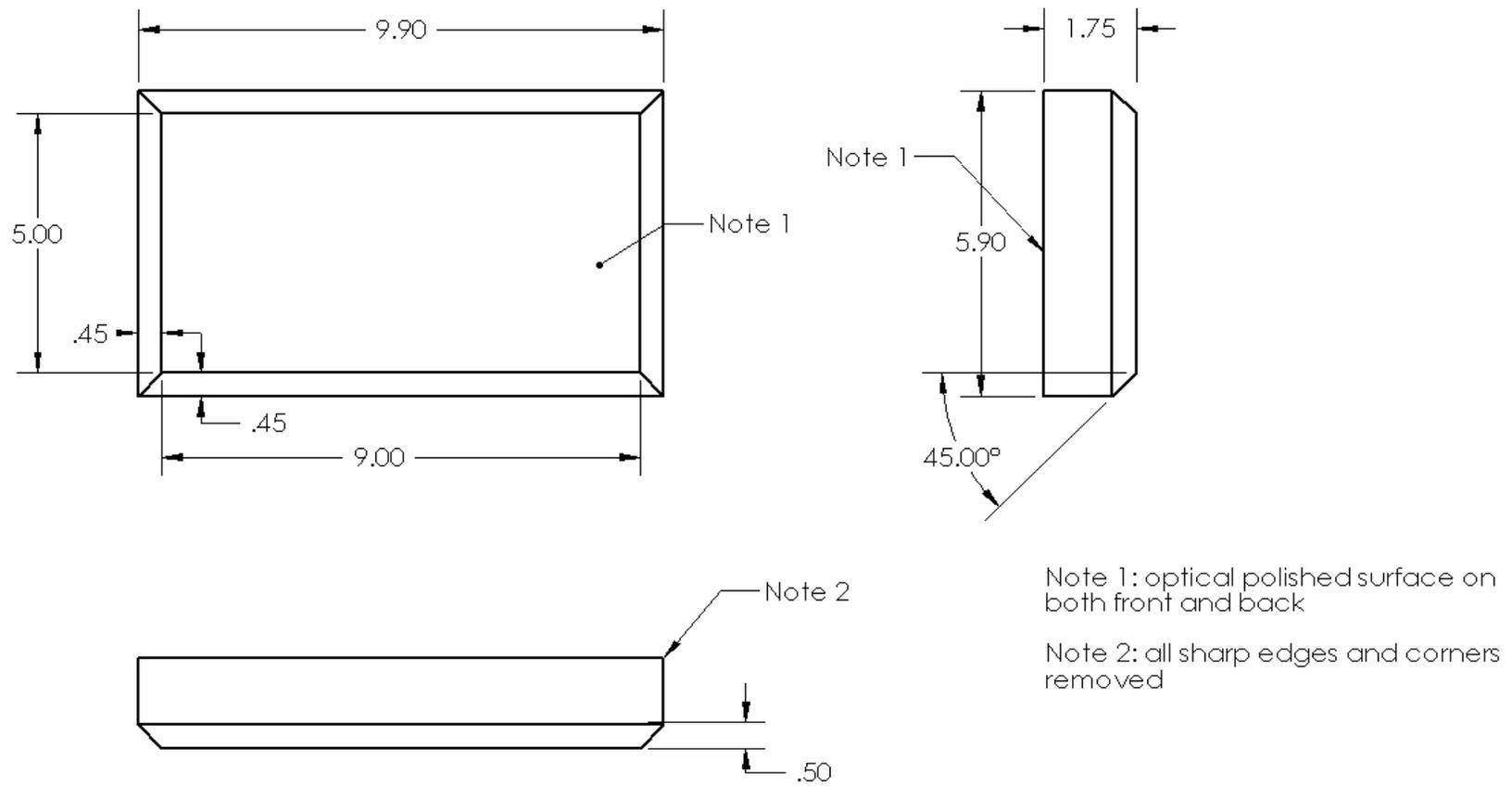
Figure 78.   BK7 glass for main optical section
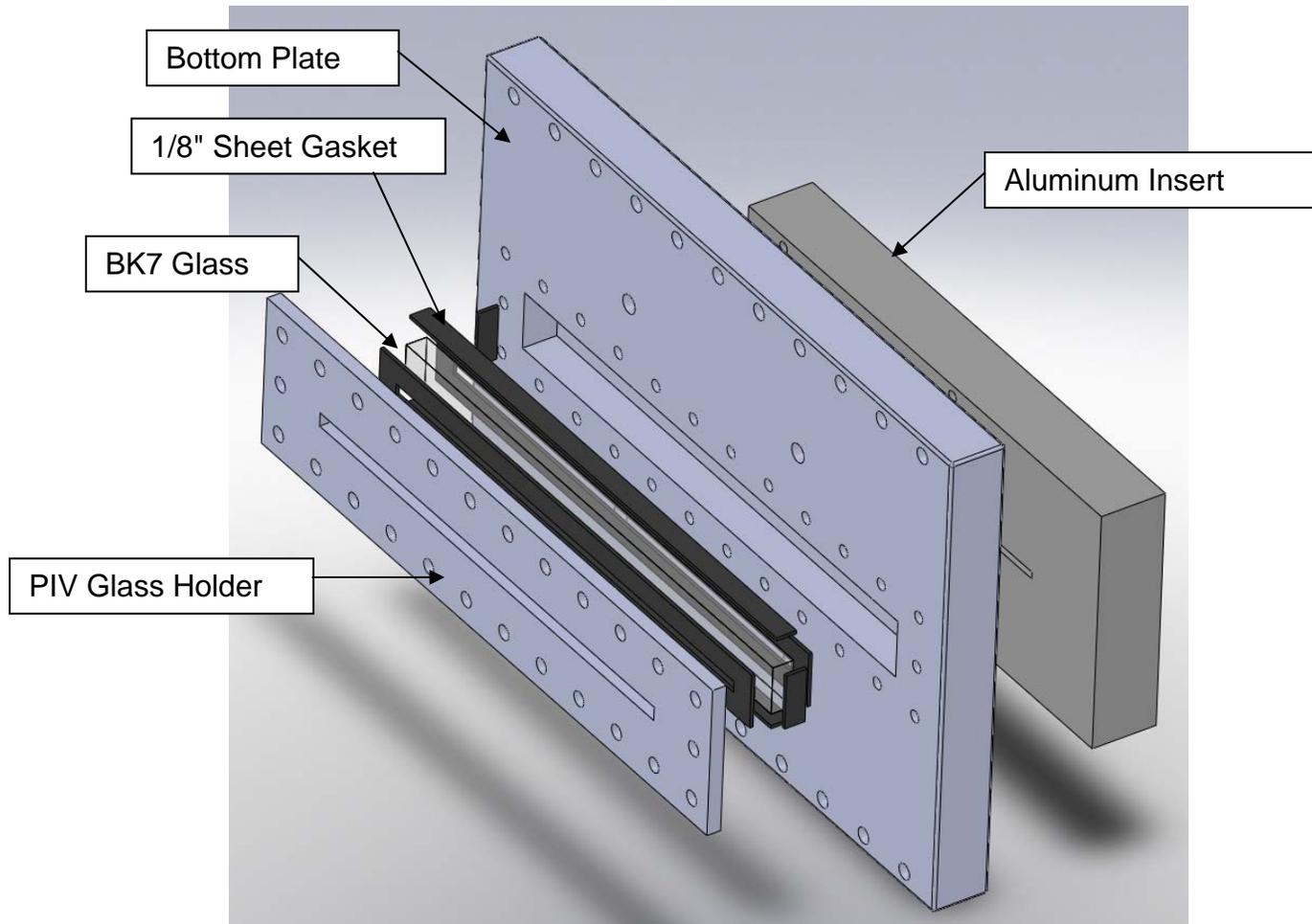
Figure 79.   Bottom plate assembly for PIV laser sheet
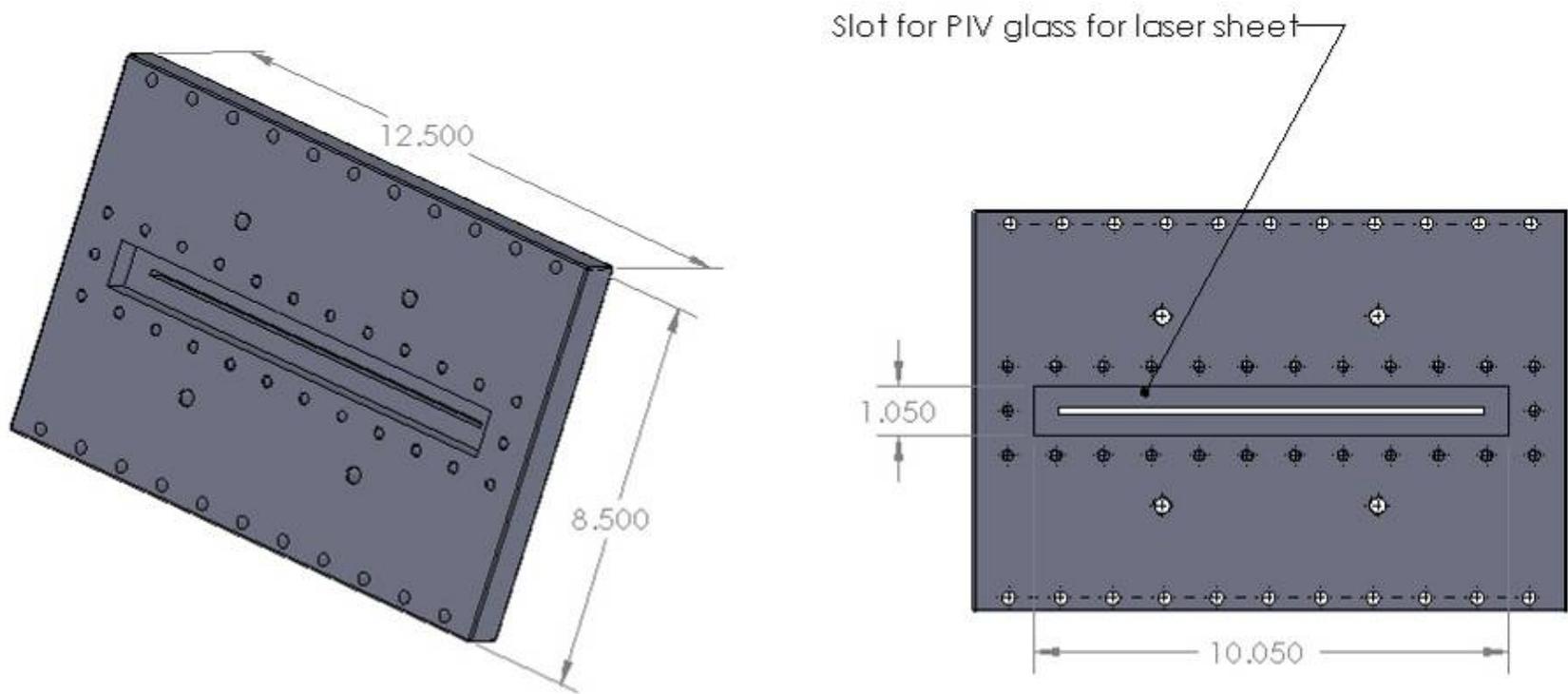
Figure 80.   Bottom plate with BK7 glass slot PIV laser sheet (1 of 2)
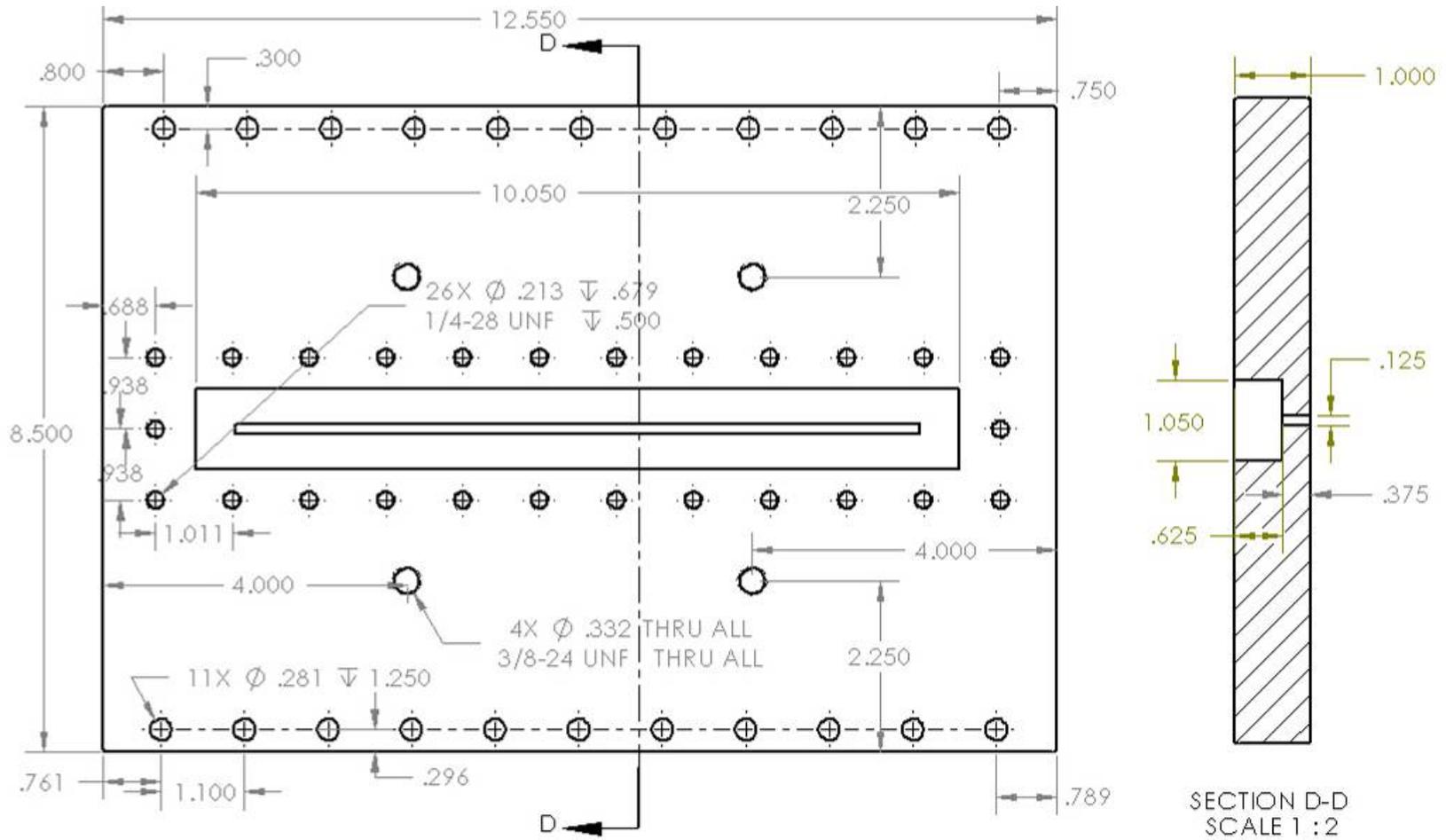
Figure 81.   Bottom Plate (2 of 2)
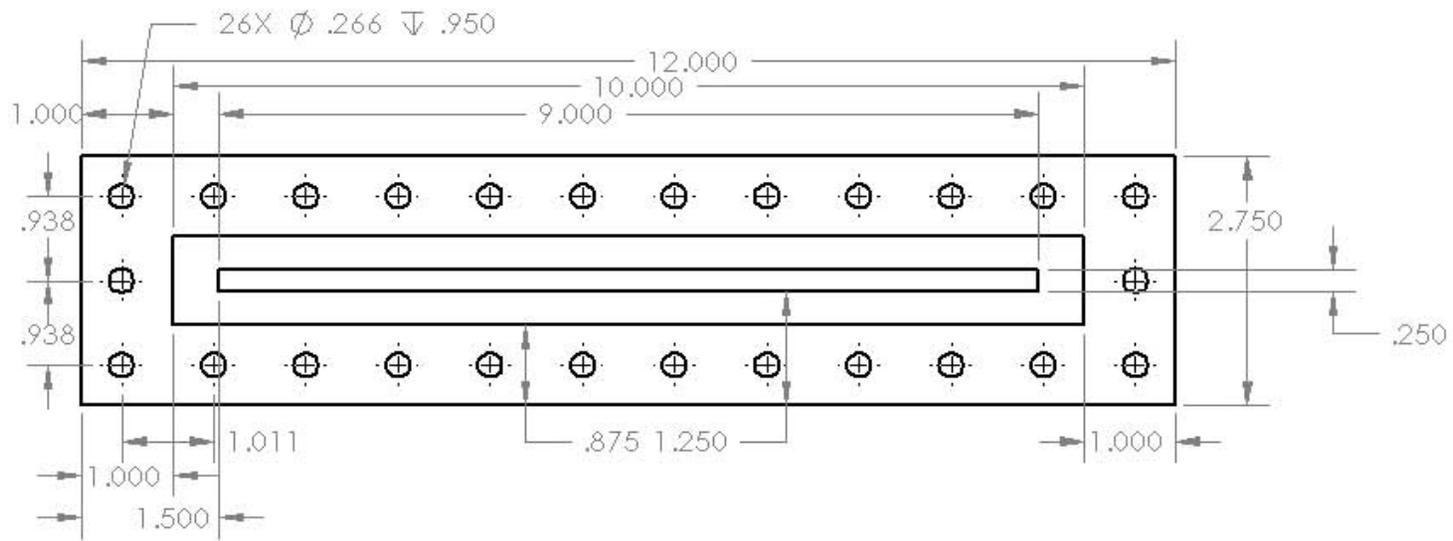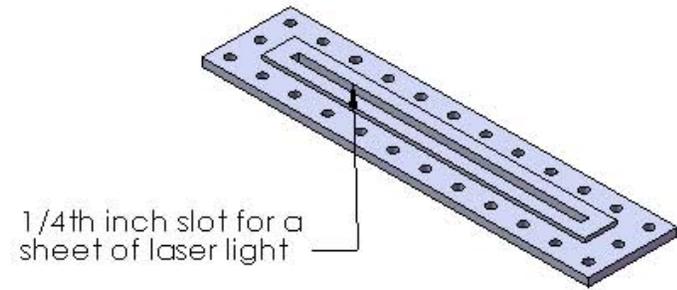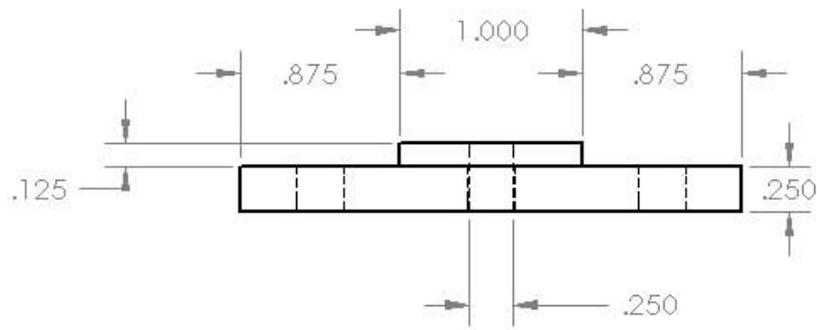
Figure 82.   PIV Glass Holder

103
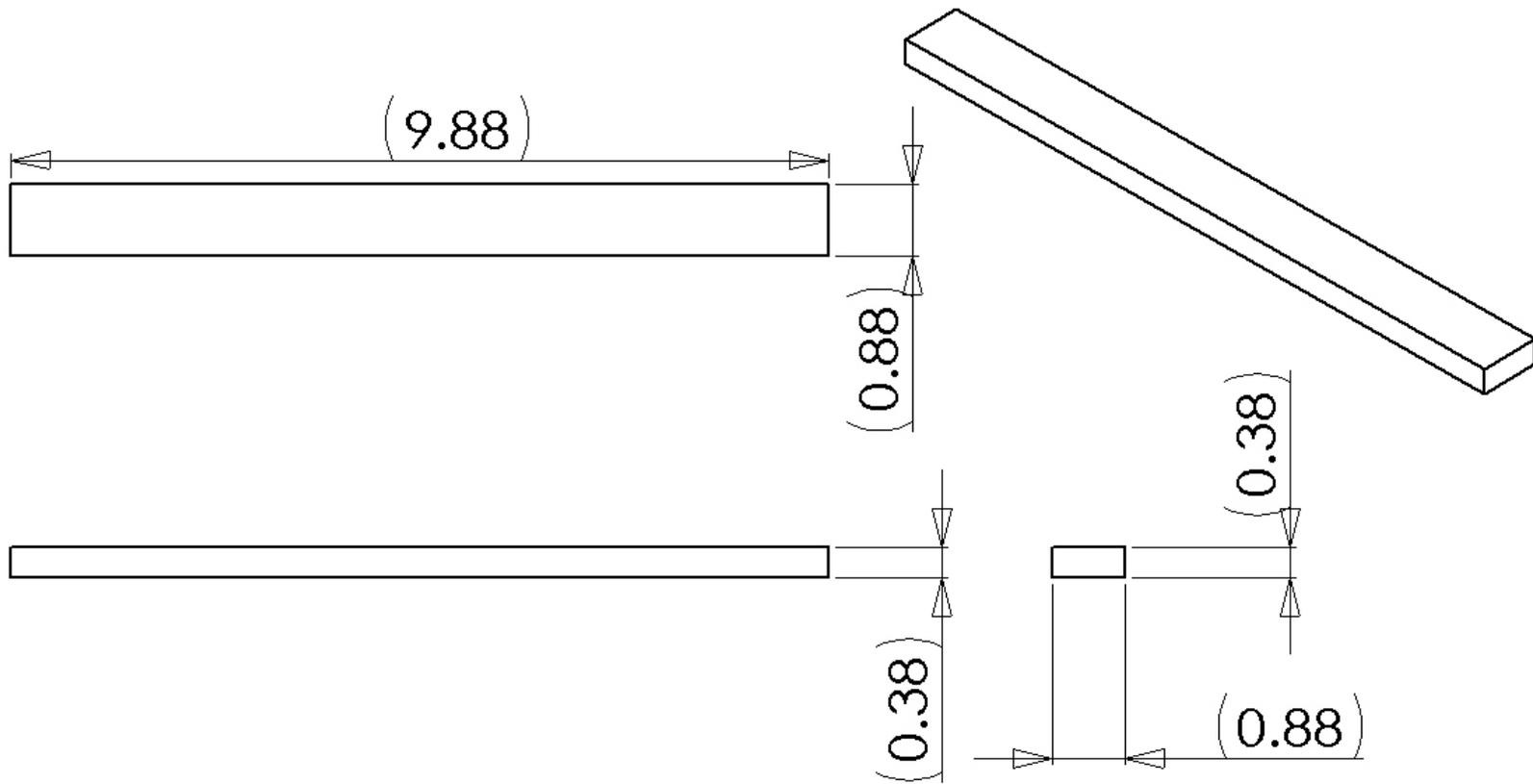
Figure 83.   PIV BK7 Glass
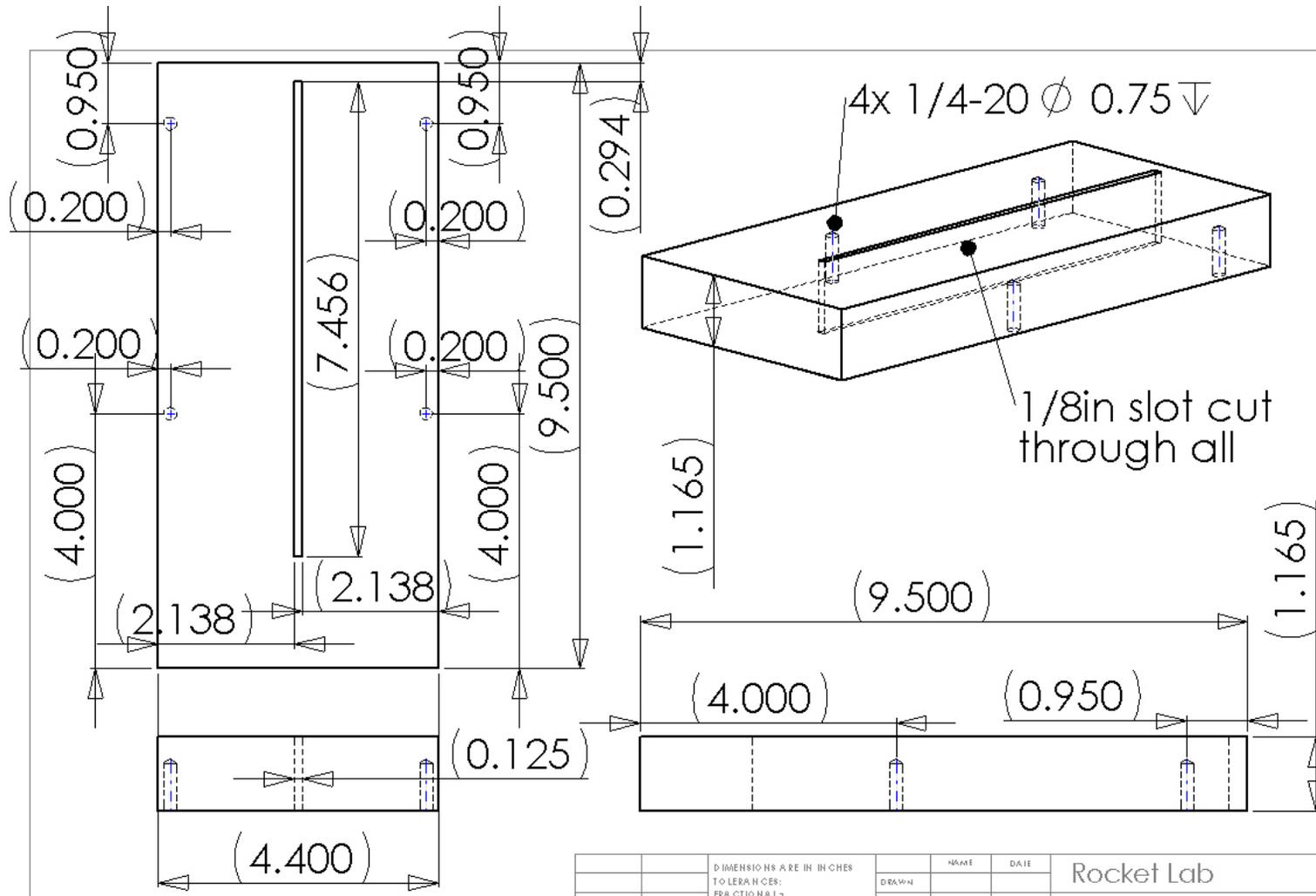
Figure 84.   Aluminum Insert

105
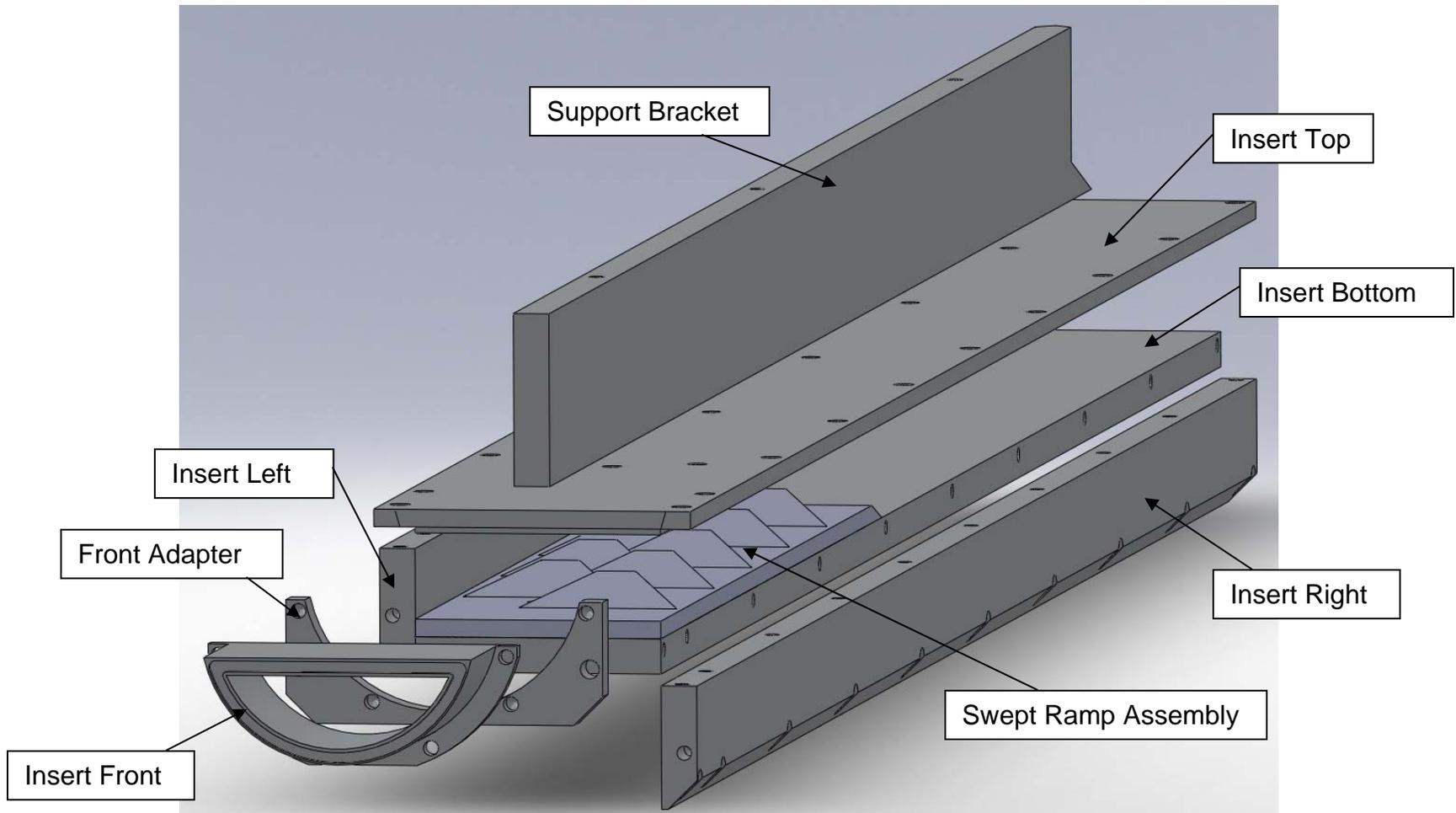
Figure 85.   Split flow insert assembly
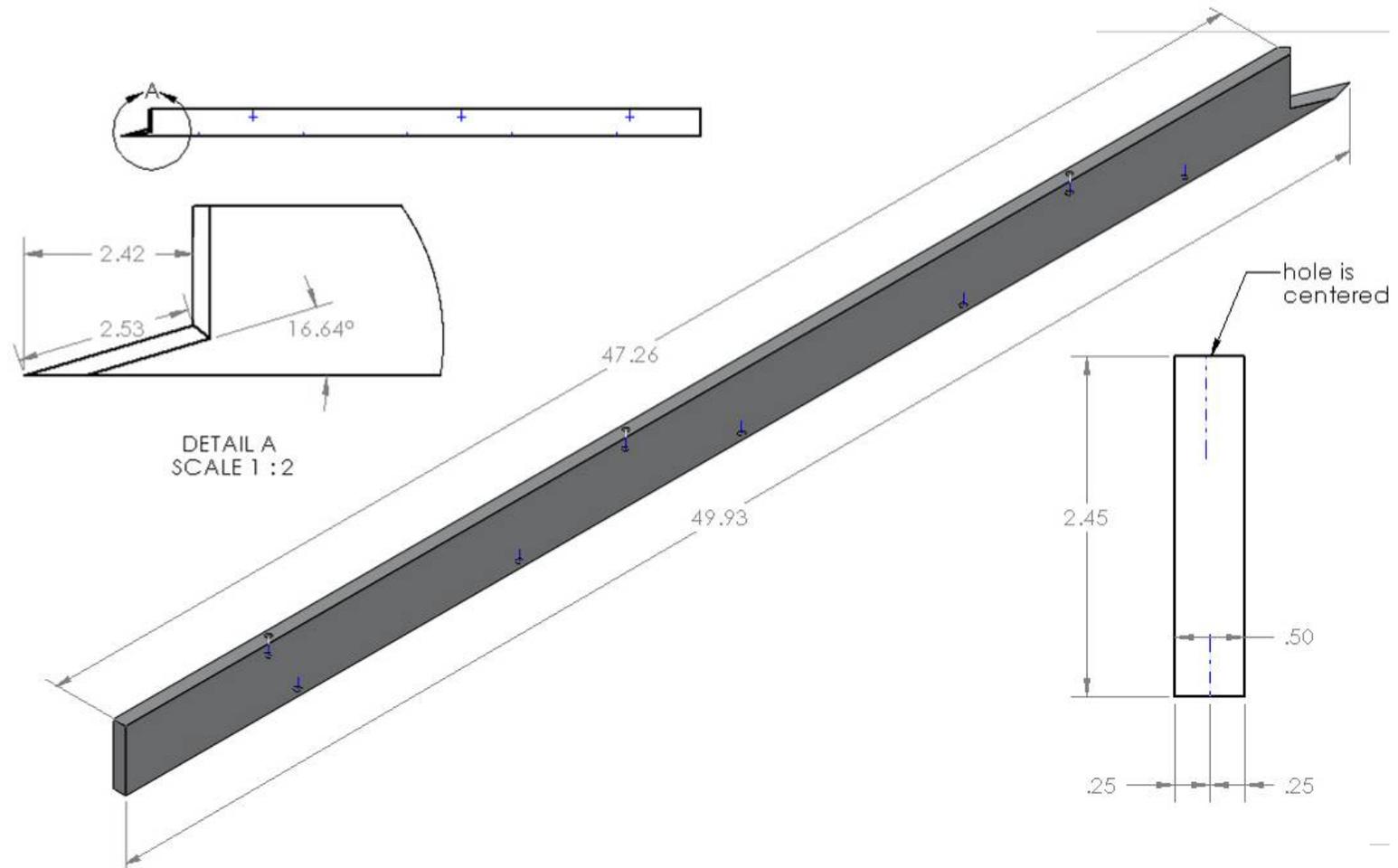
Figure 86.   Support bracket (1 of 2)

8.93   18.00   14.50

6.68   9.00   9.00   9.00   9.00

2.45

3x ∅.20 ⊽.65
1/4-20 UNC ⊽.50
centered

5X ∅ .20 ⊽ .65
1/4-20 UNC ⊽ .50

15.98°

.87

3x ∅.20 ⊽.65
1/4-20 UNC ⊽.50

Bottom
View

1.80

135.00°

Top view

DETAIL E
SCALE 1 : 4

DETAIL D
SCALE 1 : 2

DETAIL C
SCALE 1 : 2

|		UNLESS OTHERWISE SPECIFIED:		NAME	DATE	
		DIMENSIONS ARE IN INCHES TOLERANCES: FRACTIONAL ± ANGULAR: MACH ±0.05 TWO PLACE DECIMAL ±0.01	DRAWN		10 Aug 10	TITLE: split flow : support
			CHECKED			
			ENG APPR.			
			MFG APPR.			
		INTERPRET GEOMETRIC	Q.A.			

Figure 87.   Support bracket (2 of 2)
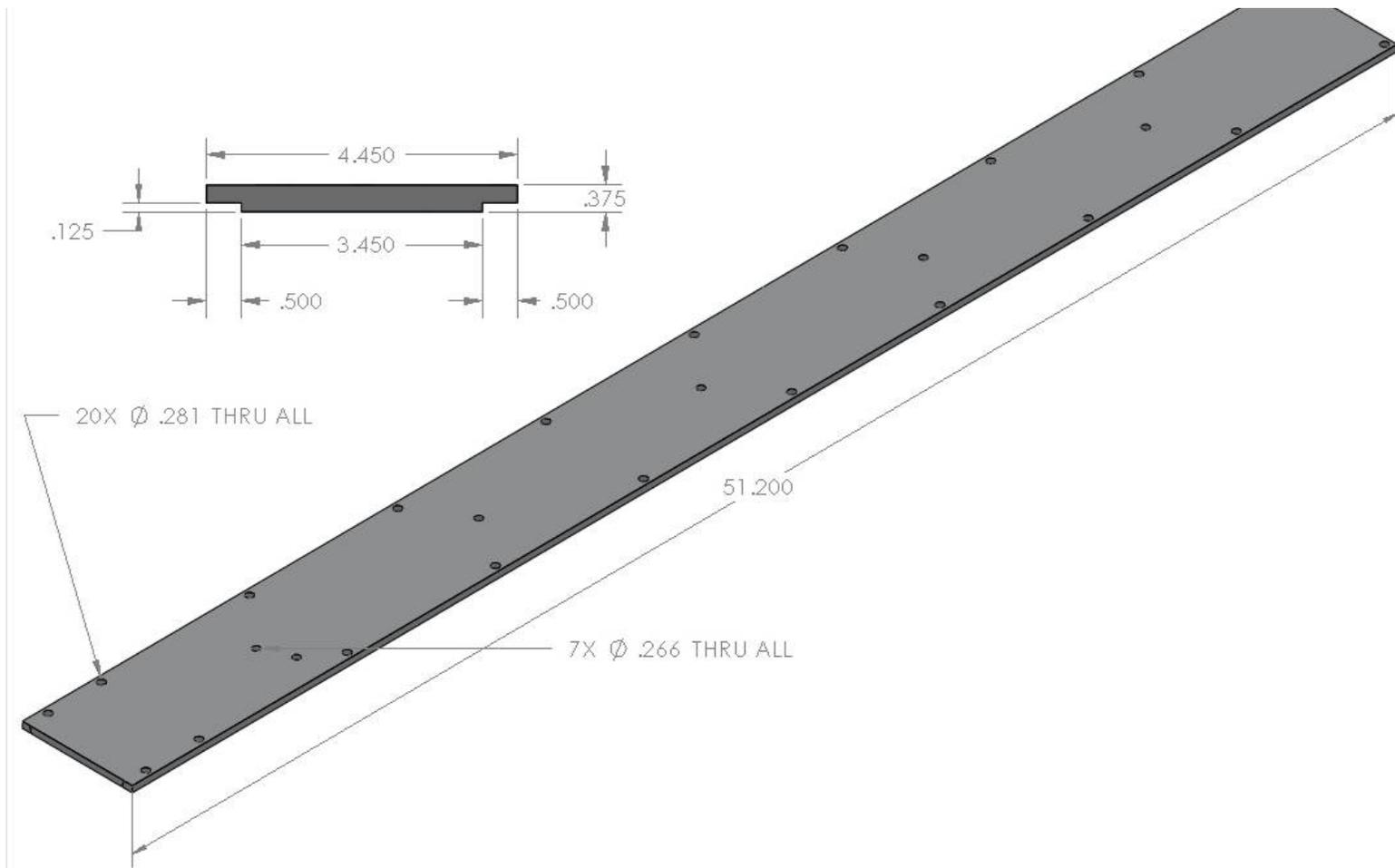
Figure 88.   Insert top (1 of 2)
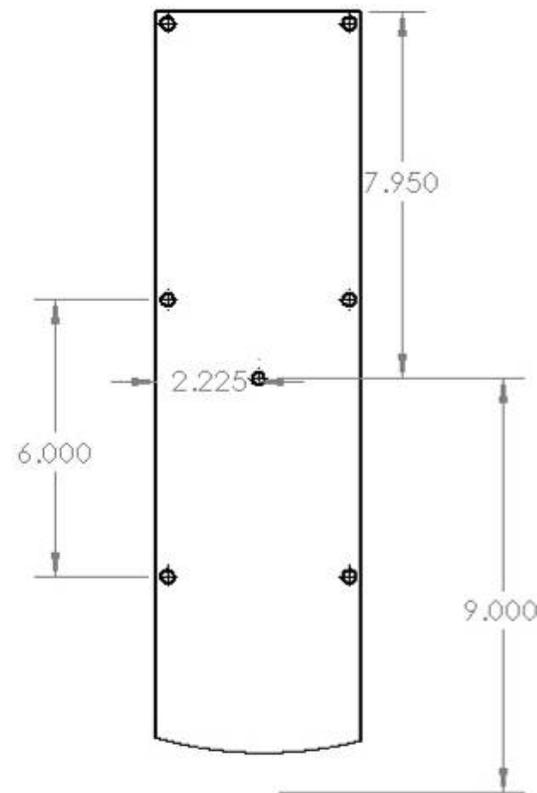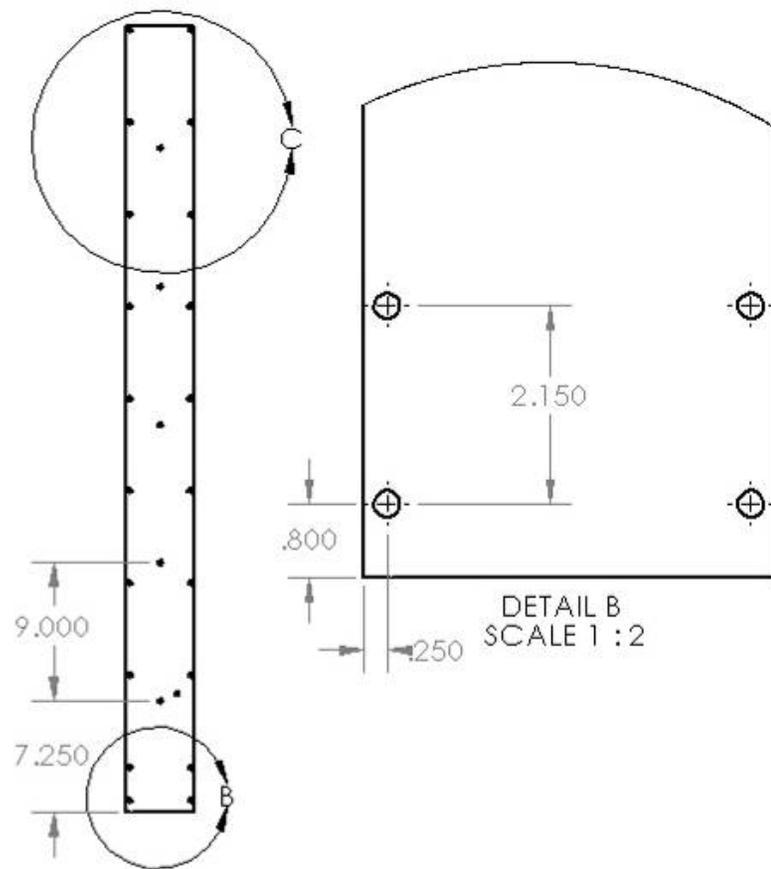
Figure 89.   Insert top (2 of 2)

110
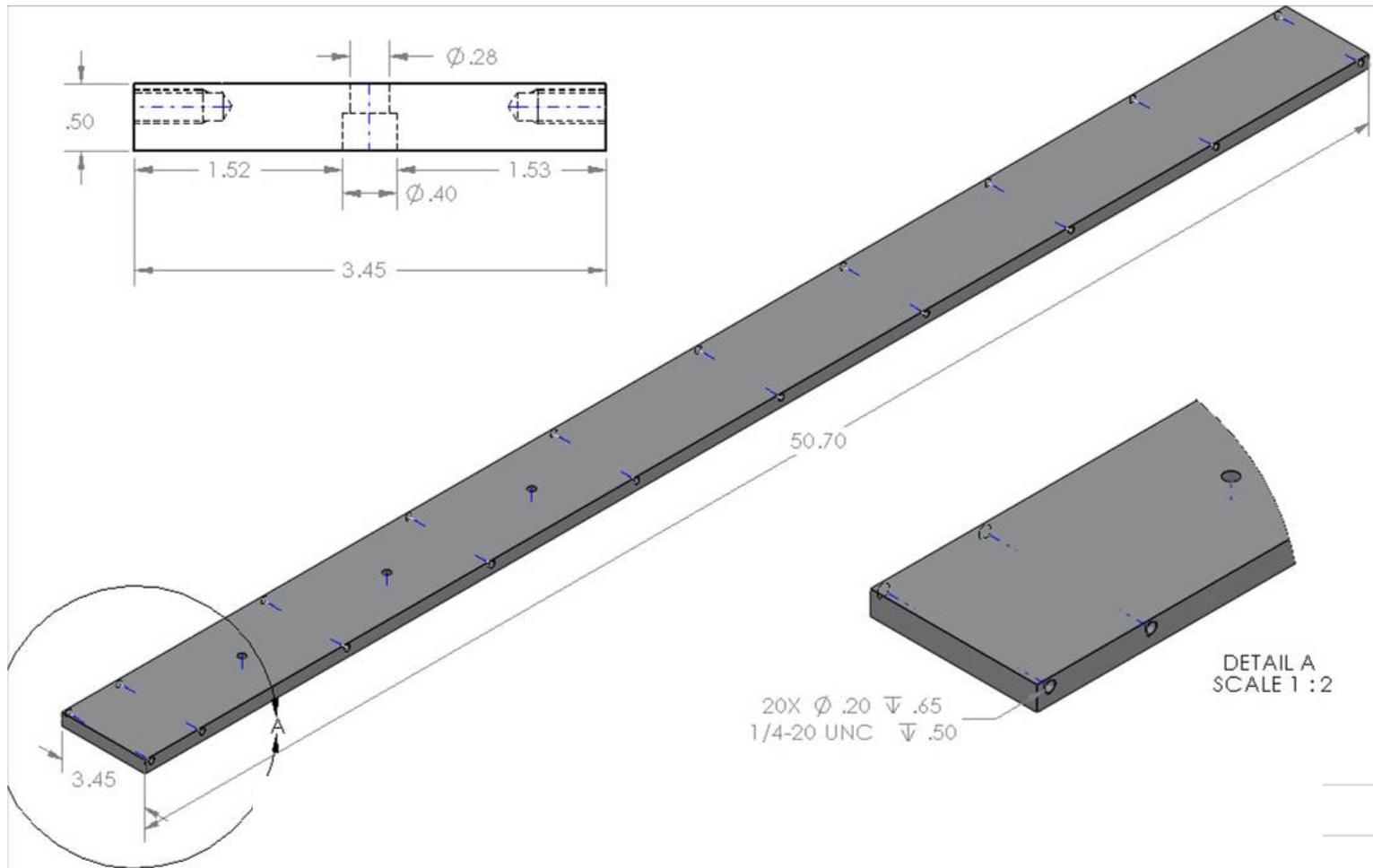
Figure 90.   Insert bottom (1 of 2)

DETAIL C
SCALE 1 : 2

DETAIL B
SCALE 1 : 2
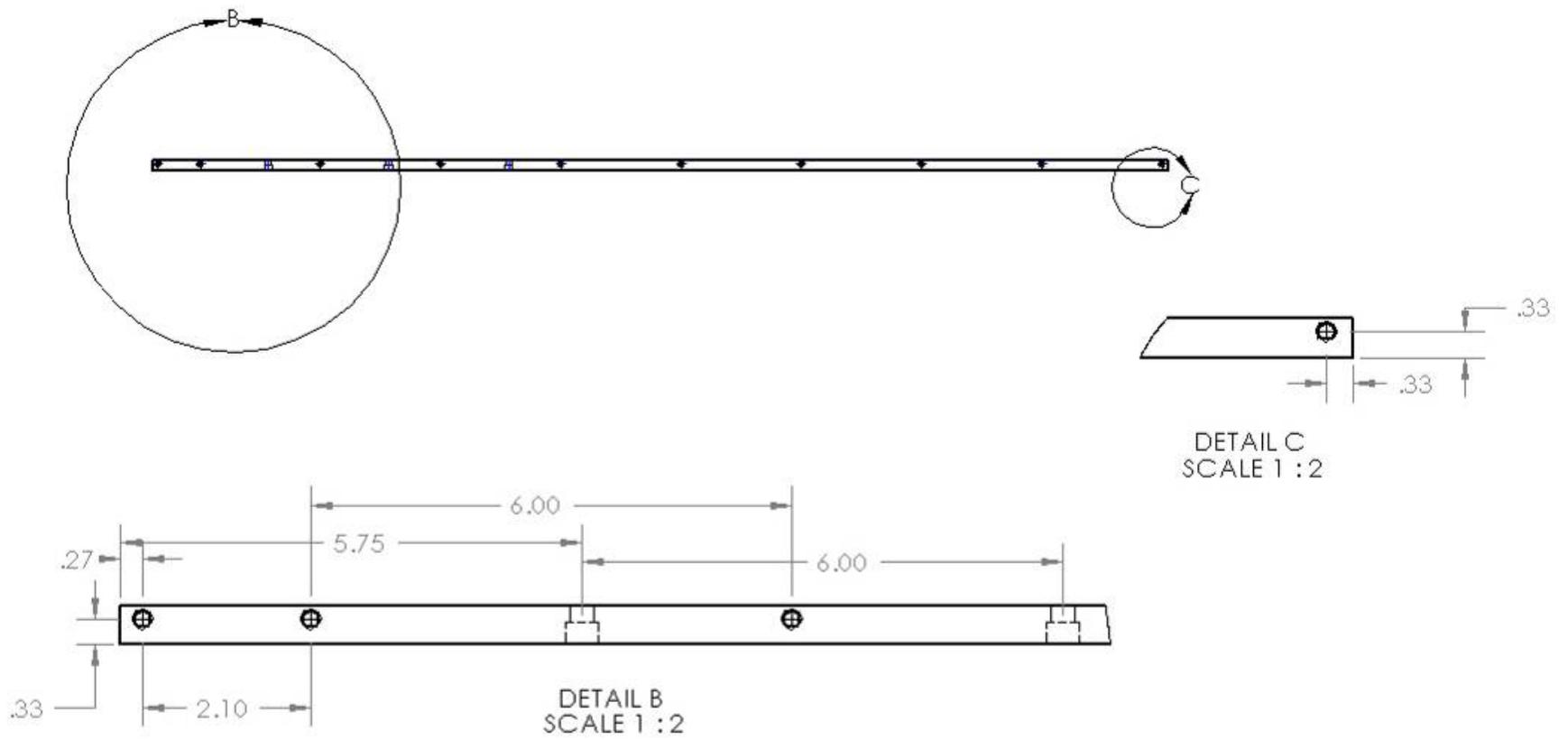
Figure 91.   Insert bottom (2 of 2)
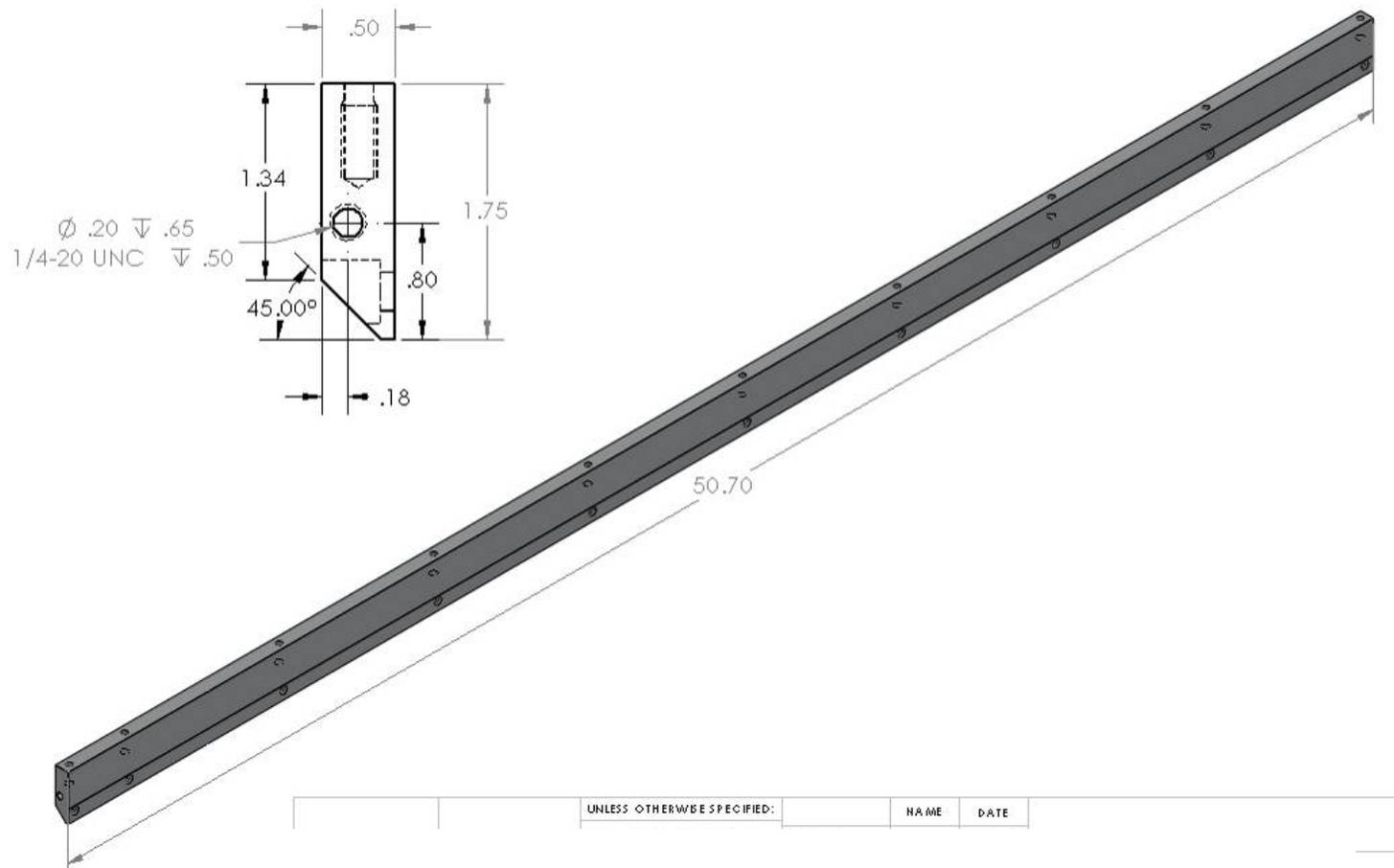
Figure 92.   Insert left (1 of 2) (mirrored for right side)

.33

.33

DETAIL C
SCALE 1 : 2

6.00

10X Ø .27 THRU ALL
⌴ Ø .44 ▽ .40

10x Ø 0.21 ▽ 0.65
1/4-20 UNF ▽0.50

.27

6.00

DETAIL B
SCALE 1 : 4

2.15

.33

2.10

DETAIL A
SCALE 1 : 1

.25
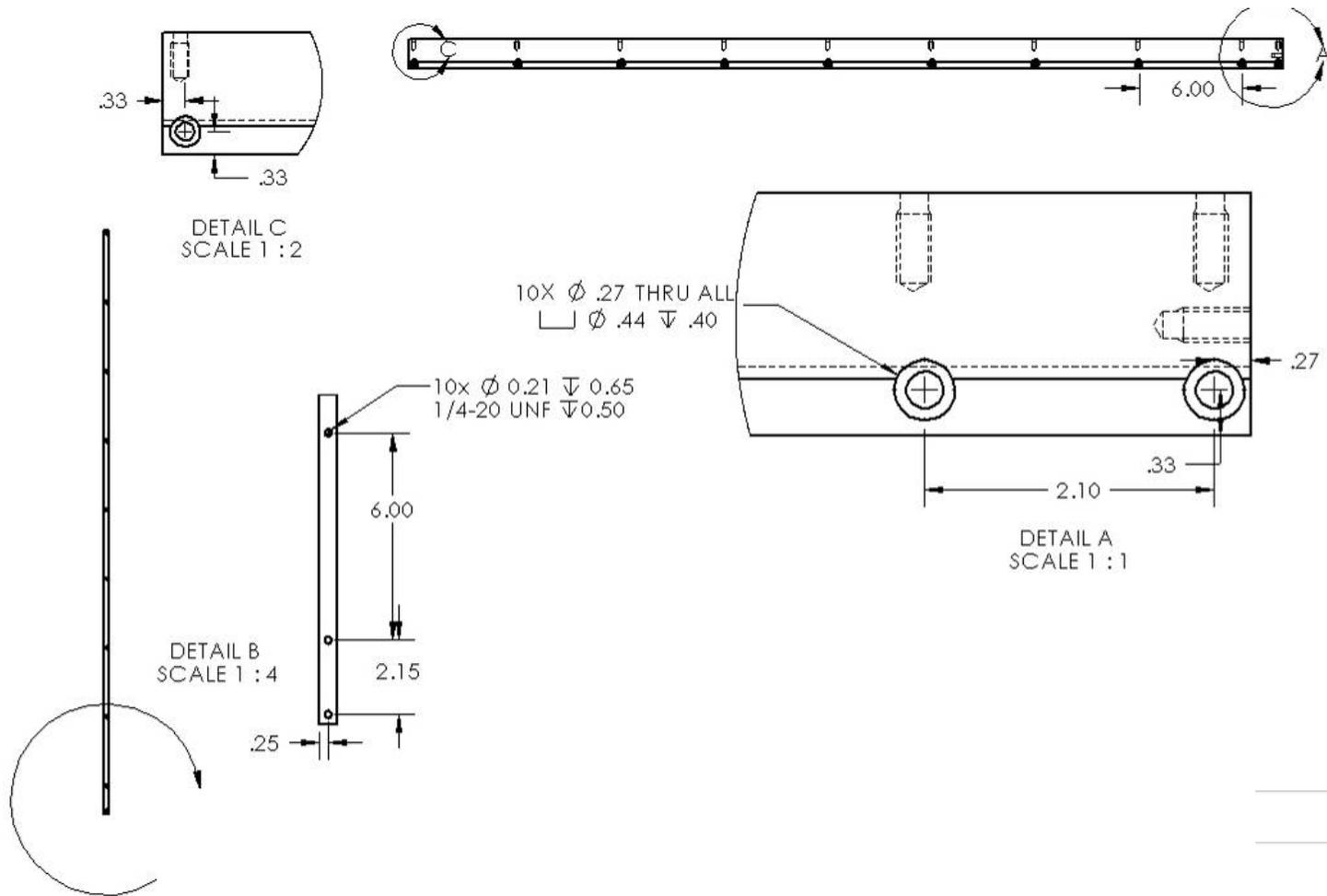
Figure 93.   Insert left (2 of 2) (mirrored for right side)

114
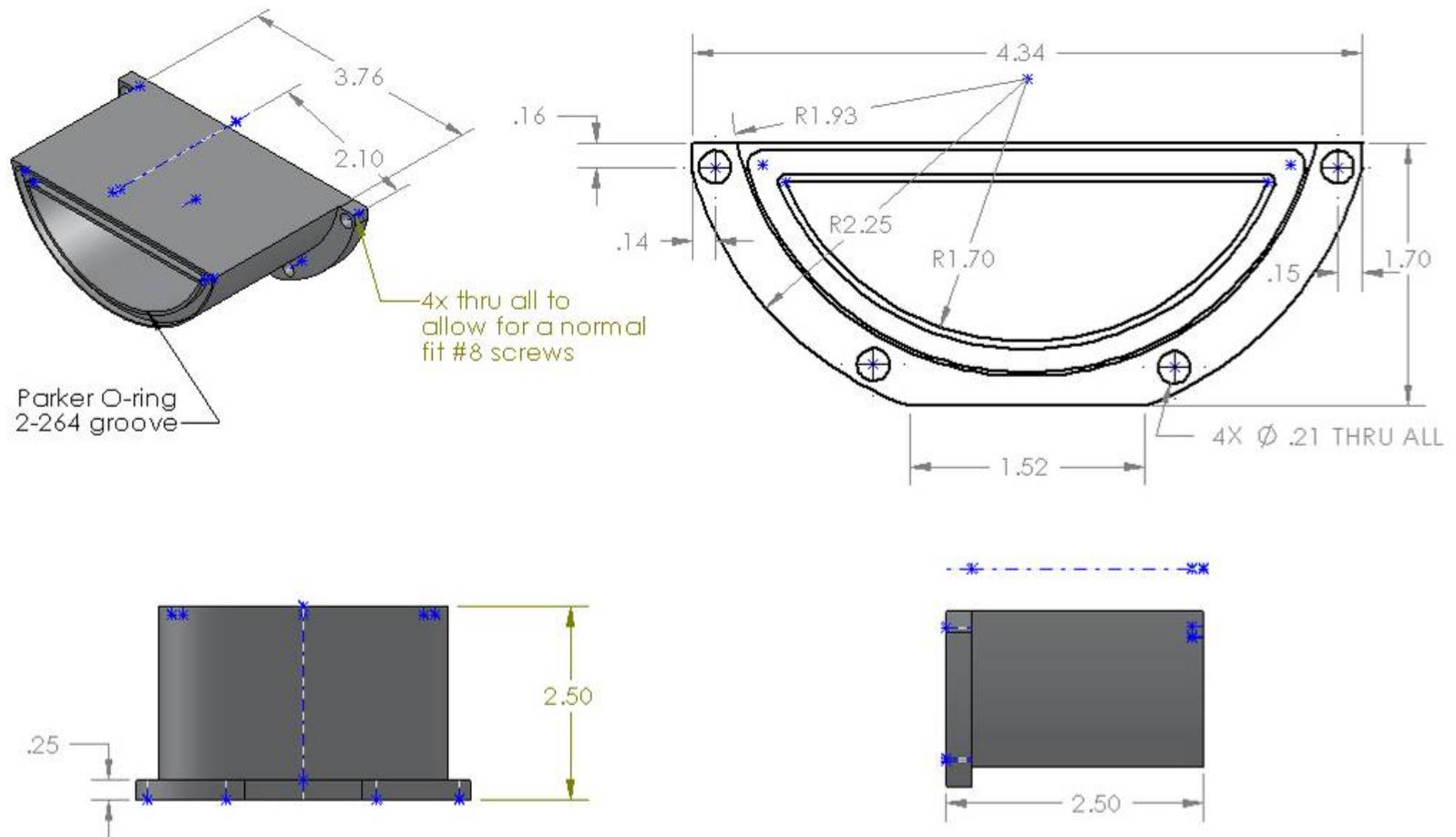
Figure 94.   Insert front

115
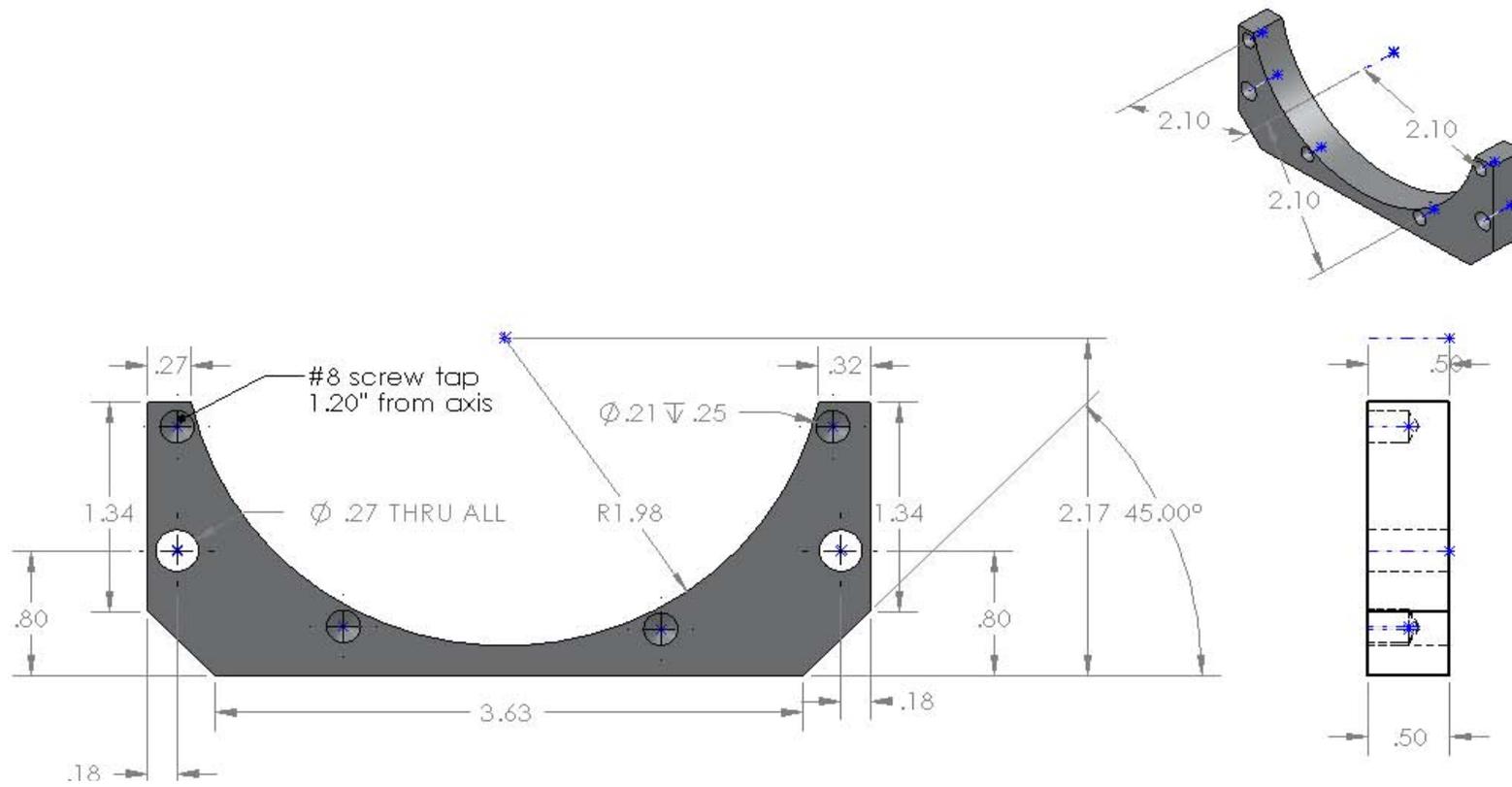
Figure 95. Insert front adapter

116
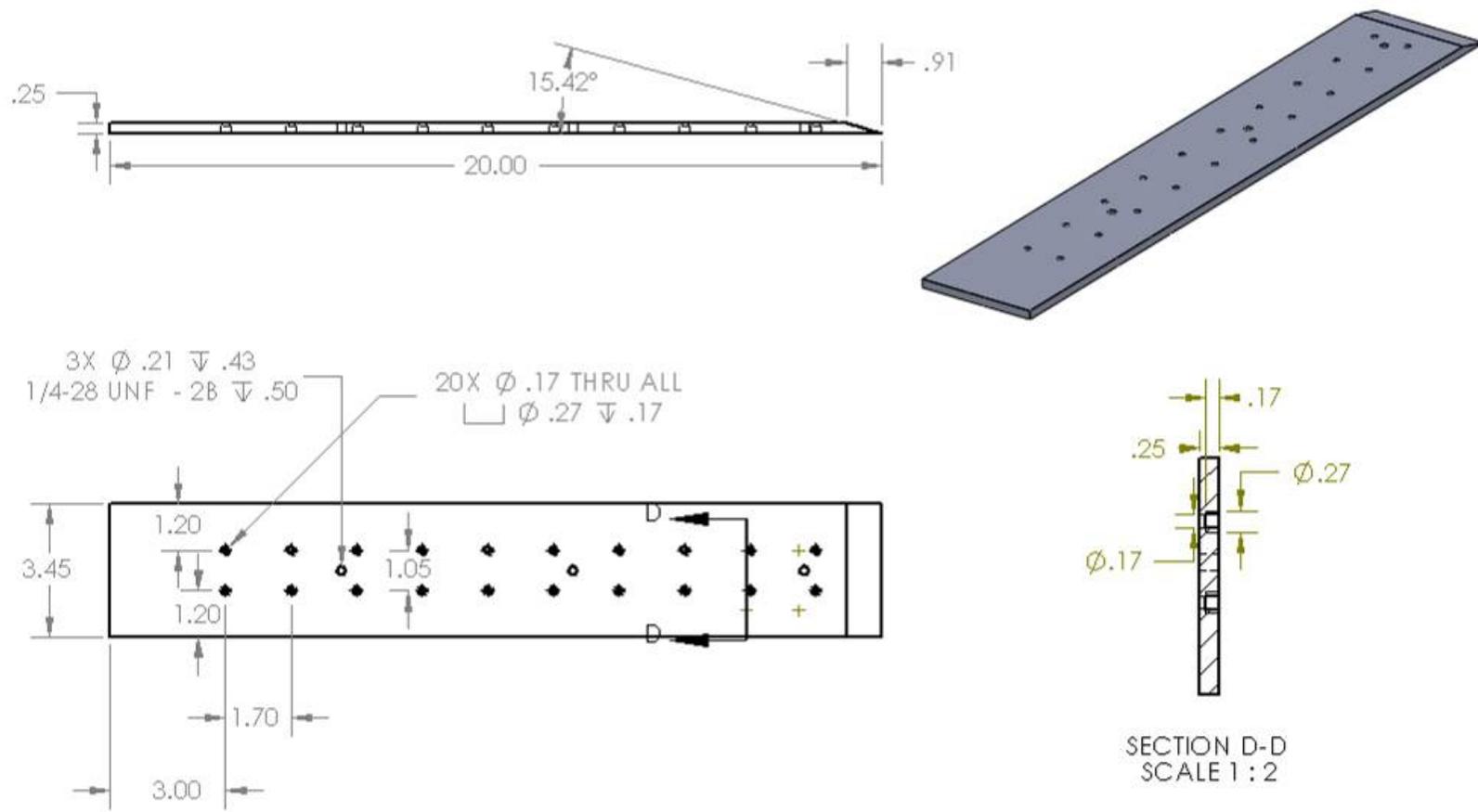
Figure 96. Insert ramp holder (1 of 2)

3X ∅ .21 ▽ .43
1/4-28 UNF - 2B ▽ .50

6.00

6.00

1.73

.73

6.00
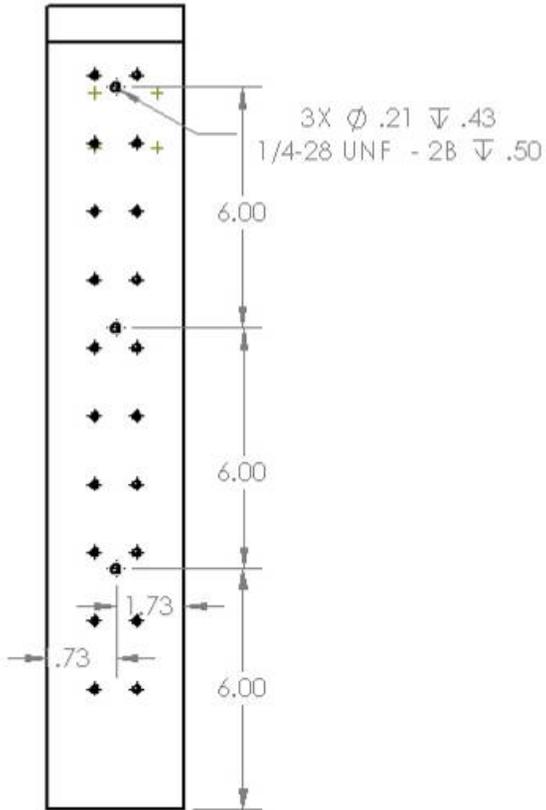
Figure 97.   Insert ramp holder (1 of 2)

118
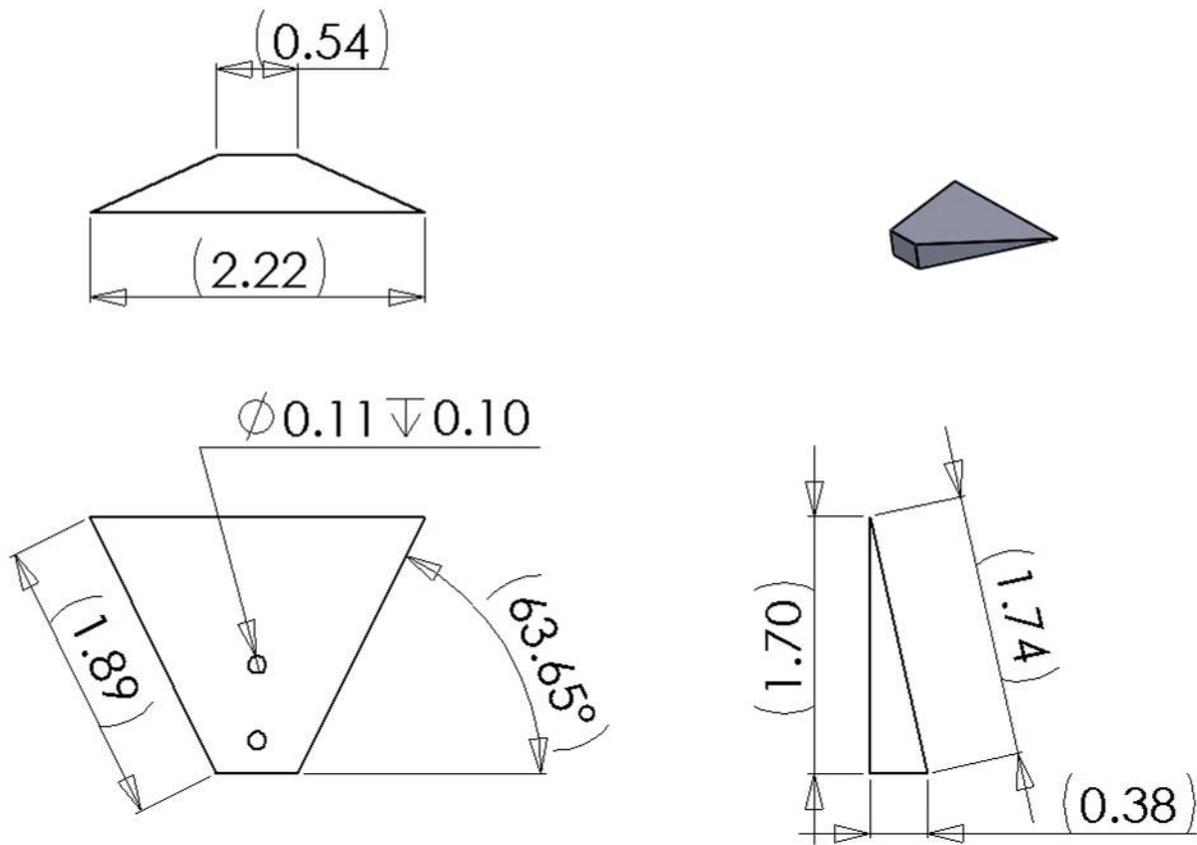
Figure 98.   Small ramps
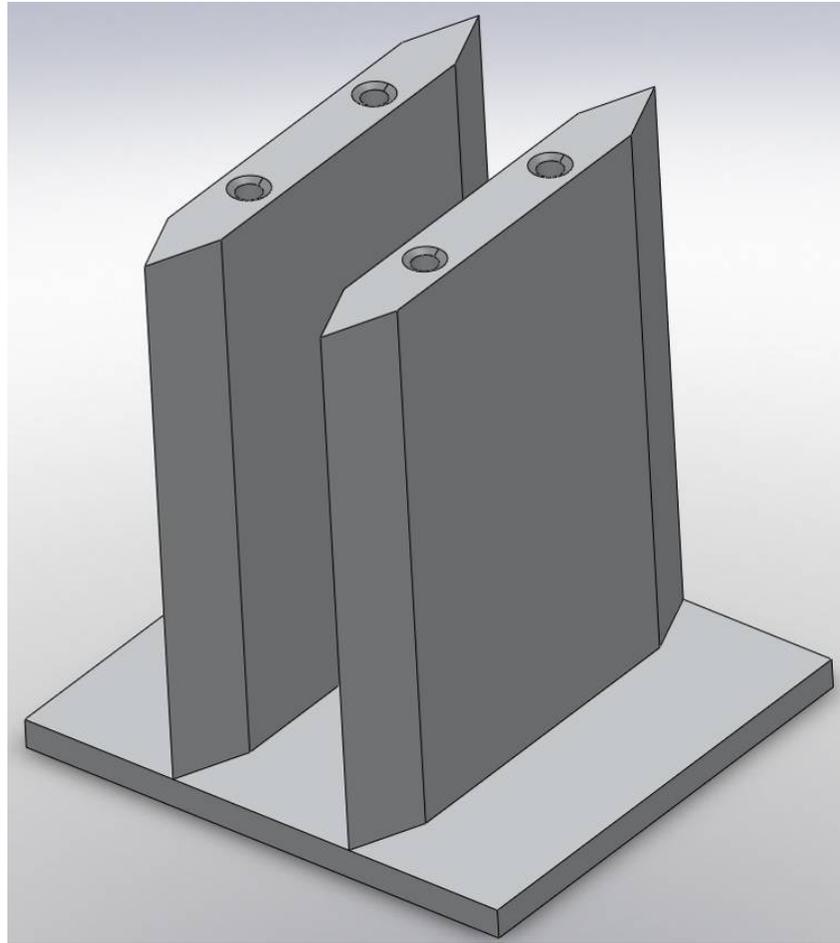
Figure 99.   Step insert sample (steps made for 1:1.25, 1:1.5 and 1:1.75)

6 x Ø 0.280 ▽ 0.253
⌴ Ø 0.400 ▽ 0.125

1.410

4.470

1.650

1.410

1.500

1.250

1.250

4.750

0.101

0.164

0.250

4.650

0.164
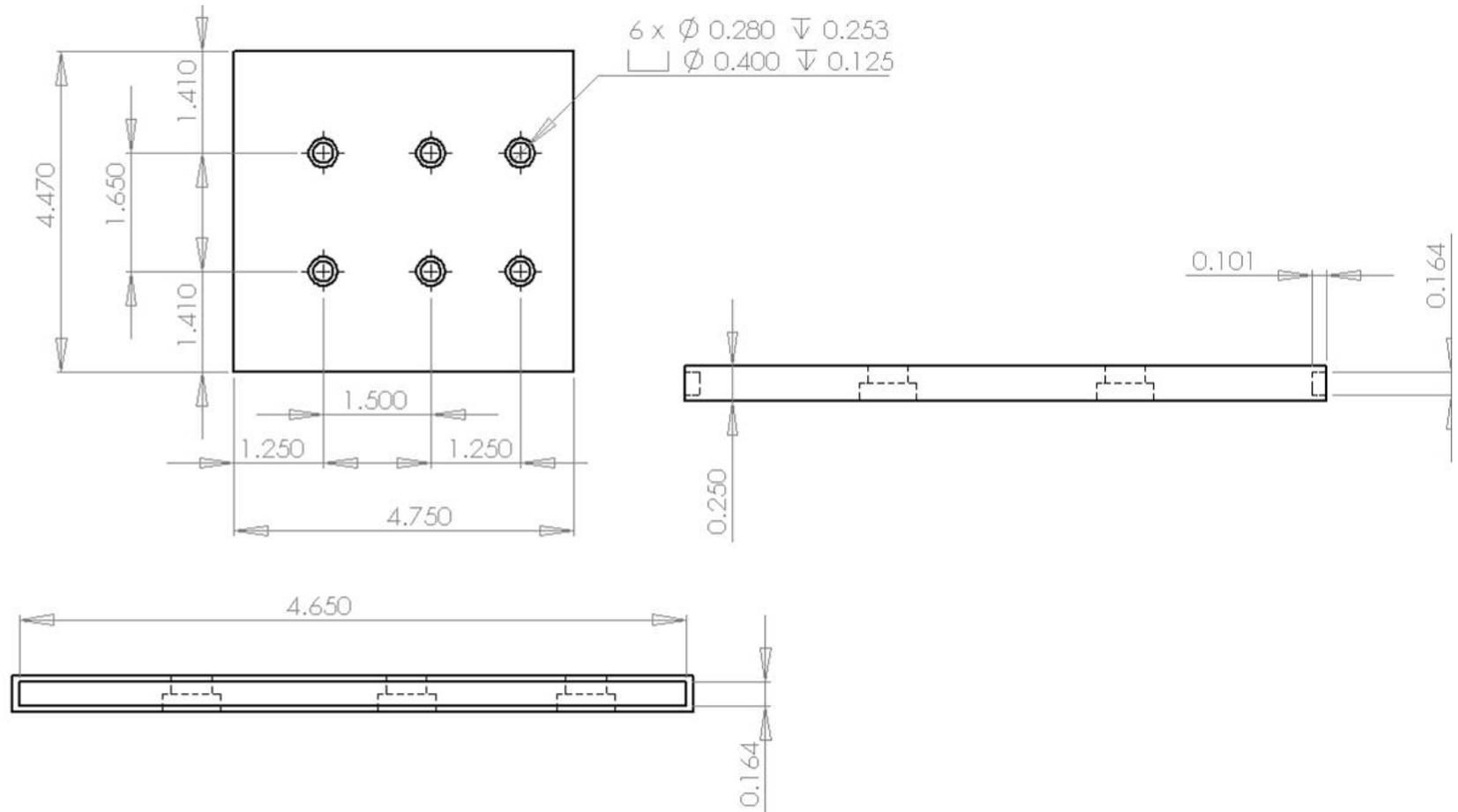
Figure 100.   Step insert lower
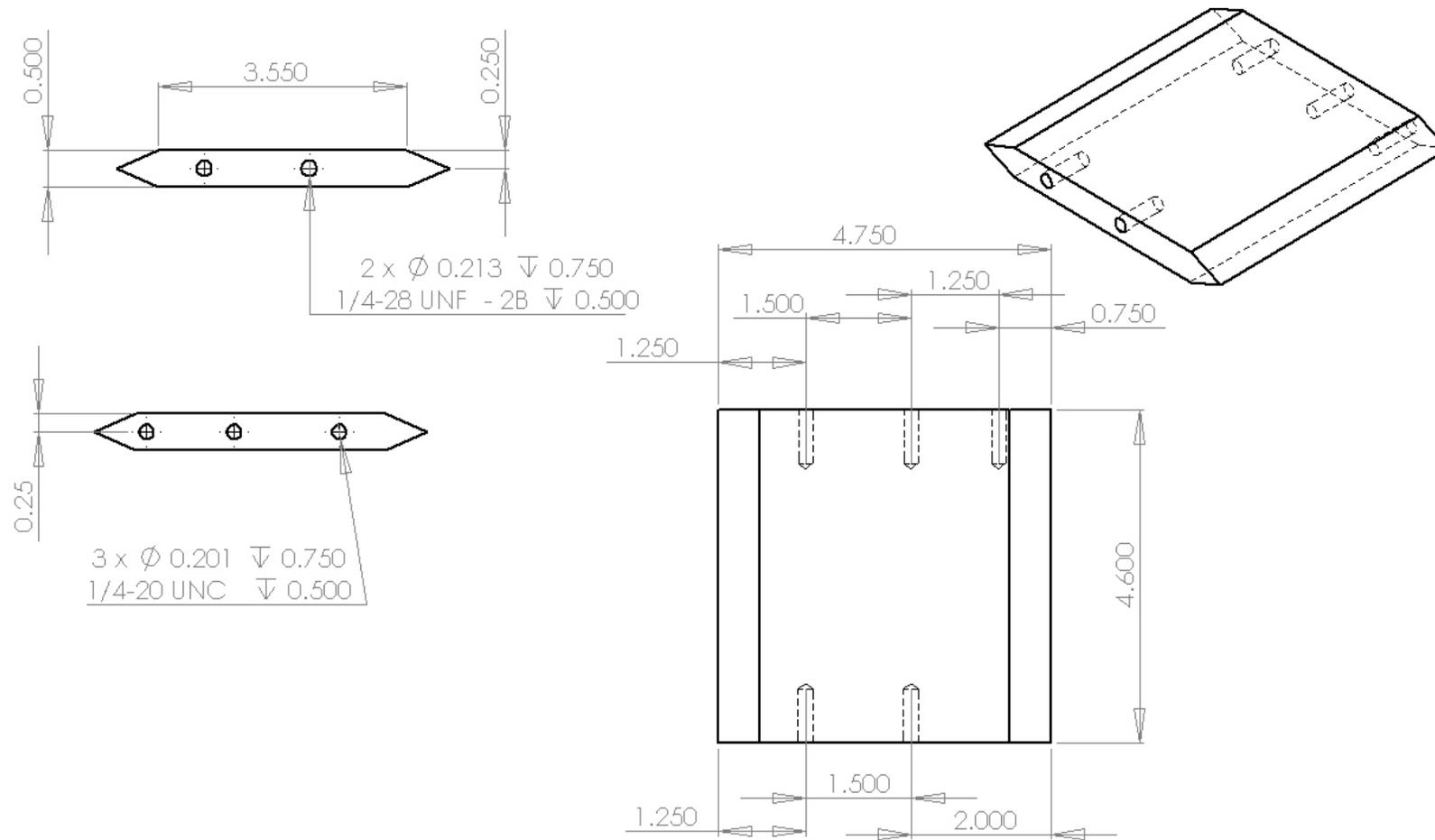
Figure 101.   Step insert support
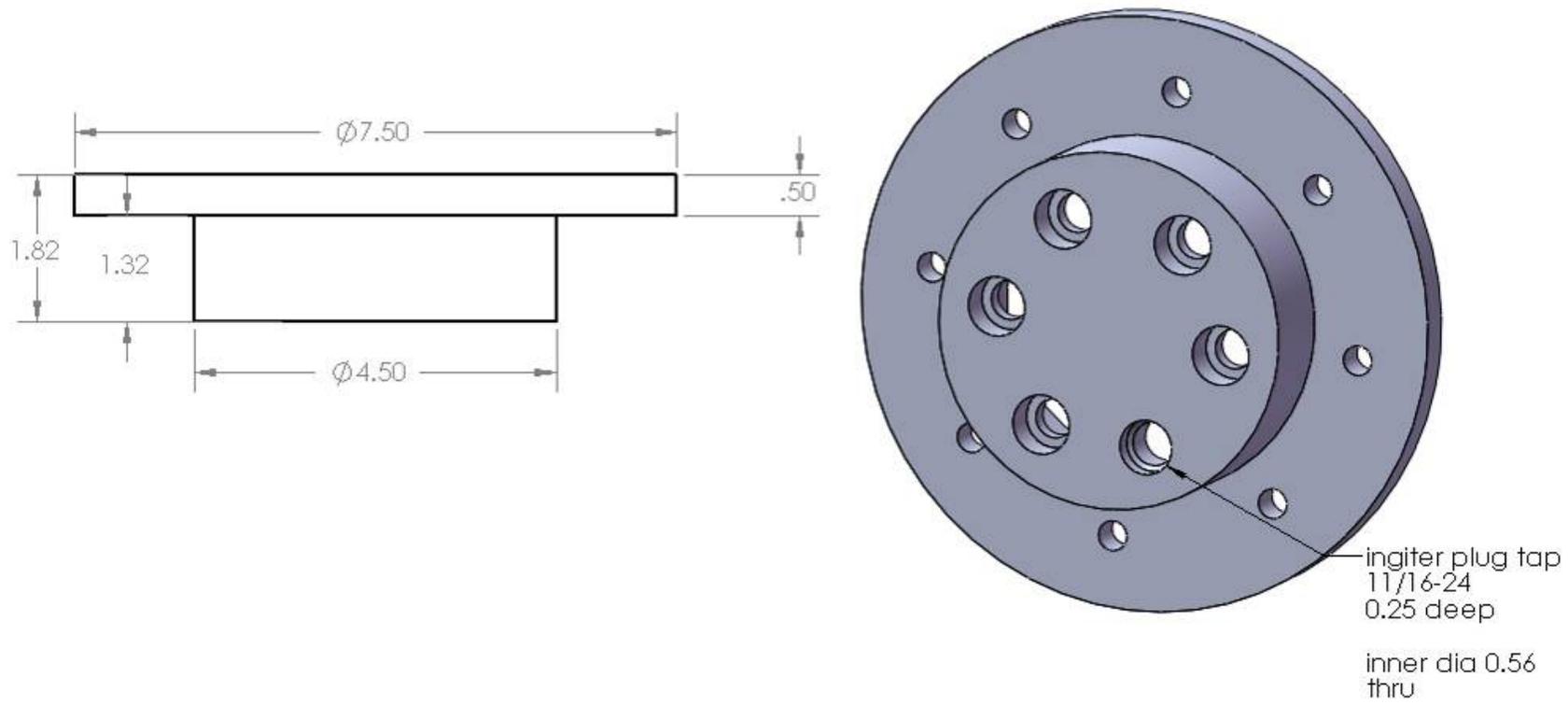
Figure 102.   Inlet manifold (1 of 2)
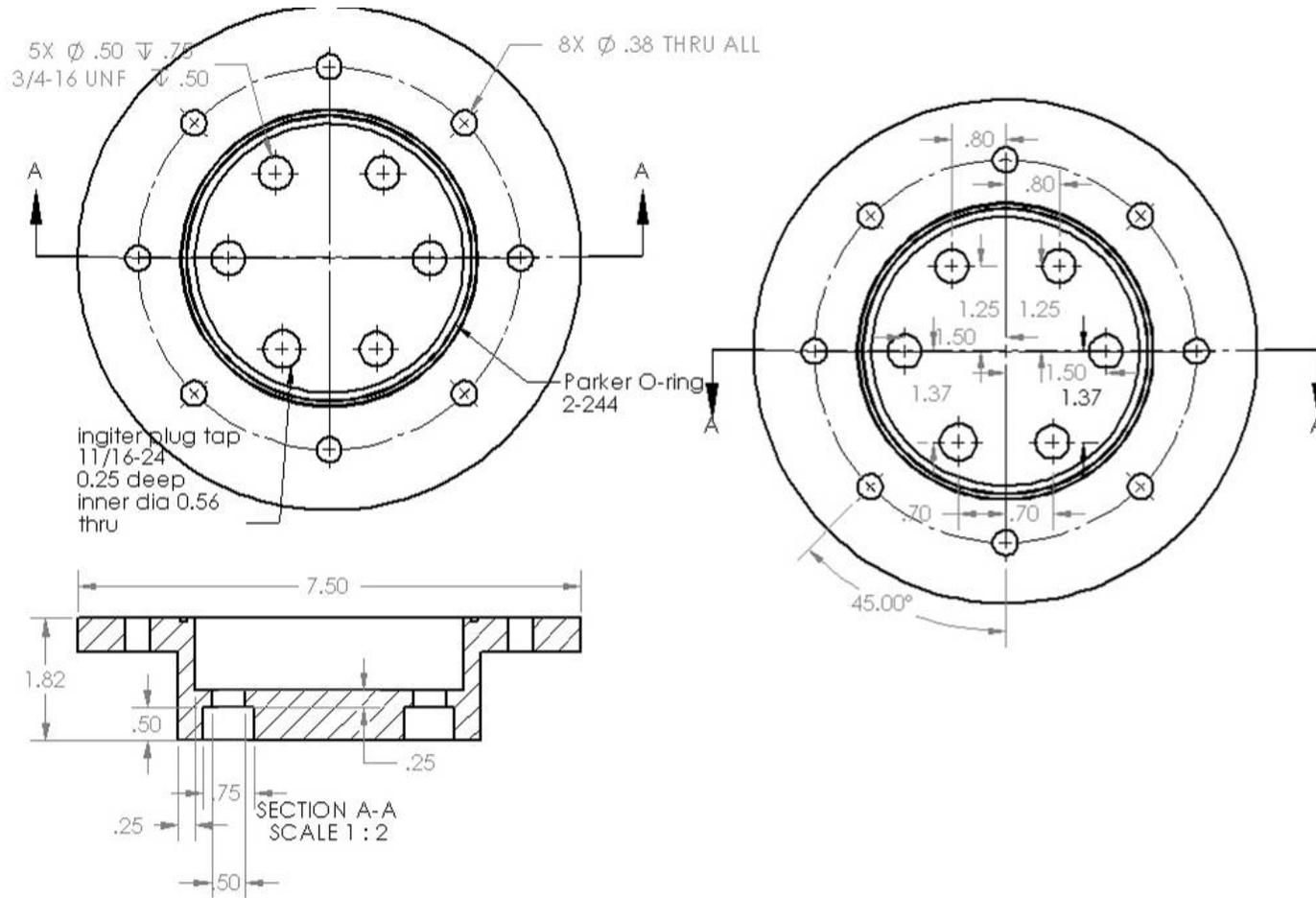
Figure 103. Inlet manifold (2 of 2)

APPENDIX C.   STANDARD OPERATING PROCEDURE

Test Cell #1Standard Operating Procedures (SOP)
Combustor Start Up
(Modification Date 4 Nov 10)

INITIAL SAFETY CHECKS

1. Notify all lab personnel of intention to make test cell 1 live.
2. Turn **ON** control console
3. Turn **ON** warning lights
4. Cell #1 EMERGENCY SHUTDOWN BUTTON (Control Room)– **VERIFY IN**

INITIAL PREPARATIONS

1. Notify the Golf Course (x2167) (Only required if Hot Fire Test is conducted)
2. Open Test Cell Door
3. Igniter Control (Test Cell)–**VERIFY OFF** (Red Button Out)
4. PXI–1000B Rack (Test Cell)–**VERIFY ON**
5. Shop Air–**VERIFY > 100 PSI**
6. Shop Air Valve (Test Cell)–**VERIFY OPEN**
7. 115 VAC Control/Cell #1 Switch (Control Room)–**ON**
8. 28VDC Power Supply/Cell #1 Switch (Control Room)–**ON**
9. Open LABVIEW file "TC1ControllerMike"

TESTING SET–UP

1. Inspect optical section and mirrors for cleanliness
2. Commence Argon–Ion laser start–up procedure (see Arg–Ion SOP)
3. Commence PIV NG–Yag double pulse laser start up (PIV SOP)
4. PIV software controller – **ON**
5. Kistler Amplifier Power–**ENSURE OFF**
6. Kistler Leads–**CONNECT**
7. Exhaust Tube–**VERIFY PROPER POSITION**
8. Notify all personnel that gasses and TESCOM will be enabled.
9. Test Cell #2 and #3 Node 1 Air Isolation Valve (Test Cell #2)–**VERIFY CLOSED**

NOTE: This valve maybe left open only if Test Cell #2 or #3 is configured for active testing

10. TRANSDUCER and TESCOM Power Switch (Test Cell #2)–**ON**
11. Set **0 (Zero)** pressures on ER3000 (Control Room) for the following:
    a. **Node 3 (Hydrogen)**
    b. **Node 1 (Main Air)**
    c. **Node4 (Seeder Air)**
12. Main HP Air Jamesbury Valve (Outside Test Cell)–**OPEN SLOWLY**
13. Power Strip (above PXI–1000B)–**VERIFY ON**
14. Igniter Control Light 5V logic (Red LED CRYDOM 2nd Column, 2nd down in PX–1000B Rack)–**VERIFY OUT**

DANGER: IF RED LIGHT IS ENERGIZED, MUST CLEAR USING LABVIEW BEFORE CONTINUING TO PREVENT PREMATURE IGNITION

15. Igniter Control (Test Cell)–**PUSH RED BUTTON IN**
16. Igniter Control Startup Diagnostics–**OBSERVE COMPLETION OF DIAGNOSTICS** (Verify energy level setting reads 2.03 J)
17. Main HP Air Isolation Valves (2) (Located in Test Cell)–**OPEN SLOWLY**

DANGER: OPEN VALVES SLOWLY TO PREVENT RAPID PRESSURIZATION OF DOWNSTREAM LINES

18. Node 3 (Hydrogen) Shop Air Valve (Above Bottle in Bottle Room)–**OPEN**
19. Hydrogen Bottle Isolation Valve (On Bottle)–**OPEN SLOWLY**

** VERIFY ADEQUATE ETHYLENE PRESSURE FOR TESTING ON DOWNSTREAM GAGE LOCATED IN BOTTLE ROOM**

PRE–TESTING

1. SA–5 Camera–**TURN ON AND REMOVE COVER**
2. Start SA–5 Software
3. Verify Image on SA–5 Software
4. PIV Camera – **TURN ON AND REMOVE COVER**
5. Start PIV software
6. Verify Desired Trigger Types and Valve Durations
7. Determine Desired Fuel and Air Pressures (Mass Flow Choke Calibrations.xls)
8. Set Required Pressures on ER3000
    a. **Node 3 (Hydrogen)**
    b. **Node 1 (Main Air)**
    c. **Node 4 (Seeder Air)**
9. Ready Digital Camera
10. Switch Monitor to Test Cell #1

TESTING

1. Clear All Test Cells and Verify with Head Count
2. Flashing Red Light and Siren–**ENERGIZE**
3. Verify Golf Course is **CLEAR**
4. Digital Camera **RECORD**
5. Camera–**ARM**
6. In LABVIEW Enable Facility Button–**ON**
7. Test Cell #1 Emergency Shutdown Button–**TURN CLOCKWISE**
8. In LABVIEW Start Button–**CLICK TO START**

WHEN TESTING COMPLETE

9. Set Node 1 Pressure to **0 (Zero)**
10. In LABVIEW Turn Off Button–**CLICK TO SECURE**
11. In LABVIEW Enable Facility Button–**VERIFY OFF**
12. Test Cell #1 Emergency Shutdown Button–**PUSH IN**
13. Siren–**OFF**
14. Digital Camera–**Stop/Pause**
15. Save SA–5 Image
16. Save PIV data

NOTE: If Further Testing is Required, re–perform steps 1–15 of the Testing Section

POST–TESTING

1. Close fuel isolation valves, rerun labview code to cycle fuel valve
2. Igniter Control (Test Cell)–**PUSH RED BUTTON OUT**
3. Flow additional Main Air to purge any remaining fuel
4. Set ER300 Node 3 (Ethylene) to **0 (Zero)**
5. Verify pressures on ER3000 are set to 0 (Zero) on the following:
   a. **Node 3 (Hydrogen)**
   b. **Node 1 (Main Air)**
   c. **Node 4 (Seeder Air)**
6. Main HP Air Isolation Valves (2) (Located in Test Cell)–**CLOSE**
7. Main HP Air Jamesbury Valve (Outside Test Cell)–**CLOSE**

NOTE: If Further Testing will be accomplished with a different Ramp obstacle configuration, return to the TESTING SET–UP Section. If not continue to step 7.

8. SA–5 Camera–**TURN OFF AND INSTALL COVER**
9. PIV Camera – **TURN OFF AND INSTALL COVER**

10. TRANSDUCER and TESCOM Power Switch (Test Cell #2)–**OFF**
11. Close Test Cell Door
12. Node 3 (Hydrogen) Shop Air Valve (Above Bottle in Bottle Room)–**CLOSE**
13. Secure Bottle Room
14. Exit out of SA–5 and PIV software
15. EXIT out of LABVIEW
10. 28VDC Power Supply/Cell #1 Switch (Control Room)–**OFF**
11. 115 VAC Control/Cell #1 Switch (Control Room)–**OFF**

LIST OF REFERENCES

[1]   K. K. Kuo, *Principles of Combustion*. John Wiley & Sons 2nd edition, Inc., 1986.

[2]   R. Friedman, *American Rocket Society*, vol. 24, pp. 349, 1953.

[3]   C .M. Brophy, J. O. Sinibaldy, D. Netzer, and K. Kailasanath, "Initiator Diffraction limits in a Pulse Detonation Engine," *in Confined Detonations and Pulse Detonation Engines*., Torus Press, 2003.

[4]   M. Fludovich, "Investigation of detonation wave diffraction interaction with reactive transpiration," M.S. thesis, Naval Postgraduate School, Monterey, CA, 2002.

[5]   E. Tousse, "Transmission of a detonation wave across a sudden expansion with varying mixture composition," M.S. thesis, Naval Postgraduate School, Monterey CA, 2003.

[6]   C. M. Brophy, AIAA–2009–1611, "Initiation Improvements for Hydrocarbon/Air Mixtures in Pulse Detonation Applications," *47th AIAA Aerospace Sciences Meeting including The New Horizons Forum and Aerospace Exposition*, Orlando, Florida, Jan. 5–8, 2009.

[7]   J. H. S. Lee, *The Detonation Phenomenon*, Cambridge Univ. Press, Cambridge, 2008.

[8]   E. Schultz, Detonation Diffraction, Ph.D. dissertation, California Institute of Technology, 2000.

[9]   NASA CEA, *NASA* computer program for calculating of the Chemical Equilibrium with Applications, NASA Glenn Research Center, Cleveland, OH.

[10]   J. Shepherd, Detonation Database, May 2002. http://www.galcit.caltech.edu/detn_db/html/C2H2–Air2.html.

[11]   P. Lafitte, *Ann Phys. Ser*. vol. 4, p. 587, 1925.

[12]   Y. B. Zeldovich, Kogarko S.M. and Simonov. *Sov. Phys. Tech. Phys.*, vol. 1: pp.1689–1713, 1957.

[13] K. I. Shchelkin and Y. K. Troshin Ya.K., *Gasdynamics of Combustion*, Mono Book Corp, 1965.

[14] V. V. Mitrofanov, R.I Solouhkin, *Sov. Phys. Dokl.*, vol. 9(12), pp.1055, 1965.

[15] A. N. Dremin, V.S. Trofimov, *Proc. Combust. Inst.*, vol. 10, pp.839–843, 1965.

[16] W. B. Benedick, R. Knystautas R, and J. H. Lee, "Large scale experiments on the transmission of fuel-air detonations from two-dimensional channels," *Progress in Astronautics and Aeronautics*, vol. 94, pp. 546–555, 1984.

[17] J. S. Lee, in: J. Bowen (Ed.), *Dynamics of Exothermicity*, Gordon and Breach, Amsterdam, Netherlands, 1996.

[18] F. Pintgen and J. E. Sheperd, "Detonation Diffraction in Gases," *Combustion and flame*, vol. 156, pp. 665–677, 2009.

[19] M. C. Burrows and A. P Kurkov, "Analytical & Experimental Study of Supersonic Combustion of Hydrogen in a Vitiated Air Stream," *NASA TM X–2828*, 1973.

[20] E. L. Petersen and R. K. Hanson, "Reduced kinetics Mechanism for Ram accelerator combustion*," Journal of Propulsion and Power*, vol.15, pp.591–600.591–600, 1999.

[21] J. M. Powers and S. Paolucci, "Accurate spatial resolution estimates for reactive supersonic flow with detailed chemistry". *AIAA Journal*, vol. 43, pp.1088–1099, 2005.

[22] I. Ho, "Investigation on novel methods to increase specific thrust in pulse detonation engines via imploding detonations," M.S. thesis, Naval Postgraduate School, Monterey CA, 2009.

[23] C. Myers, "Initiation Mechanisms of Low-Loss Swept-Ramp Obstacles for Deflagration to Detonation Transition In Pulse Detonation Combustors," M.S. Thesis, Naval Postgraduate School, Monterey, CA, 2009.

[24] I. O. Moen, G. O. Sulmistras et al., in *Dynamics of Explosions,* ed J.R. Bower, J. C. Reyer, R. I Soloukhin, 1985.

[25]   B. W. Skews, "The perturbed region behind a diffracting shock wave." *Journal of Fluid Mechanics*, vol. 29: pp. 705–719, 1967.

INITIAL DISTRIBUTION LIST

1.   Defense Technical Information Center
      Ft. Belvoir, Virginia

2.   Dudley Knox Library
      Naval Postgraduate School
      Monterey, California

3.   Graduate School of Engineering and Applied Sciences
      Naval Postgraduate School
      Monterey, California

4.   Professor Jose O. Sinibaldi
      Department of Physics
      Naval Postgraduate School
      Monterey, California

5.   Professor Christopher M. Brophy
      Department of Mechanical and Aeronautical Engineering
      Naval Postgraduate School
      Monterey, California

6.   Professor Knox T. Millsaps
      Department of Mechanical and Aeronautical Engineering
      Naval Postgraduate School
      Monterey, California

7.   Major Daniel M. Juillet
      Department of Mechanical and Aeronautical Engineering
      Naval Postgraduate School
      Monterey, California